Università degli Studi di Torino
Scuola di Dottorato

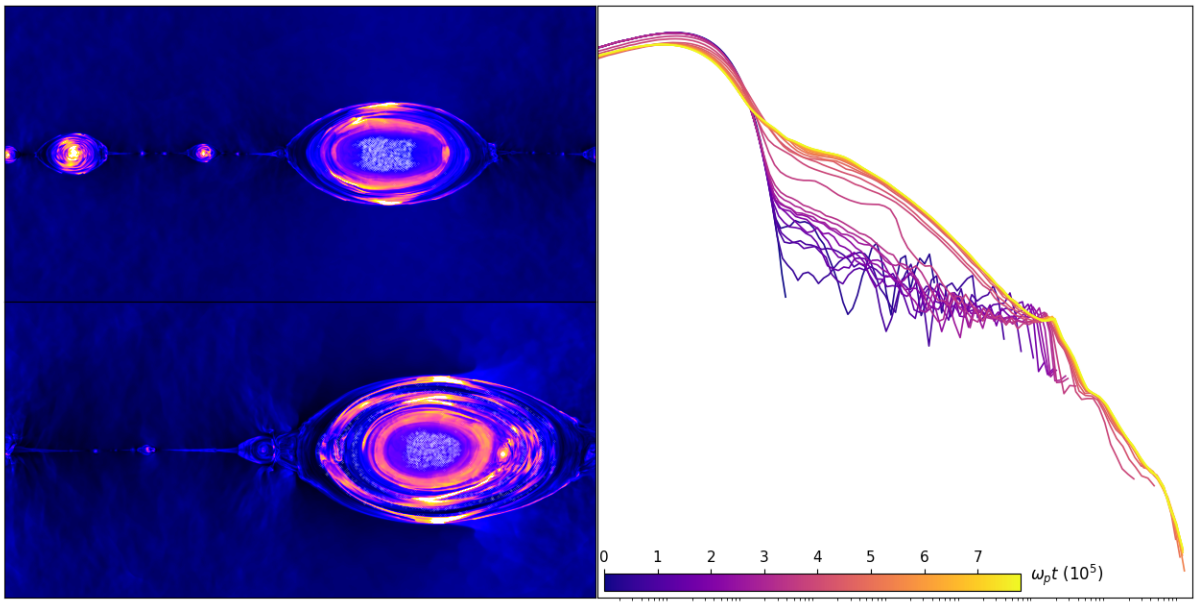

On the impact of numerical and physical resistivity on magnetic reconnection and particle acceleration

Eleonora Puzzoni

Università degli Studi di Torino
Scuola di Dottorato

Dottorato in Fisica

On the impact of numerical and physical resistivity on magnetic reconnection and particle acceleration

Eleonora Puzzoni

Tutor: Andrea Mignone

To Carla. Thank you for pushing me into the physics career.

Abstract

Particle acceleration in astrophysical plasmas is a process of crucial importance for the interpretation of the most energetic phenomena in the universe produced, for example, in Active Galactic Nuclei, Pulsar Wind Nebulae, and Gamma-Ray Bursts. The recent wealth of investigation by means of numerical simulations has shown that, when compared to shock diffusive acceleration, relativistic magnetic reconnection taking place in strongly magnetized current sheets can result in a more efficient and universal acceleration process. In particular, dynamic instabilities such as the tearing one can trigger a magnetic reconnection regime with time-scales comparable to the ones observed in astrophysical plasmas.

However, discretization techniques used in numerical simulations introduce artificial viscosity effects which are not easily quantifiable but can be reduced through high-order methods and/or at finer mesh spacing. Therefore, we investigated the impact of different numerical algorithms, grid resolutions, and physical resistivity on magnetic reconnection as well as on particle acceleration mechanisms. 2D magnetohydrodynamics numerical simulations of tearing-unstable current sheets coupled to a population of non-thermal test-particles are performed with the PLUTO code for astrophysical fluid dynamics. Our results indicate that the reconnection rate of the background tearing-unstable plasma converges only for finite values of the Lundquist number and for sufficiently large grid resolutions. On the other hand, the process of particle acceleration is found to be nearly independent of the underlying numerical details since the system becomes tearing-unstable and enters its non-linear stages. In the limit of large Lundquist numbers, the ensuing power-law index quickly converges to $p \approx 1.7$, consistently with the fast reconnection regime.

In the context of particle acceleration in high-energy astrophysical envi-

ronments featuring magnetic reconnection, the importance of the resistive term of the electric field compared to the convective one is still under debate. Therefore, in the second half of this thesis, the importance of the resistive contribution in accelerating particles is investigated. We find that the resistive field plays a significant role in the early-stage energization of high-energy particles. Indeed, these particles are firstly accelerated due to the resistive electric field when they cross an X-point, created during the fragmentation of the current sheet due to the onset of the tearing instability. If this preliminary particle acceleration mechanism dominated by the resistive field is neglected, particles cannot reach the same high energies. Our results support, therefore, the conclusion that the resistive field is not only non-negligible but it does actually play an important role in the particle acceleration mechanism.

List of Acronyms

Below is the list of acronyms that have been used throughout this thesis listed in alphabetical order:

AGNs	Active Galactic Nuclei
AU	Astronomical Unit
AW	Alfvén waves
CMB	Cosmic Microwave Background
CFL	Courant-Friedrichs-Lewy
CRs	Cosmic Rays
CT	Constrained Transport
DSA	Diffusive Shock Acceleration
FSRQ	Flat Spectrum Radio Quasars
FTBS	Forward in Time, Backward in Space
FW	Fast Waves
GRBs	Gamma-Ray Bursts
GZK	Greisen-Zatsepin-Kuzmin
EHT	Event Horizon Telescope
ICM	Intracluster Medium
IGM	Intergalactic Medium
IR	Infrared
KH	Kelvin-Helmholtz
LTE	Local Thermal Equilibrium
MHD	Magnetohydrodynamics
PIC	Particle-In-Cell
QSO	Quasi Stellar Objects
RMHD	Relativistic Magnetohydrodynamics
RK2	2^{nd}-order Runge-Kutta
RK3	3^{rd}-order Runge-Kutta
SED	Spectral Energy Distribution
SMBH	Supermassive Black Holes
SNR	Supernova Remnant
SW	Slow Waves
TD	Tangential Discontinuity
TM	Tearing mode
UCT	Upwind Constrained Transport

Nomenclature

Below is the nomenclature of indices and parameters that have been used throughout this thesis.

Indices

a	Index for atoms
c	Index for the convective contribution
E	Index for the east-direction with respect to zone edge
e	Index for electrons
i	Index for positive ions or for grid points along x-axis
j	Index for grid points along y-axis
k	Index for grid points along z-axis
L	Index for the left side of the interface
N	Index for the north-direction with respect to zone edge
n	Index for step number
p	Index for protons or single particle
R	Index for the right side of the interface
r	Index for the resistive contribution
S	Index for the south-direction with respect to zone edge
W	Index for the west-direction with respect to zone edge
0	Index for the ground state or the equilibrium value

Parameters

$\mathbf{A}$	Vector potential
a	Initial current sheet width
$\mathbf{B}$	Magnetic field

C_a	Courant number
c	Speed of light
$\mathbb{C}$	Speed of light artificial value
$\bar{d}$	Average particle distance
d_l	Optimal weights for a 5^{th}-order accurate approximation
e	Electron charge
$\mathbf{E}$	Electric field
E_{kin}	Particle kinetic energy
E_t	Total energy density
E_{thr}	Threshold kinetic energy
F	Flux tensor
$f(\mathbf{x}, \mathbf{v}, t)$	Distribution function
f_{part}	Fraction of particles
$f_{[\text{S}]}$	Short for flux
I	Ionization energy
$\mathcal{I}(f_{[\text{s}]})$	Interface values reconstruction
$\mathbf{J}$	Current density
k	Boltzmann constant
k_{max}	Maximum wavenumber for the fastest growing mode
$\mathcal{L}$	Flux difference operator
L	System length
L_{bol}	Bolometric luminosity
L_{GRB}	GRBs luminosity
$\mathbf{m}$	Momentum density
m	Particle mass
M_*	Stellar mass
$M_\odot$	Solar mass

n	Number density
N	Total number of particles
N_m	Number of modes
N_{part}	Number of particles in each energy bin
N_x	Grid resolution along the x-axis
$\mathbf{p}$	Particle momentum
p	Power-law index
P	Plasma pressure
P_{IC}	Inverse Compton emission power
P_{sync}	Synchrotron emission power
q	Charge density
$\mathbf{q}$	Thermal flux vector
R_m	Reynolds number
R_{rec}	Reconnection rate
S	Lundquist number
$\mathbf{S}$	Poynting vector
t	Time
t_{stop}	Final computational time
T	Plasma temperture
T_B	Brightness temperature
$\mathcal{U}$	Array of conserved quantities
U_B	Magnetic field energy density
$\mathbf{u}$	Four-velocity coordinates
U_{rad}	Radiation energy density
$\mathcal{V}$	Array of primitive variables
V	Volume
v_A	Alfvén velocity

$\mathbf{v}_g$	Gas velocity
$\mathbf{v}$	Velocity coordinates
v_s	Shock velocity
v_T	Thermal velocity
W or W_{tot}	Energy gained by particles
$\mathbf{x}$	Position coordinates
Z	Atomic number
β	β-parameter
β_l	Smoothness indicators
Γ	Polytropic index
γ	Lorentz factor
γ_{max}	Maximum growth rate for the fastest growing mode
γ_{TM}	Tearing mode growth rate
Δx	Coordinate spacing along x-axis
Δy	Coordinate spacing along y-axis
Δz	Coordinate spacing along z-axis
Δt	Time step
$\Delta\tilde{\mathcal{V}}$	Slopes
δ	Spectral index
ϵ	Perturbation amplitude
η	Physical resistivity
θ	Angle between $\mathbf{v}$ and $\mathbf{B}$
λ	Characteristic speeds
λ_D	Debye length
ν_c	Particle collision rate
$\mathbf{\Pi}$	Viscous stress tensor
ρ	Plasma density

σ	Electrical conductivity
σ_d	Standard deviation
σ_T	Thomson cross section
τ	Thermalization time
τ_A	Alfvénic time
τ_c	Convective time scale
τ_d	Diffusive time scale
ϕ	Dissipative term
ϕ_m	Random phases
χ	Degree of ionization
$\psi(\mathbf{v})$	Arbitrary velocity function
ω_c	Larmor frequency
ω_l	Weights
ω_p	Plasma frequency

Contents

List of Figures

List of Tables

1

Introduction

The study of particle acceleration is of fundamental importance to understanding the high-energy part of the spectra of the most powerful astrophysical sources, such as Gamma-Ray Bursts (GRBs) and Active Galactic Nuclei (AGNs). This chapter gives an overview of the reference astrophysical scenario, as well as the particle acceleration mechanisms taking place in these environments. Moreover, this chapter describes the techniques used to carry out this study, which must necessarily involve numerical simulations.

1.1 High-energy astrophysical scenario

Much of the energy output from the most powerful environments of the universe such as Gamma-Ray Bursts (GRBs; see, e.g., Giannios, 2008; McKinney and Uzdensky, 2012; Sironi and Giannios, 2013; Beniamini and Piran, 2014; Beniamini and Giannios, 2017) and jets found in Active Galactic Nuclei (AGNs; see, e.g., Böttcher, 2007; Giannios, 2013; Sironi et al., 2015; Petropoulou et al., 2016), features a non-thermal signature originated by high-energy particles. This non-thermal signature has been observed from the radio to the gamma-ray wavebands, up to TeV energies.

1.1.1 Gamma-Ray Bursts

Gamma-Ray Bursts (GRBs) are high-energy explosions with luminosities exceeding, in some cases, $L_{\mathrm{GRB}} = 10^{54}\ erg/s$ (Pescalli et al., 2016). These explosions may be connected to the merging of compact objects in binary systems (i.e., short GRBs) or the collapse of a massive star into a black hole or a neutron star (i.e., long GRBs). The binary systems linked to short GRBs may be composed of neutron stars or a neutron star and a black hole (see, e.g., Kumar and Zhang, 2015). As claimed by, e.g., Perna et al. (2016), a short GRB can also be produced by the merger of two black

holes. On the other hand, the massive stars that collapse and generate long GRBs are of Wolf-Rayet type with a mass $M_* \gtrsim 30 M_\odot$ (see Piron, 2016). As the name suggests, short and long GRBs are distinguished, for the first time by Kouveliotou et al. (1993), by their duration, respectively less or more than about 2 seconds. In particular, short GRBs last from a minimum of a few milliseconds and a maximum of about 2 seconds (see, e.g., Lazzati, 2020).

The GRBs emission is characterized by two phases: the prompt and the afterglow phase (see Fig. 1.1). The former is a short phase, whose duration distinguishes short and long GRBs (Lazzati, 2020). The prompt phase features an emission that is very intense in the hard X- and gamma-ray bands. This phase is followed by another one: the afterglow (first observed by the BeppoSAX satellite; see Costa et al., 1997; van Paradijs et al., 1997). This is a longer but less energetic phase, as the emission peaks at less energetic wavelengths (i.e., X-ray, visible and radio; see Piron, 2016).

The fireball model (see Wijers et al., 1997, and reference therein) explains how the prompt emission and the afterglow phase are produced. According to this model, the merger of a neutron star binary system or the collapsed core of a massive star are considered as central engines launching a plasma composed of electrons, positrons, and baryons in the form of highly relativistic jets. The prompt and the afterglow emissions are produced by the interactions of blobs inside the jet itself and with the surrounding material, respectively (see, e.g., Dainotti et al., 2018). However, as pointed out in Dainotti et al. (2018), this model is not effective in explaining all the observations of GRBs (see, e.g., Willingale et al., 2007; Melandri et al., 2008).

Long GRBs can be detectable out to very high redshifts. Therefore, they can be used to study the stars formation rate and their environmental impact, for instance, on the metal enrichment of the intergalactic medium (IGM; see Wang et al., 2015). Moreover, they can be used to investigate the expansion rate of the Universe, as well as the properties of dark energy (see, e.g., Demianski et al., 2017).

1.1.2 Active Galactic Nuclei

Active Galactic Nuclei (AGNs) are compact regions at the center of galaxies powered by accretion onto supermassive black holes (SMBH with $M \gtrsim$

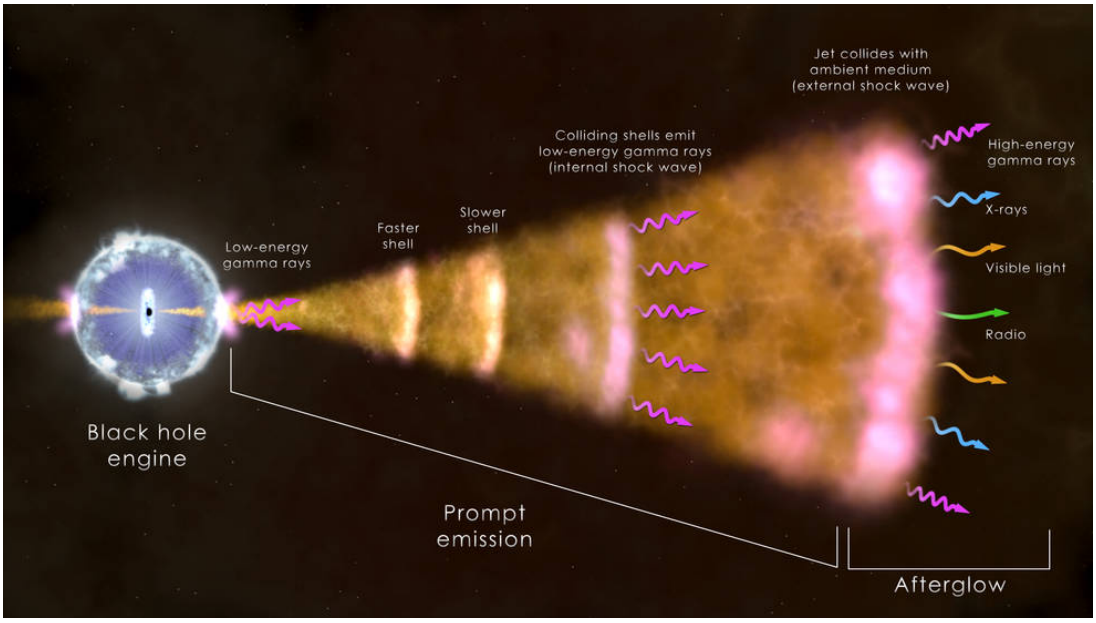

Figure 1.1: Scheme of the most common type of gamma-ray burst, characterized by the prompt and the afterglow phase. Credit: NASA's Goddard Space Flight Center.

$10^{5-9} M_{\odot}$; see, e.g., Netzer, 2015; Kono et al., 2021). These objects can be more luminous ($L_{\rm bol} \approx 10^{48}\ erg/s$; see, e.g., Padovani et al., 2017) than the remaining galaxy light.

Heckman and Best (2014) divided low-redshift AGNs into two categories: the "radiative-mode" and "jet-mode" AGNs. In these categories, the dominant energetic output takes the form of electromagnetic radiation and of bulk kinetic energy transported in two-sided collimated jets, respectively. Heckman and Best (2014) claimed that the electromagnetic radiation in "radiative-mode" AGNs is generated by the conversion of the gas potential energy that is accreted by the SMBH, while jets in "jet-mode" AGNs may derive from gas accretion or they may take advantage of SMBH spin energy.

Jets in AGNs typically extend on scales from AU to Mpc and can be observed from meter wavelengths up to TeV gamma energies, thus requesting multi-messenger campaigns (Blandford et al., 2019). Each spectral band (see Fig. 1.2) is linked to a particular AGN physical process. At either end of the spectra, there are the infrared (IR) band, which is sensitive to dust, and the gamma-ray band, which is indeed related to AGNs non-thermal radiation emitted through jets (Padovani et al., 2017). AGNs jets are commonly accepted to be launched from systems composed of an ac-

cretion disk that surrounds a central object (see, e.g., Pudritz and Ray, 2019, and references therein). It is commonly believed that the magnetic field has a key role in the launching, acceleration, and collimation of jets. However, the origin of the accretion-disk magnetic field is not entirely understood. One of the proposed explanations is that this magnetic field is created by a dynamo process in the disk (see, e.g., Stepanovs and Fendt, 2014; Mattia and Fendt, 2020a,b). As stressed by Tsunetoe et al. (2022), the study on the link between the powerful jet and the central engine has been pushed forward since the first ever image of the shadow of the SMBH in M87 was released by the Event Horizon Telescope (EHT; see Event Horizon Telescope Collaboration et al., 2019). Janssen et al. (2021), for instance, presented EHT observations of the jet launching and collimation in Centaurus A, revealing a highly collimated jet and a fainter counterjet. Tsunetoe et al. (2022) investigated the disk-jet structure in M87 through an analysis concerning the polarization images. Akiyama and Event Horizon Telescope Collaboration (2022) claimed that Sagittarius A*, being the nuclear SMBH in our Galaxy, allows us to elucidate some of the drivers of observed cycles in accretion power and jet launching. These are just a few examples of the latest work on the subject (see also Doeleman et al., 2012; Lu et al., 2014; Chael et al., 2016).

Urry and Padovani (1995) unified jetted AGN with a scheme that takes into account the emission in the radio band, the optical spectrum, and the viewing angle (Foschini, 2017). By considering the last feature, when the viewing angle is large these AGNs are classified as radio galaxies. On the other hand, if the viewing angle is small, AGNs are called Blazars, with relativistic jets pointing towards us. The emitted flux from the blazar jet is amplificated because of the Doppler boosting, and it can dominate the emission from the host galaxy or accretion disc (Morris et al., 2019). As set out in Romero et al. (2017), blazars are characterized by a compact radio core, a high degree of radio and optical polarization, and a intense emission in the gamma-ray band. Blazars are classified as BL Lacertae objects (i.e., BL Lac objects) when their optical emission is weak or even absent, as Flat Spectrum Radio Quasars (i.e., FSRQ) when the optical emission is characterized by the quasars (i.e., QSOs meaning Quasi Stellar Objects) typical emission lines (Romero et al., 2017), or as uncertain/transitional blazars (Massaro et al., 2009). These classification names are linked to the origin of the term blazar. In fact, Angel and Stockman (1980) explained that

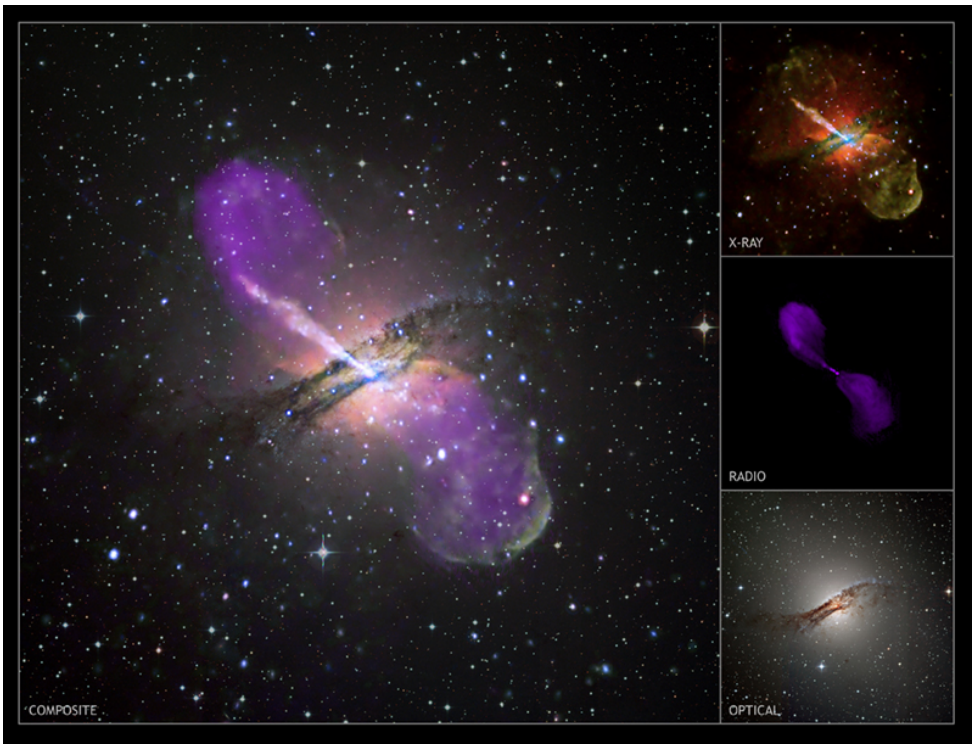

Figure 1.2: Image of the nearby galaxy Centaurus A taken by Chandra Space Telescope. The multi-panel on the right shows the same image in context with optical and radio observations. Credit: X-ray: NASA/CXC/CfA/R.Kraft et al; Radio: NSF/VLA/Univ.Hertfordshire/M.Hardcastle; Optical: ESO/WFI/M.Rejkuba et al.

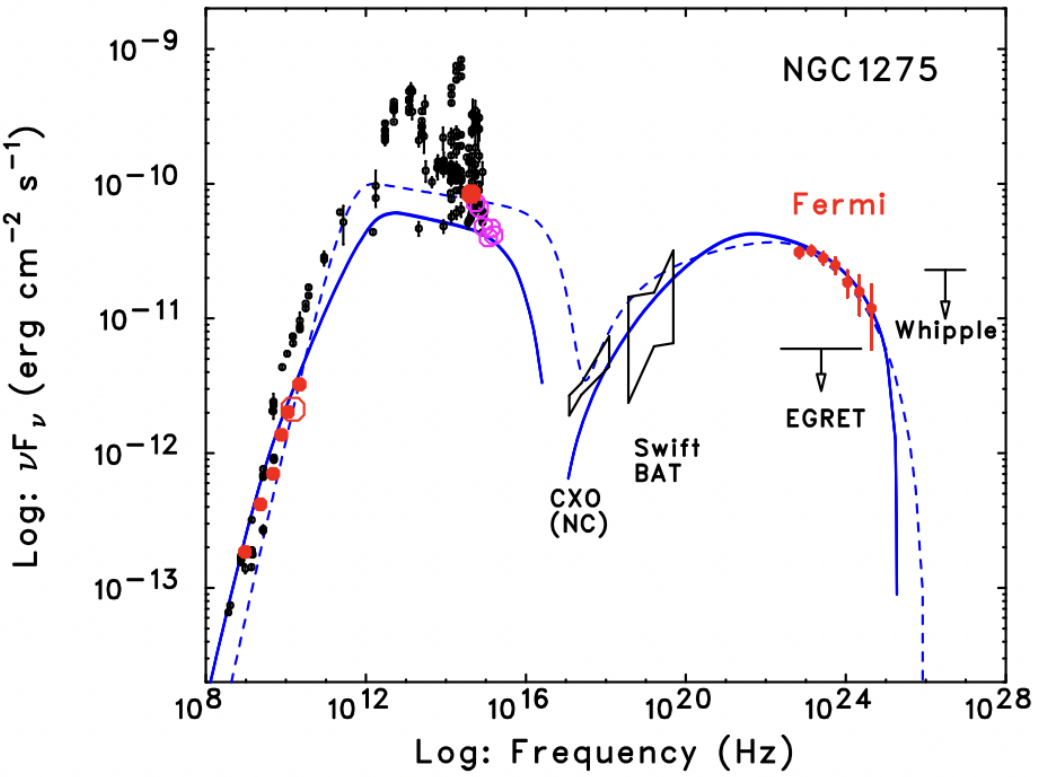

Figure 1.3: Characteristic "double humped" spectral energy distribution (SED) of NGC 1275. Credit: Abdo et al. (2009).

this term derives from the combination of BL Lac object and quasars, done by Ed Spiegel during a banquet speech at the BL Lac objects Pittsburgh meeting.

1.1.3 Characteristic emission spectrum

The non-thermal signature that features AGNs is originated from highly energetic particles undergoing inverse Compton or synchrotron cooling. ANGs, and consequently Blazars, have a characteristic "double humped" continuum emission spectrum (Morris et al., 2019), as shown in Figure 1.3. Radio and soft X-ray emission is attributed to synchrotron emission, while the high-energy part of the spectra is due to the inverse Compton mechanism. Synchrotron radiation is a type of non-thermal emission generated by charged particles spiraling around magnetic field lines, emitting photons with a power given by

$$P_{\text{sync}} = \frac{2e^2}{3c^3}\gamma^2\omega_c^2 v^2 \sin^2\theta = \frac{4}{3}c\sigma_T\beta^2\gamma^2 U_B. \tag{1.1}$$

Equation (1.1) represents the Larmor formula, where $\gamma = 1/\sqrt{1 - v^2/c^2}$ is the Lorentz factor, c is the speed of light, $\omega_c = 2\pi\nu_L$, where $\nu_L = eB/mc$ is the Larmor frequency, θ is the angle between the speed of the particle (i.e., v) and the magnetic field (i.e., B), σ_T is the Thomson cross section, while $U_B = B^2/8\pi$ is the energy density contained in the magnetic field. This applies to a single electron, while for a power-law distribution of electrons the power emitted is equal to

$$P_{\text{sync}} = \frac{2}{3} c\sigma_T n_0 \frac{U_B}{\nu_L} \left(\frac{\nu}{\nu_L}\right)^{-\delta}, \tag{1.2}$$

where n_0 is the electrons' number density, while $\delta = (p-1)/2$ is the spectral index of the synchrotron emission, where p represents the power-law index of the electron energy spectrum. In fact, observations indicate that non-thermal particles possess a power-law distribution of the form $I_f \propto f^{-p}$, with p generally less than 2 (see, e.g., Ishibashi and Courvoisier, 2010, and references therein) for energies over $2 - 10$ keV (see, e.g., Page et al., 2005; Piconcelli et al., 2005).

The radiation emitted is polarised in the plane perpendicular to the magnetic field, with the degree and orientation of the polarisation providing information about the magnetic field of the source.

Condon and Ransom (2016) explained that, although the total radiation field is normally fairly isotropic in the rest frame of a synchrotron source, this radiation field looks extremely anisotropic to the individual ultrarelativistic electrons producing the synchrotron radiation. Indeed relativistic aberration leads almost all ambient photons to approach within an angle $\sim \gamma^{-1}$ rad of head-on (as seen in Fig. 1.4). The electrons kinetic energy is reduced by Thompson scattering and is converted into inverse Compton radiation by upscattering radio photons to become optical or X-ray photons (Condon and Ransom, 2016). These authors claimed that this process also limits the maximum rest-frame brightness temperature of an incoherent synchrotron source to $T_b \approx 10^{12} K$. The power emitted due to the inverse Compton mechanism is given by

$$P_{\text{IC}} = \frac{4}{3} \sigma_T c \beta^2 \gamma^2 U_{\text{rad}}, \tag{1.3}$$

that is very similar to Equation (1.1) apart from U_{rad}, i.e. the radiation energy density. The photons involved in this process can be either those

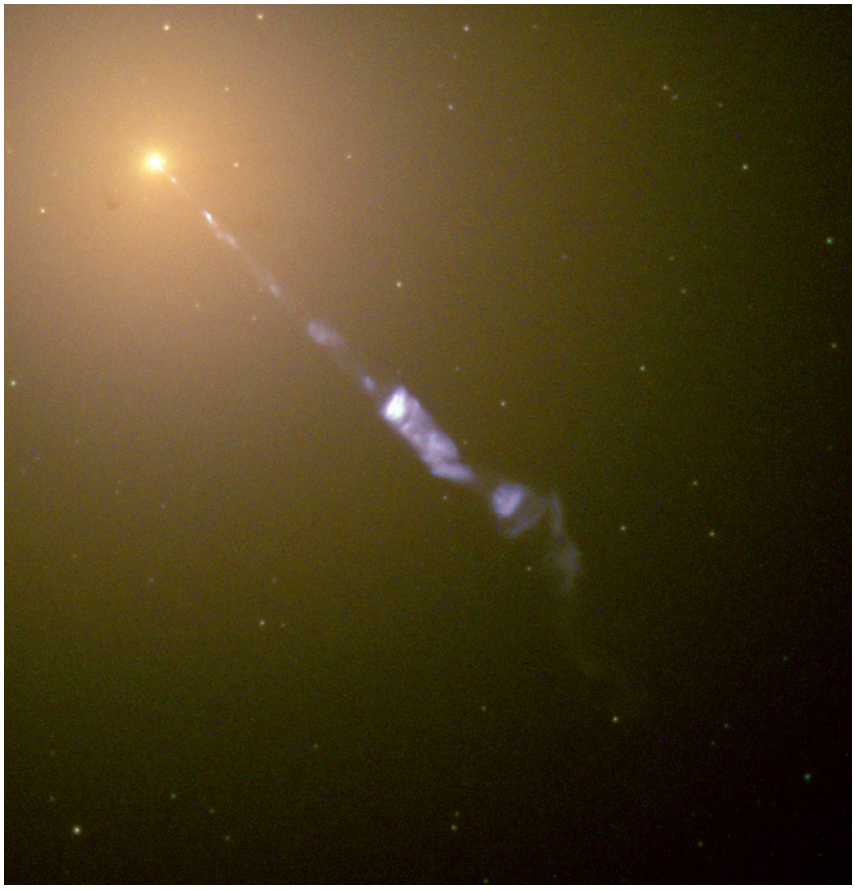

Figure 1.4: AGN jet of the M87 galaxy. The other jet is not visible due to relativistic beaming. Credit: NASA and the Hubble Heritage Team (STScI/AURA).

of the Cosmic Microwave Background (CMB) or the same ones produced by the synchrotron emission (i.e., synchrotron self-Compton).

In addition to radiative losses, the high-energy of cosmic rays is limited by the Hillas criteria for confinement (see Hillas, 1984). Indeed, particles need to stay in the acceleration region to gain more energy. This leads to a limit in their maximum energy, obtained by imposing that the Larmor radius of the particles is smaller than the size of the acceleration region. The particle energization is also limited by the collision with photons from synchrotron radiation, galactic emissions, and cosmic background radiation (Honda, 2009). As claimed by Allard and Protheroe (2009), these interactions lead to features in the propagated spectrum of high-energy cosmic rays such as the Greisen-Zatsepin-Kuzmin (GZK; see Greisen, 1966; Zatsepin and Kuzmin, 1966) cutoff. Binary interactions with the thermal particles of the intracluster medium (ICM) can also cause a loss of cosmic rays energy (see, e.g., Vazza et al., 2013).

As stated in Wang et al. (2014), while the emission mechanisms generating the spectra of blazars are well understood, those for the prompt phase of GRBs are still under debate, even if models have been proposed (see, e.g., Giannios, 2008). The synchrotron radiation is the leading emission mechanism for the afterglow phase (see, for instance, Sari et al., 1998, and references therein). Indeed, the afterglow is produced by the synchrotron radiation from the deceleration of the GRB remnant by the collision with the external medium (Panaitescu and Kumar, 2001). Sironi and Giannios (2013) investigated the temporal decay of the afterglow GRBs emission at late times. Figure 1.5 shows some examples of GRBs spectra.

GRBs and AGNs emission shows variability. AGNs are characterized by variability on the entire electromagnetic spectrum with time-scales from decades to minutes (Zhang et al., 2022), while the gamma-rays flux emitted by GBRs during the prompt phase varies on $\lesssim 1\ s$ time-scales (Lloyd-Ronning et al., 2016).

What is known at the moment of these astrophysical sources is what can be observed experimentally, i.e., their spectra. It is of crucial importance to have a real comparison between the theoretical models and the observed data to fully understand how the particles really accelerate and produce the emission spectra that we observe.

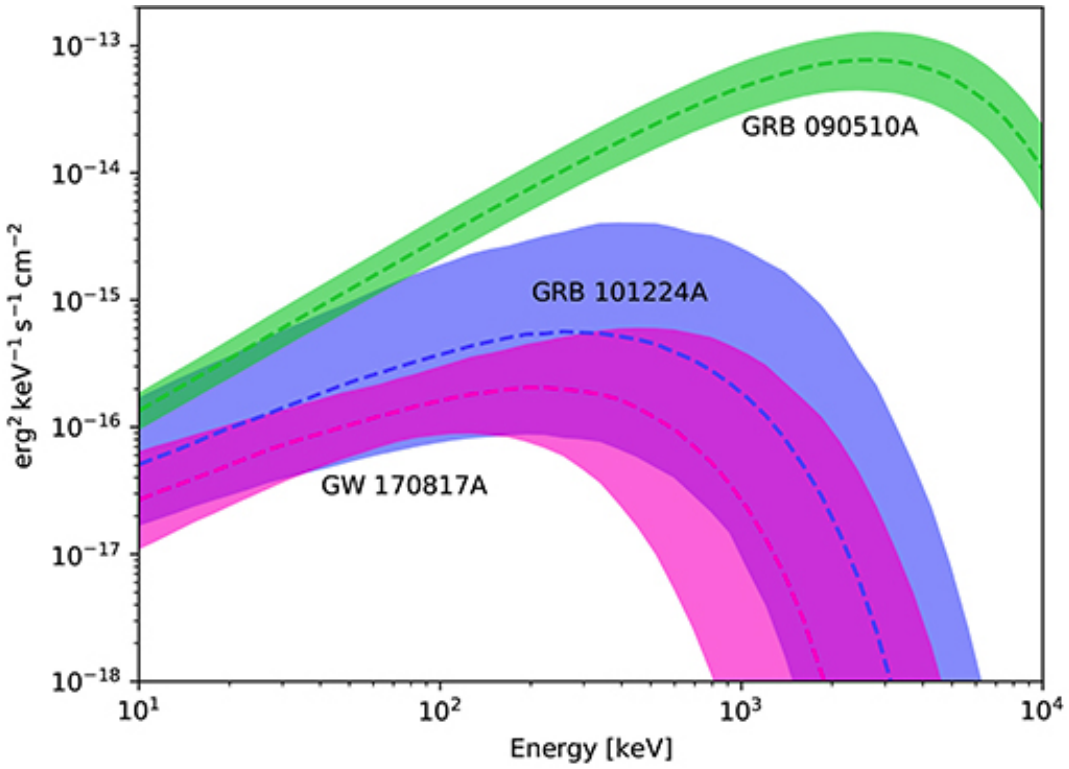

Figure 1.5: Comparison of gamma-ray spectrum of GRB 170817A, GRB 101224A, and GRB 090510A. Credit: Burgess et al. (2020).

1.2 How are particles accelerated?

It is often believed that particle acceleration is profoundly affected by plasma turbulence and that shocks are the major acceleration sites, although magnetic reconnection in current sheets has been recently pointed out as an efficient energization process (see, e.g., Lazarian et al., 2012; Guo et al., 2014, 2015; Sironi and Spitkovsky, 2014; Sironi et al., 2015). Indeed, it has often been proven that relativistic magnetic reconnection produces power-law spectra of energetic non-thermal particles (see, e.g., Guo et al., 2014; Sironi and Spitkovsky, 2014) and time-variability compatible with observations. In particular, a magnetic reconnection regime with time-scales comparable to the ones observed in astrophysical plasmas can be triggered by dynamical instabilities as the tearing mode (TM). Therefore, it is of paramount importance to investigate how the dynamical evolution of this instability can lead to the formation of magnetized current sheets, which, in turn, are responsible for particle acceleration.

1.2.1 Diffusive shock acceleration

Fermi (1949) first proposed that cosmic rays are accelerated primarily by collisions against magnetic fields in motion in the interstellar medium. This mechanism can occur in shock waves, under the name of diffusive shock acceleration (DSA). As explained in Vainio (1999), particles cross the shock many times and gain energy each time by scattering off the magnetic turbulence. As it passes, the shock amplifies the irregularities of the magnetic field. The variation of the magnetic field generates an electric field, which accelerates the particles. The acceleration time scale is proportional to the number of reflections between the two shock regions: the upstream and the downstream (Hoshino, 2001), shown in Figure 1.6. When a particle crosses a shock that is moving at the velocity v_s, it gains an energy of the order $\Delta\epsilon/\epsilon = v_s/c$.

The observations are modeled well, as such a diffusive process naturally produces a power-law particle spectrum (Baring, 1997). DSA occurs in collisionless shocks characterizing astrophysical environments such as the non-relativistic supernova remnant (SNR) shocks, which are often considered as sources of galactic cosmic rays (CRs; see, e.g., Caprioli et al., 2010; Morlino and Caprioli, 2012). In fact, an exploding supernova sends a shock

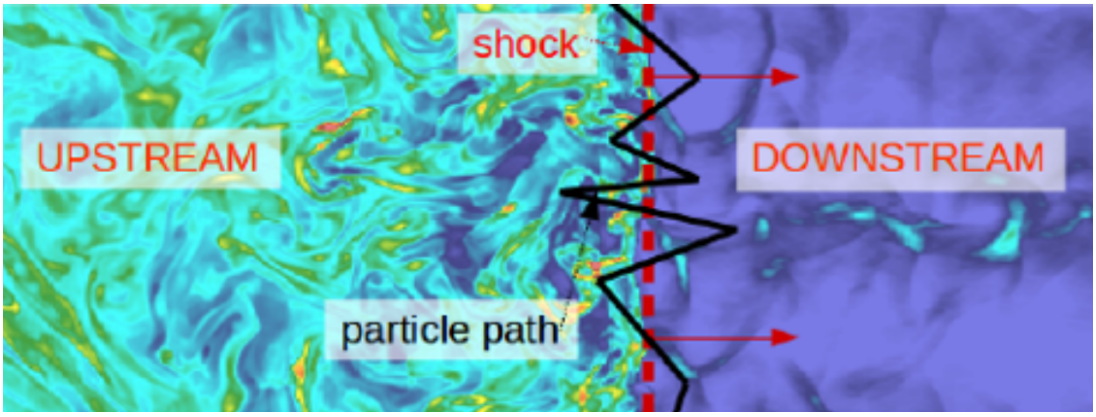

Figure 1.6: Particle path through the shock from upstream to downstream and vice versa. Credit: A. Mignone.

into outer space, which propagates by accelerating the particles it encounters through DSA. The problem with this acceleration mechanism is that the electric field, which accelerates particles, is stochastic, very variable, and not so strong. Therefore, DSA in supernovae is not the main CRs acceleration mechanism. Indeed, Sironi et al. (2015) showed that although shocks are efficient energy dissipators, they do not energize particles far beyond the thermal energy. A more promising particle acceleration mechanism is magnetic reconnection.

1.2.2 Magnetic reconnection

As claimed by Zweibel and Yamada (2016), magnetic fields are ubiquitous in the cosmos, and one of the most important basic processes that occur in almost all the magnetized plasmas is magnetic reconnection. This process plays a fundamental role in solar, space, and astrophysical problems (see the review of Yamada et al., 2010). Figure 1.7 shows a sketch of the configuration of magnetic field lines in the reconnecting current sheet: the magnetic field has one component that reverses its polarity along the x-axis. Such a field can be established by a current sheet $\mathbf{J}$ moving on an infinite plane, perpendicular and outgoing from the page. Lorentz force $\mathbf{J} \times \mathbf{B}$ pulls plasma to the B-neutral region (i.e., the green line), since equilibrium is established. During the magnetic reconnection process, fields of opposite polarities rapidly annihilate and the magnetic energy is converted into kinetic and thermal energy of the plasma becoming, at the same time, available in creating a non-thermal population of accelerated

particles. Magnetic field lines are indeed cut and sewn together and plasma blobs are ejected, as observed on the Sun.

For this mechanism to operate, the plasma cannot be ideal (i.e., non-resistive) and the Alfvén theorem does not hold: field lines should be able to change their topology. Albeit astrophysical plasmas are essentially ideal, the flow evolution may lead to the formation of localized regions of large gradients and electric currents, where resistivity cannot be any longer neglected since its role becomes essential in the energy and momentum balance (see, e.g., Uzdensky, 2011, 2016; Giannios, 2013; Mignone et al., 2019).

The formation of strong and localized current sheets favors reconnection events during which the magnetic field topology may break becoming favorable to resistive instabilities such as the tearing one. Sweet (1958) and Parker (1957) model describes magnetic reconnection, although it predicts reconnection rates that are several orders of magnitude slower than the observed ones, especially when the Lundquist number $S = Lv_A/\eta$ is large (here L is the characteristic length of the system, v_A is the Alfvén velocity and η is the physical resistivity). It is a well-known fact that, for astrophysical or laboratory highly-conducting plasmas, $S \gg 1$ (e.g., $S = 10^{12}$ in the solar corona), classical steady-state models fail to predict the observed bursty phenomena such as solar flares or tokamak disruptions, which occur instead on a non-negligible fraction (say not less than $\sim 10\%$) on the ideal (Alfvénic) time-scales (see, e.g., Marcowith et al., 2020). However, a different picture emerges when magnetic reconnection occurs as a time-dependent and unstable process triggered by the tearing mode instability.

1.2.3 Tearing instability

When magnetic reconnection occurs by magnetic diffusion the process is slow, as in the Sweet-Parker model, but if instability occurs, the process takes place more quickly. Indeed, a magnetic reconnection regime with time-scales comparable to the ones observed in astrophysical plasmas can be triggered by dynamic instabilities as the tearing mode (TM), which are now considered as byproducts of instabilities acting at larger scales, such as the Kelvin-Helmholtz (KH; see, e.g., Loureiro et al., 2013), and current-driven (CD; see, e.g., Striani et al., 2016) instabilities.

The TM instability fragments an initially neutral current sheet into a num-

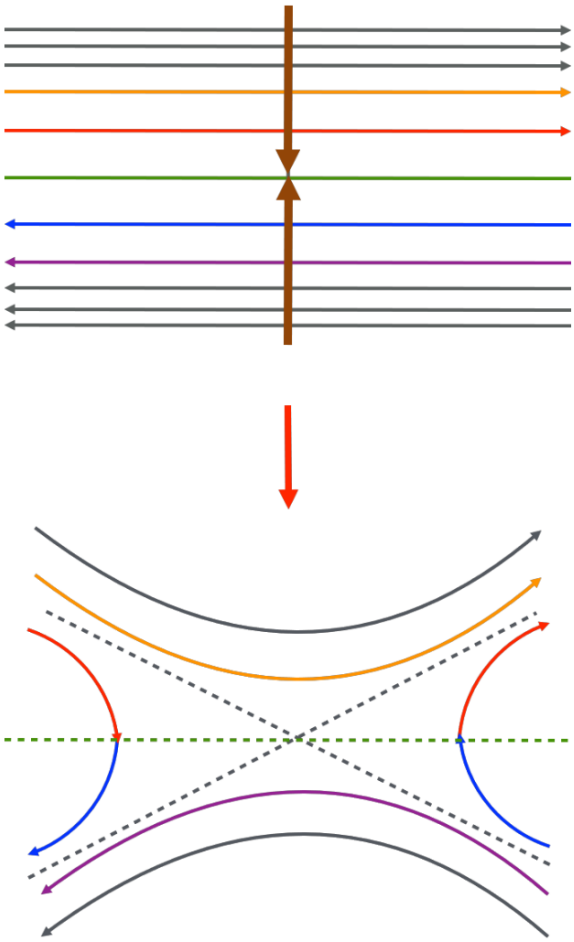

Figure 1.7: A sketch of the initial (top panel) and final (bottom panel) configuration of magnetic field in the reconnecting current sheet. Credit: E. Beratto.

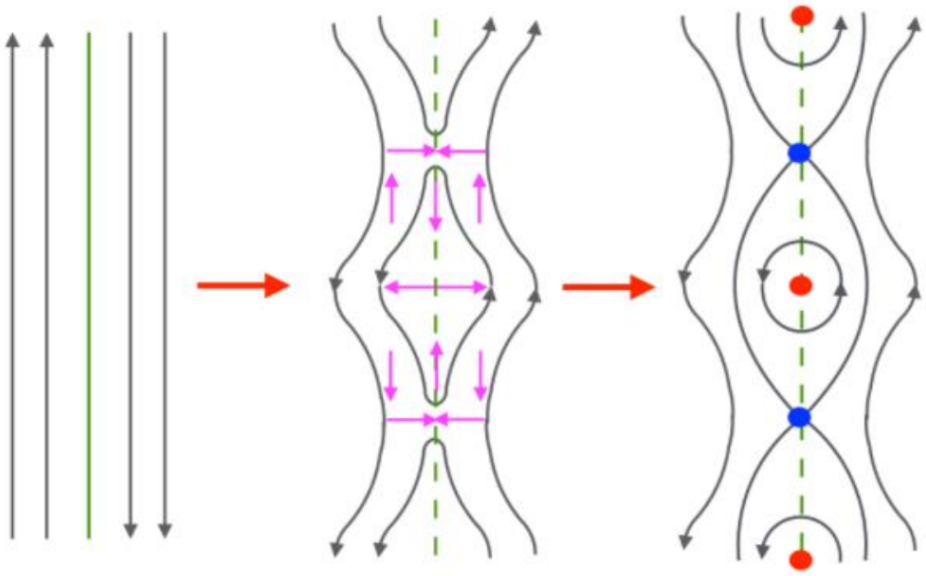

Figure 1.8: A sketch of the initial neutral current sheet fragmented in X-points (blue dots) and O-points (red dots) due to the tearing instability. Credit: E. Beratto.

ber of X-points, where field lines cross each other, and O-points, surrounded by magnetic islands (see Fig. 1.8). In the X-points, the magnetic field has null points, while the electric field is very intense. The O-points (often called plasmoids) are regions of high current density.

Following Loureiro and Uzdensky (2016), it is now generally accepted that the tearing instability radically changes magnetic reconnection, which becomes intrinsically time-dependent, bursty, and fast compared to the Sweet-Parker steady-state model. The precise criteria for the onset of the fast reconnection regime, in which the tearing instability occurs basically on the Alfvénic time-scales, has been numerically investigated in various regimes by Landi et al. (2015) (non-relativistic case), Del Zanna et al. (2016) (relativistic case) and Papini et al. (2019) (Hall regime).

Particle energization via magnetic reconnection can either occur by a direct acceleration at X-points due to the strong electric field (see, e.g., Bessho and Bhattacharjee, 2007; Lyubarsky and Liverts, 2008; Ball et al., 2019), or by the anti-reconnection electric field due to the merging of plasmoids (see, e.g., Oka et al., 2010; Sironi and Spitkovsky, 2014; Nalewajko et al., 2015), or because particles are trapped in contracting magnetic islands due to the Fermi reflection (see, e.g., Drake et al., 2010; Kowal et al., 2011; Petropoulou and Sironi, 2018; Hakobyan et al., 2021).

1.2.4 The debate on the importance of resistivity

Particles are accelerated by the plasma electric field, which consists of a convective and a resistive term, associated with different acceleration mechanisms. Indeed, X-points are characterized by the presence of a resistive electric field, while the Fermi reflection is associated with the convective electric field.

Which of the two electric field terms dominates in accelerating particles is to date still under debate. Kowal et al. (2011) and other authors (see, e.g., Kowal et al., 2012; de Gouveia Dal Pino and Kowal, 2015; del Valle et al., 2016; Medina-Torrejón et al., 2021) directly neglected the contribution of the resistive field in the particle acceleration mechanism, as they considered it unimportant. In Guo et al. (2019) and Paul and Vaidya (2021) it is claimed that the Fermi mechanism is the dominant one in the acceleration process, while the crossing of an X-point makes a small contribution to the global energization. In particular, Guo et al. (2019) argued that the non-ideal field does not contribute even to the formation of the power-law, but it is only the Fermi mechanism that determines the spectral index.

On the contrary, Onofri et al. (2006) and Zhou et al. (2016) claimed that, even if the resistive contribution is less intense than the convective one, it is much more important in accelerating particles. The results of Zhou et al. (2016) were later confirmed by Ripperda et al. (2017a). In addition, in Ball et al. (2019) it is claimed that the particle acceleration mechanism is more efficient when more X-points are formed on the current sheet. Recently, Sironi (2022) argued that the acceleration from the non-ideal electric field is a basic requirement for subsequent acceleration, which is, on the contrary, typically dominated by the ideal field (as claimed by Guo et al., 2019). Indeed, particles that do not undergo the non-ideal contribution do not even reach relativistic energies. The results of this thesis favorably agree with these last authors, who support the importance of the resistive electric field.

First thesis aim: quantify the relative importance of the resistive and convective electric field in the particle acceleration process to understand if, when, and why one contribution prevails over the other.

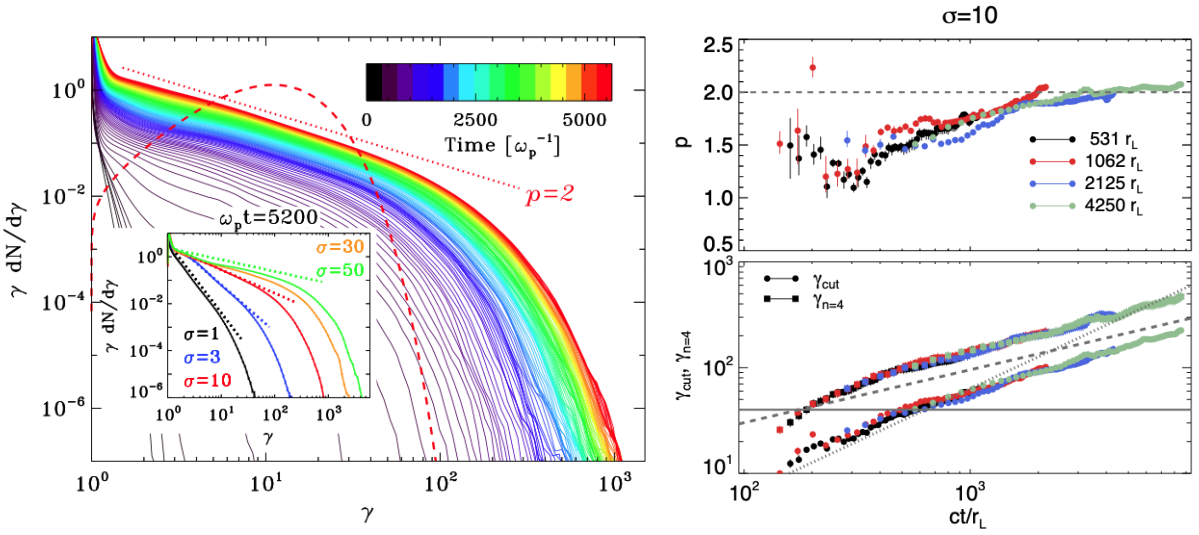

Figure 1.9: *Left panel*: Evolution over time of particle energy spectrum obtained through PIC simulation with different magnetization. *Right panel*: Evolution over time of the spectrum power-law index (top panel), of the cutoff Lorentz factor and the maximum Lorentz factor (bottom panel). Credit: Sironi and Spitkovsky (2014) (left panel), Petropoulou and Sironi (2018) (right panel).

1.3 Previous results on particle acceleration

The last decade has provided a wealth of investigations, mostly through magnetohydrodynamic (MHD) or particle-in-cell (PIC) numerical simulations. These approaches model the large and small scales of high-energy astrophysical environments, respectively. The advantage of the PIC approach (which lacks the MHD one) is the ability to capture the kinetic effects relevant at small scales. However, these scales are much smaller than the typical size of high-energy astrophysical environments. Hence, PIC simulations are extremely expensive in describing these astrophysical systems at larger scales (as opposed to MHD ones). Nevertheless, the simulation results obtained with both methods indicate relativistic magnetic reconnection as a very promising candidate in the process of particle acceleration.

1.3.1 Test-particles MHD versus PIC

Through PIC simulations, Sironi and Spitkovsky (2014), and likewise Petropoulou and Sironi (2018), found that accelerated particles populate a power-law distribution with a spectral slope $p \sim 2$ in a pair plasma (see Fig. 1.9). Such studies have been widened to the fluid regime using

MHD simulations in conjunction with a test-particle approach (see, e.g., Gordovskyy et al., 2010a,b; Kowal et al., 2011; de Gouveia Dal Pino and Kowal, 2015; Ripperda et al., 2017a,b), finding results similar to those obtained with PIC simulations in terms of particle acceleration. This has been suggested, e.g. by Kowal et al. (2011), who have found that in 2D MHD models during an island contraction (due to the merger with other islands) a particle trapped in it can accelerate and increase its energy exponentially in a non-relativistic scenario. This is similar to what Drake et al. (2010) have found with a PIC approach (see Fig. 1.10). This bulk of evidence suggests that magnetic reconnection can be more efficient and universal when compared to other mechanisms, such as varying magnetic fields in compact sources, and the first-order Fermi process behind shocks (Kowal et al., 2011).

Test-particles acceleration in MHD is usually studied by using frozen snapshots (see, e.g., Gordovskyy et al., 2010a; Kowal et al., 2011; de Gouveia Dal Pino and Kowal, 2015; Ripperda et al., 2017a), in which the fluid provides a background, static configuration on top which particles are allowed to evolve. In contrast with these investigations, test-particles and MHD fluid will be evolved simultaneously in this thesis work, with the advantage of studying the acceleration mechanism in response to the dynamical evolution of the system, as done by Gordovskyy et al. (2010b), Kowal et al. (2012), and Ripperda et al. (2017b, 2019b).

1.3.2 Shortcomings

Except for very few works (see, e.g., Kowal et al., 2009; Santos-Lima et al., 2010; Rembiasz et al., 2017), however, the vast majority of these studies largely overlook the impact of the numerical method on the simulation results, it scarcely addresses the problem of convergence concerning grid resolution and it often neglects the effect of a physical resistivity on the evolution of the instabilities. Classical and relativistic MHD numerical simulations have, in fact, shown that when the Lundquist number S is greater than a certain threshold value, plasma instabilities in the current sheet trigger a fast reconnection regime with time-scales comparable to the observed ones. However, the grid resolution must be sufficiently large to ensure that the dissipation scale is regulated by physical resistivity and not by numerical diffusion. This requirement, together with the low-resistivity

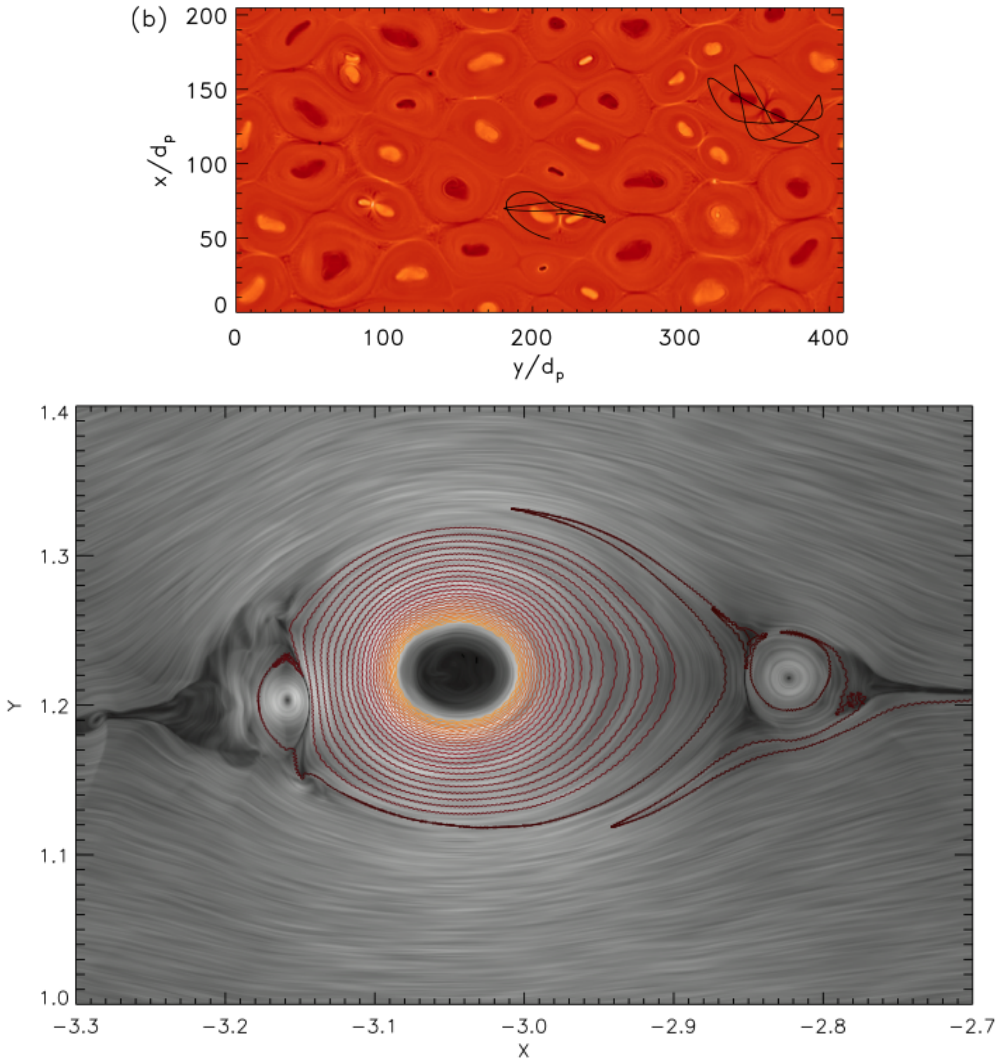

Figure 1.10: *Top panel*: Test protons trajectories in the PIC simulation fields. *Bottom panel*: Test proton trajectory inside a magnetic contracting island (merging with other two small islands), obtained through MHD simulations. Credit: Drake et al. (2010) (top panel), Kowal et al. (2011) (bottom panel).

(or high S, typically $S > 10^3$) typical of astrophysical plasma, can indeed demand a very fine mesh spacing in the proximity of the current sheet. This determines the numerical convergence of the simulation and eventually regulates the correct reconnection rate, once the proper numerical resolution is achieved.

Second thesis aim: assess the impact of numerical method, grid resolution, and physical resistivity on the magnetic reconnection process as well as their implications in the particle acceleration mechanisms.

1.4 Outline of the thesis

In this thesis, we focus on the impact of the numerical method on the magnetic reconnection process and particle acceleration mechanism, as well as the importance of the physical resistivity in accelerating high-energy particles.

Chapter 2 describes the theoretical model. Indeed, the fundamental plasma parameters are introduced, as well as the different plasma models with a focus on the MHD model. The particle equations of motion are also discussed.

Chapter 3 introduces the numerical model. First, we briefly discuss the several numerical approaches generally used in this context, and then we describe the code used to carry out the simulations presented in this thesis work: the PLUTO code. Finally, we discuss our numerical setup.

Chapter 4 investigates the impact of the numerical method and resistivity on magnetic reconnection and particle acceleration. Indeed, we discuss the effect of the spatial reconstruction scheme, the Riemann solver, the emf averaging scheme, and the Lundquist number both on the plasma evolution and on the particle acceleration mechanism. This chapter is based on the published work of Puzzoni et al. (2021).

Chapter 5 describes the importance of the resistive electric field contribution in accelerating particles. First, we briefly discuss the convergence of our simulations using a 2D histogram analysis. Then, we focus on the resistive field role in accelerating high-energy particles by observing their

spectra. Finally, we analyze the impact of the current sheet evolution on particle energization. This chapter is based on the published work of Puzzoni et al. (2022).

Chapter 6 summarizes and discusses the most important results of this thesis and the plans for future research.

2

Theoretical model: plasma definition and equations

"Plasma is a system whose dynamics are dominated by electromagnetic forces, as it is the ensemble of charged particles and the fields they generate" (Chiuderi and Velli, 2012). After solid, liquid, and gas, plasma is considered the 4$^{\text{th}}$ *state of matter* (Frank-Kamenetskii, 1972). This state is achieved by heating a gas to the point where electrons separate from positively charged ions. It is estimated that about 99% of the known universe is made up of plasma, which is why it is a topic that arouses more and more interest. In this chapter, after an introduction to some of the fundamental parameters of plasma and its kinetic description, the non-relativistic magnetohydrodynamic model is discussed, together with the particle equations of motion.

2.1 Basic plasma parameters

Since electrons in the plasma are free moving, they will collide with ions, marked by index i, and atoms, marked by index a, with a frequency

$$\nu_c = \alpha^i n_i \left(1 + \frac{\alpha^a}{\alpha^i}\frac{1-\chi}{\chi}\right), \tag{2.1}$$

where n is the number density, $\alpha = \sigma_c \bar{v}$ (with $\bar{v}$ the average electron velocity and σ_c the cross section), while $\chi = n_i/(n_i + n_a)$ represents the degree of ionization ($0 < \chi < 1$). This frequency appears in the definition of electrical conductivity, namely

$$\sigma = \frac{e^2 n_e}{m_e \nu_c} = \frac{Ze^2}{m_e \alpha^i}\frac{1}{1 + \frac{\alpha^a}{\alpha^i}\frac{1-\chi}{\chi}} = \frac{\sigma_{\max}}{1 + \frac{\alpha^a}{\alpha^i}\frac{1-\chi}{\chi}}, \tag{2.2}$$

where Ze represents the ion charge, m_e is the electron mass and $\sigma_{\max}$ is the maximum value of electrical conductivity, achieved at $\chi = 1$. An electrical

conductivity that is half that of completely ionized gas is obtained with a χ of the order of 1% (Chiuderi and Velli, 2012).
The state of ionization is described by the *Saha equation*, that is

$$\frac{n_i}{n_0} \simeq 2.4 \cdot 10^{15} \frac{T^{3/2}}{n_i} e^{-I/kT}, \tag{2.3}$$

where n_0 and n_i are the number density of the ground state and of the i^{th} state of ionization respectively, T is the plasma temperature, I represents the energy of ionization, and k the *Boltzmann constant*.
In addition to being ionized, a plasma must satisfy the condition of *quasi-neutrality*. Indeed, the charge of a particle tends to be shielded by the presence of charged particles of opposite signs that surround it, as they are free to move. The scale at which this occurs is called the *Debye length*, namely

$$\lambda_D = \sqrt{\frac{kT}{4\pi e^2 n_0}}, \tag{2.4}$$

where n_0 is the density without the surrounding particles (i.e., the unperturbed state). In order to achieve *quasi-neutrality*, the condition $\bar{d} \ll \lambda_D$ must be satisfied, where $\bar{d}$ is the average distance between particles. Since $\bar{d} \simeq n^{-1/3}$, the previous condition becomes

$$n\lambda_D^3 \gg 1. \tag{2.5}$$

This means that the plasma must be composed of many particles to achieve the *quasi-neutrality* condition.
A characteristic velocity of the particles is the *thermal velocity*, that is

$$v_T = \sqrt{\frac{3kT}{m}}. \tag{2.6}$$

This equation indicates that, at the same temperature T, electrons have a higher thermal velocity, as it depends on mass. Particles reach the same temperature through collisions. This process is called *thermalization*. The collision rate can be written as

$$\nu_c = n\sigma_c v_T \propto \frac{n}{T^{3/2}\sqrt{m}}. \tag{2.7}$$

The time in which populations of particles reach thermodynamic equilibrium through collisions is $\tau \sim \nu^{-1}$, therefore

$$\frac{\tau_{ee}}{\tau_{ii}} \sim \frac{\nu_{ii}}{\nu_{ee}} \sim \sqrt{\frac{m_e}{m_i}} \ll 1, \tag{2.8}$$

if collisions between electrons (suffix ee) and between ions (suffix ii) are considered. As a consequence, the electrons thermalize before the ions ($\tau_{ee} \ll \tau_{ii}$). If collisions between ions and electrons are also considered, the scale of times is $\tau_{ee} \ll \tau_{ii} \ll \tau_{ie}$ (Chiuderi and Velli, 2012).
Another important plasma parameter is the *plasma frequency*, given by

$$\omega_p = \sqrt{\frac{4\pi e^2 n}{m}}, \tag{2.9}$$

which is again different in the case of protons and electrons, as it depends on the mass and charge of the particle. Particles perform a harmonic motion with frequency ω_p as a reaction to a perturbation to which the plasma is subjected, such as the local violation of charge neutrality (Chiuderi and Velli, 2012). This frequency, together with the speed of light c, is related to *plasma skin depth* $c/\omega_{p,e}$, which is the depth in plasma to which electromagnetic radiation can penetrate and the wave amplitude is attenuated by a factor of $1/e$ (Stenson et al., 2017).
When a charged particle moves in a magnetic field of module B, it performs a circular motion with a frequency

$$\omega_c = \frac{eB}{mc}, \tag{2.10}$$

that is the *cyclotron frequency* or *Larmor frequency*, related to *Larmor radius* or *gyroradius* c/ω_c.
In magnetized plasma, a magnetic perturbation propagates with the *Alfvén velocity*, which is another fundamental plasma parameter and it is defined by

$$v_A = \frac{B}{\sqrt{4\pi\rho}}, \tag{2.11}$$

where ρ is the plasma density.
In the presence of a magnetic field, a magnetic pressure is added to the gas pressure P, and it is the *β-parameter*

$$\beta = \frac{P}{B^2/8\pi} \tag{2.12}$$

that establishes which of the two pressures dominates the other:

- if $\beta \ll 1$ the magnetic field determines the motion and so it draws the plasma,
- if $\beta \gg 1$ the pressure forces determine the motion and so it is the plasma that draws the magnetic field.

2.2 Plasma kinetic description

When the system is made up of a very large number of particles N, it becomes impossible to solve the equations of motion of the particles, that is to know their position $\mathbf{x}$ and their velocity $\mathbf{v}$ at any instant of time. Therefore, a statistical approach is preferred, in which all particles are described by the distribution function $f(\mathbf{x}, \mathbf{v}, t)$. In this way, the total number of particles is given by

$$N(t) = \int_V f(\mathbf{x}, \mathbf{v}, t) dx^3 dv^3, \tag{2.13}$$

where V represents the phase space volume. The number of particles is conserved, so N obeys a conservation law and f, therefore, to the continuity equation

$$\partial_t f + \mathbf{v} \cdot \nabla_x f + \mathbf{a}_{\text{glob}} \cdot \nabla_v f = \left(\frac{\partial f}{\partial t} \right)_{\text{coll}}. \tag{2.14}$$

The continuity equation assumes this form because the force is divided into two parts: a global contribution due to all the forces generated by the plasma ($\mathbf{a}_{\text{glob}}$), and a collisional term due to the collision between pairs of particles $(\partial f/\partial t)_{\text{coll}}$. In the case of a collisionless plasma (which is typical of many, although not all, astrophysical plasma), Equation (2.14) becomes the *Vlasov equation* (see Vlasov, 1968)

$$\partial_t f + \mathbf{v} \cdot \nabla_x f + \mathbf{a}_{\text{glob}} \cdot \nabla_v f = 0. \tag{2.15}$$

It becomes the *Boltzmann equation* if there is a neutral gas instead of a plasma, namely

$$\partial_t f + \mathbf{v} \cdot \nabla_x f + \mathbf{a}_{\text{glob}} \cdot \nabla_v f = \left(\frac{\partial f}{\partial t} \right)_{\text{Boltz}}. \tag{2.16}$$

In this case, elastic binary collisions between particles are dominant. If the plasma is collisional, the Equation (2.14) becomes the *Fokker-Planck equation*

$$\partial_t f + \mathbf{v} \cdot \nabla_x f + \mathbf{a}_{\text{glob}} \cdot \nabla_v f = \left(\frac{\partial f}{\partial t} \right)_{\text{coll}}, \tag{2.17}$$

in which the right-hand side of the equation is very different as there are collisions between one particle and all the others, not only between two particles. In fact, each particle within the *Debye sphere* interacts with

many particles at the same time. Therefore, the total deflection it undergoes is the result of many small deviations rather than a single interaction (Chiuderi and Velli, 2012). The global contribution in Equation (2.15) is given by

$$\mathbf{a}_{\text{glob}} = \frac{q}{m}\left(\mathbf{E} + \frac{\mathbf{v}}{c} \times \mathbf{B}\right), \tag{2.18}$$

where q and m are the particle charge and mass, respectively. Therefore the *Vlasov equation* for electrons, marked with suffix e, and positive ions, marked with suffix i, becomes

$$\begin{aligned} \frac{\partial f_e}{\partial t} + \mathbf{v}_e \cdot \nabla f_e - e\left(\mathbf{E} + \frac{\mathbf{v}_e}{c} \times \mathbf{B}\right) \cdot \frac{\partial f_e}{\partial \mathbf{p}} = 0, \\ \frac{\partial f_i}{\partial t} + \mathbf{v}_i \cdot \nabla f_i + Z_i e\left(\mathbf{E} + \frac{\mathbf{v}_i}{c} \times \mathbf{B}\right) \cdot \frac{\partial f_i}{\partial \mathbf{p}} = 0, \end{aligned} \tag{2.19}$$

where e is the electron charge, c the speed of light, Z the atomic number and $\mathbf{p}$ is the momentum given by the product of the particle mass m and velocity $\mathbf{v}$. The electric $\mathbf{E}$ and magnetic $\mathbf{B}$ fields are given by *Maxwell's equations*, namely

$$\begin{aligned} \nabla \times \mathbf{B} &= \frac{4\pi\mathbf{J}}{c} + \frac{1}{c}\frac{\partial \mathbf{E}}{\partial t}, \\ \nabla \times \mathbf{E} &= -\frac{1}{c}\frac{\partial \mathbf{B}}{\partial t}, \\ \nabla \cdot \mathbf{E} &= 4\pi\rho, \\ \nabla \cdot \mathbf{B} &= 0, \end{aligned} \tag{2.20}$$

where the density is given by

$$\rho = e\int (Z_i f_i - f_e) d^3p, \tag{2.21}$$

while the current density is equal to

$$\mathbf{J} = e\int (Z_i f_i \mathbf{v}_i - f_e \mathbf{v}_e) d^3p. \tag{2.22}$$

Equations (2.19) and (2.20) form the *Vlasov-Maxwell system.* The electric and magnetic fields, therefore, depend on the distribution function f (i.e., on particle motion).

2.3 Towards the fluid model

The distribution function f, however, cannot always be measured (even if for the solar wind this was done with probes), so the moments of the distribution function are considered, giving up particle velocity information. The aim is to find differential equations in which only the moments of f appear, namely

$$\frac{\partial}{\partial t}(n\langle\psi(\mathbf{v})\rangle)+\nabla\cdot(n\langle\psi(\mathbf{v})\mathbf{v}\rangle)-n\mathbf{a}_{\text{glob}}(\mathbf{x})\cdot\langle\nabla_v\psi(\mathbf{v})\rangle-\frac{ne}{mc}\langle\mathbf{v}\times\mathbf{B}\cdot\nabla_v\psi(\mathbf{v})\rangle=\mathcal{C}. \tag{2.23}$$

This equation characterized the so-called *two-fluid plasma model*. Indeed, a plasma is composed of electrons and protons that collide, therefore the collisional terms (in $\mathcal{C}=\int\psi(\mathbf{v})(\partial f/\partial t)_{\text{coll}}d\mathbf{v}=(\partial_t(n\langle\psi\rangle))_{\text{coll}}$) cannot be considered null and must be classified according to the species of the particles. $\psi(\mathbf{v})$ is an arbitrary function of the velocity $\mathbf{v}$, whose average value is given by

$$\langle\psi(\mathbf{v})\rangle=\frac{1}{n}\int\psi(\mathbf{v})f(\mathbf{x},\mathbf{v},t)d\mathbf{v}, \tag{2.24}$$

where

$$n(\mathbf{x},t)=\int f(\mathbf{x},\mathbf{v},t)d\mathbf{v} \tag{2.25}$$

is the number density. In Equation (2.23) the information on the three components of velocity is lost, but the one on the three spatial dimensions and the temporal one is maintained. By considering $\psi(\mathbf{v})=m$, $\psi(\mathbf{v})=m\mathbf{v}$ and $\psi(\mathbf{v})=mv^2/2$, the continuity, momentum and energy equations are obtained respectively. In this way, the moments of the distribution function f are the solutions of the equation, without referring to f itself.
The substitution of the $0^{\text{th}}-$, $1^{\text{st}}-$ and $2^{\text{nd}}-$order moment in Equation (2.23) leads to 16 scalar differential equations (2 continuity equations, 2×3 components of momentum equations, 2 energy equations, 2×3 components of Maxwell equations) and 2 algebraic equations (the equations of state), for 18 unknowns (2 densities, 2×3 components of velocities, 2 pressures, 3 components of the electric field, 3 components of the magnetic field and 2 specific energies). Therefore, this model is not convenient to use because of the many equations to solve. For this reason, it is convenient to define a single-fluid model.
The *single-fluid plasma model* considers a single fluid made of electrons

(suffix e) and protons (suffix p), that moves with a total fluid velocity

$$\mathbf{v} = \frac{\rho_e \mathbf{v}_e + \rho_p \mathbf{v}_p}{\rho_e + \rho_p}. \tag{2.26}$$

The mass density of the fluid is

$$\rho = m_e n_e + m_p n_p \simeq m_p n_p, \tag{2.27}$$

as $m_p n_p \gg m_e n_e$, with $n = n_e + n_p$ representing the number density. The charge density is given by

$$q = e(n_p - n_e), \tag{2.28}$$

while

$$\mathbf{J} = e(n_p \mathbf{v}_p - n_e \mathbf{v}_e) \tag{2.29}$$

represents the current density. By following this approach, the obtained mass continuity, charge continuity, momentum, and energy equations are

$$\begin{aligned}
&\frac{\partial \rho}{\partial t} + \nabla \cdot (\rho \mathbf{v}) = 0, \\
&\frac{\partial q}{\partial t} + \nabla \cdot \mathbf{J} = 0, \\
&\rho \frac{d\mathbf{v}}{dt} + \nabla \cdot \mathbf{P} - q\mathbf{E} - \frac{1}{c}\mathbf{J} \times \mathbf{B} = 0, \\
&\frac{\partial}{\partial t}\left(\xi + \frac{E^2 + B^2}{8\pi}\right) + \nabla \cdot \left[(\xi + P)\,\mathbf{v} + \mathbf{v} \cdot \mathbf{\Pi} + \mathbf{q} + \mathbf{S}\right] = 0,
\end{aligned} \tag{2.30}$$

where

$$\xi = \frac{1}{2}\rho v^2 + \frac{3}{2}P, \tag{2.31}$$

$\mathbf{q}$ is the vector of thermal flux, and $\mathbf{S} = (\mathbf{E} \times \mathbf{B})/4\pi$ is the Poynting vector. $\mathbf{\Pi}$ and P are parts of the pressure tensor $\mathbf{P} = P\mathbb{1} + \mathbf{\Pi}$, that is indeed divided into its viscous stress tensor ($\mathbf{\Pi}$), related to viscous forces, and its scalar pressure (P), where $\mathbb{1}$ is the unit tensor. These equations must necessarily be coupled with Maxwell's equations (2.20). The obtained system is composed of 12 equations with 21 unknowns, that become 15 for $\mathbf{q} = 0$ and $\mathbf{\Pi} = 0$. In this case, the plasma is *collisional*, i.e., is in local thermal equilibrium (LTE). Therefore, three more equations are needed to solve the system. These are given by the *generalized Ohm's law* in the case of a fully ionized plasma ($n_e \simeq n_p$) and with $m_e \ll m_p$, namely

$$\mathbf{E} + \frac{1}{c}(\mathbf{v} \times \mathbf{B}) - \frac{\mathbf{J}}{\sigma} = \frac{m_e}{n_e e^2}\left[\frac{\partial \mathbf{J}}{\partial t} + \nabla \cdot (\mathbf{J}\mathbf{v} + \mathbf{v}\mathbf{J})\right] + \frac{\mathbf{J} \times \mathbf{B}}{n_e e c} - \frac{\nabla \mathbf{P}_e}{e n_e}. \tag{2.32}$$

Therefore, there is an effect due to conductivity, that is the dissipation due to the Joule effect, which transforms magnetic energy into thermal energy. In Equation (2.32), $\mathbf{J}$ is defined as a function of macroscopic quantities. The state of the plasma under pressure P in the ideal case (i.e., non-viscous) is described by the equation of state

$$\rho e = \frac{P}{\Gamma - 1}, \tag{2.33}$$

where ρe represents the internal energy and $\Gamma = (d_f + 2)/d_f$ is related to the degrees of freedom d_f. The system is now closed with the same number of equations and unknowns.

2.4 The magnetohydrodynamic model

The magnetohydrodynamic (MHD) model applies to large scales and low frequencies ($\omega \ll \omega_p, \omega_c, \nu_c$) and it constitutes the simplest phenomenological model of a plasma described as a perfectly conducting fluid. As such, it completely ignores kinetic effects, finite-Larmor-radius effects, and wave-particle interaction. Nevertheless, the MHD description provides the simplest and most viable first approximation to much of the physics, even when some of the conditions are not met. In that sense, it allows drawing intuitive conclusions concerning plasma behavior without solving the equations in detail.
The continuity, momentum, induction, and energy conservation laws in the MHD model are, respectively,

$$\begin{aligned}
&\frac{\partial \rho}{\partial t} + \nabla \cdot (\rho \mathbf{v}) = 0, \\
&\frac{\partial \mathbf{m}}{\partial t} + \nabla \cdot \left[\mathbf{m}\mathbf{v} - \mathbf{B}\mathbf{B} + \mathbb{1} \left(P + \frac{\mathbf{B}^2}{2} \right) \right] = 0, \\
&\frac{\partial \mathbf{B}}{\partial t} + \nabla \times (c\mathbf{E}) = 0, \\
&\frac{\partial E_t}{\partial t} + \nabla \cdot \left[\left(\frac{\rho \mathbf{v}^2}{2} + \rho e + P \right) \mathbf{v} + c\mathbf{E} \times \mathbf{B} \right] = 0,
\end{aligned} \tag{2.34}$$

where $\mathbf{m} = \rho \mathbf{v}$ is the momentum density, and E_t is the total energy density, defined as

$$E_t = \rho e + \frac{\mathbf{m}^2}{2\rho} + \frac{\mathbf{B}^2}{2}, \tag{2.35}$$

being $\rho e = P/(\Gamma - 1)$ in the case of an ideal gas, with $\Gamma = 4/3$. In the MHD case, the pressure tensor is diagonal ($P \neq 0$, $\mathbf{\Pi} = 0$), as it is applied to large scales and low frequencies, therefore the collisional equilibrium is reached ($\tau \gg \tau_p, \tau_c, \tau_\nu$). The evolution of the magnetic field $\mathbf{B}$ is prescribed by Faraday's law, and a constant term $\sqrt{4\pi}$ is included in its definition. Moreover, Faraday's law is accompanied by the solenoidal condition

$$\nabla \cdot \mathbf{B} = 0. \tag{2.36}$$

The definition of the electric field $\mathbf{E}$ comes from the *generalized Ohm's law* in Equation (2.32), in which the right-hand side is null as it is composed of terms corresponding to high-frequencies. Therefore, the electric field is given by

$$c\mathbf{E} = -\mathbf{v} \times \mathbf{B} + \frac{\eta}{c}\mathbf{J}, \tag{2.37}$$

where $\eta = c^2/\sigma$ represents the resistivity, with σ being the conductivity defined in Section 2.1. The current density is defined as

$$\mathbf{J} = c\nabla \times \mathbf{B}. \tag{2.38}$$

As seen in Equation (2.34), the continuity charge equation is missing, as in the MHD case it becomes

$$\nabla \cdot \mathbf{J} = 0, \tag{2.39}$$

in agreement with Equation (2.38). In Equation (2.37), $\mathbf{v} \times \mathbf{B}$ represents the convective term ($\mathbf{E}_c$), while $(\eta\mathbf{J})/c$ is the resistive one ($\mathbf{E}_r$). These two terms are related to two different time scales, which can be identified in the *induction equation*

$$\frac{\partial \mathbf{B}}{\partial t} = \nabla \times (\mathbf{v} \times \mathbf{B}) + \eta \nabla^2 \mathbf{B}, \tag{2.40}$$

obtained by first applying the curl operator to Equation (2.37) and then substituting Equation (2.38). The first term of Equation (2.40) is the convective one, which expresses the fact that the magnetic field is affected by the motion of the plasma, while the second one is the resistive one, which diffuses the magnetic field. These events are linked to two time scales: the convective ($\tau_c = L/v_g$) and diffusive ($\tau_d = L^2/\eta$) scale, where L represents the characteristic length scale of the system. The ratio between

these scales leads to the magnetic *Reynolds number* $R_m = \tau_d/\tau_c = v_g L/\eta$ or to the *Lundquist number*

$$S = \frac{v_A L}{\eta}, \tag{2.41}$$

where v_A is the *Alfvén velocity* defined in Section 2.1. Three regimes are possible:

- $R_m, S \gg 1$: ideal regime ($\eta = 0$),
- $R_m, S \sim 1$: non-ideal regime ($\eta \neq 0$),
- $R_m, S \ll 1$: resistive regime ($\eta \neq 0$).

In the ideal regime ($\eta = 0$), *Alfvén theorem* holds. It stands that

$$\frac{d\Phi(\mathbf{B})}{dt} = 0, \tag{2.42}$$

i.e., that magnetic flux through any closed line that moves along with the fluid does not change over time. Therefore, the fluid acts on the magnetic field, but the field acts on the fluid in turn. The dynamic that dominates the other is established by the β-parameter described in Section 2.1. *Alfvén theorem* obviously does not hold in the resistive case ($\eta \neq 0$), as the magnetic field can change its topology. In fact, in the limit case $\eta \to \infty$ the fluid and the magnetic field are decoupled.

2.4.1 Sweet-Parker model

As claimed in the introduction (see Section 1), in the resistive case, magnetic field topology may break due to the formation of localized and strong current sheets that favor magnetic reconnection events. Sweet (1958) and Parker (1957) argued that magnetic reconnection takes place in current sheets and discussed the model shown in Figure 2.1.
Consider a region of length $2L$ and height $2l$ containing a non-ideal plasma ($\eta \neq 0$), with a practically zero magnetic field. Outside this region, there is an ideal plasma or a plasma in which the convective effects dominate over the resistive ones ($\eta \simeq 0$). In this outer region, the magnetic field B_i is frozen in the plasma, due to the Alfvén theorem, and is transported to the diffusive region with plasma velocity v_i. There is a stationary condition, which occurs when two velocities are equal. The velocities are v_i and the speed with which the magnetic field manages to spread in the resistive

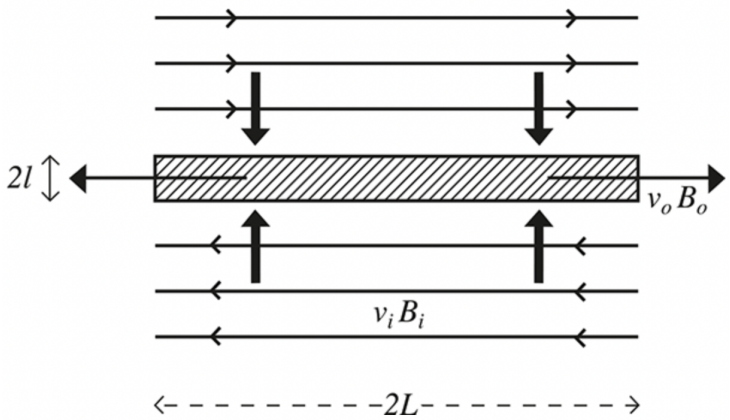

Figure 2.1: A sketch of the the Sweet–Parker model for magnetic reconnection at a current sheet. Credit: Priest (2020).

region until it is canceled with that coming from the opposite direction. Outside the region, the electric field only has its convective term

$$E \sim \frac{v_i B_i}{c}, \tag{2.43}$$

while inside only the resistive processes occur

$$E \sim \frac{J}{\sigma}. \tag{2.44}$$

At the boundary, the two terms must be equal. In fact, since a tangent field has no discontinuity, the tangent components are continuous at the interface. J could be obtained through a numerical analysis from Equation (2.38)

$$J \sim \frac{cB}{l}. \tag{2.45}$$

By equaling the electric fields and replacing this value of J, the initial speed of the fluid

$$v_i = \frac{\eta}{l} \tag{2.46}$$

is obtained. The stationary equation of motion must also be considered, with equal pressure everywhere ($\nabla P \sim 0$), namely

$$\rho \frac{v_o^2}{L} = \frac{B_i B_0}{l} \rightarrow v_o^2 = \frac{B_i^2}{\rho} = v_{\mathrm{A,i}}^2. \tag{2.47}$$

This means that the fluid exits the region with the Alfvén speed at the entrance.

The efficiency of the process is given by the reconnection rate

$$R_{\rm rec} = \frac{v_i}{v_o} = \sqrt{\frac{\eta}{L v_o}} = S^{-1/2}. \tag{2.48}$$

However, as claimed in the introductory section, this rate is too slow to account for astrophysical phenomena.

2.4.2 Fast magnetic reconnection

Magnetic reconnection can be triggered by the tearing instability, which can lead to fast magnetic reconnection (see, e.g., Giannios, 2013; Del Zanna et al., 2016), that is responsible for the fragmentation of very thin current sheets into a large number of plasmoids.
Del Zanna et al. (2016) studied the tearing mode instability in relativistic plasmas through a linear analysis of the growth of the perturbations of an initial current sheet in equilibrium. It is convenient to normalize all quantities against the length-scale a (i.e., the half width of the sheet), the corresponding Alfvénic crossing time $\bar{\tau}_A = a/v_A$, and the equilibrium magnetic field strength B_0. In this way, the maximum growth rate for the fastest growing mode is

$$\bar{\gamma}_{\rm max} \equiv \gamma_{\rm max} \bar{\tau}_A \simeq 0.6\ \bar{S}^{-1/2}, \tag{2.49}$$

with corresponding maximum wavenumber

$$\bar{k}_{\rm max} \equiv k_{\rm max} a \simeq 1.4\ \bar{S}^{-1/4}, \tag{2.50}$$

where $\bar{S}$ is the Lundquist number relative to the length-scale a, namely

$$\bar{S} = \frac{a v_A}{\eta}. \tag{2.51}$$

To analyze the relativistic ideal tearing instability in thin current sheets, it is convenient to measure both the time and the Lundquist number in terms of a macroscopic length-scale L, namely the length of a thin current sheet (with aspect ratio $L/a \gg 1$). The time thence becomes

$$\tau_A = \frac{L}{v_A}, \tag{2.52}$$

while the Lundquist number is given by Equation (2.41), so that

$$\bar{\tau}_A = \frac{a}{L}\tau_A \ll \tau_A, \quad \bar{S} = \frac{a}{L} S \ll S. \tag{2.53}$$

Therefore, the growth rates are expected to increase, when normalized to these macroscopic quantities.
The result for thin current sheets is

$$\gamma_{\max}\tau_A \simeq 0.6\ S^{-1/2}\left(\frac{a}{L}\right)^{-3/2}. \tag{2.54}$$

This result in Sweet-Parker sheets with $a/L \sim S^{-1/2}$ leads to the paradoxical result of a rate growing with a positive power of S. However, the ideal plasma limit should be recovered for $S \to \infty$. It is convenient to parametrize in terms of S the inverse aspect ratio as $a/L \sim S^{-\alpha}$ (see Pucci and Velli, 2014). In this way, the tearing growth time becomes ideal when $\alpha = 1/3$. This occurs as the dependence on S completely disappears when $a = LS^{-1/3}$. Thence the Equation (2.49) and (2.50) become

$$\gamma_{\max}\tau_A \simeq 0.6, \quad k_{\max}L \simeq 1.4\ S^{1/6}, \tag{2.55}$$

using the normalization in Equation (2.53). The instability now occurs on the Alfvénic time τ_A, as measured on the macroscopic scales.
Pucci and Velli (2014) and Landi et al. (2015) concluded that in a dynamical process with decreasing a/L values, the Sweet-Parker configuration with $\alpha = 1/2 > 1/3$ is never reached. Therefore, a thin current sheet that enters the ideal tearing mode ($a/L \sim S^{-1/3}$), is subjected to fast magnetic dissipation. Indeed, the modes growth is fast and asymptotically independent of S (provided $S \sim 10^6$).

2.4.3 A note on resistivity

The origin of physical resistivity η in plasmas is still a subject of active debate. Astrophysical plasmas are supposed to be *collisionless*, as Coulomb collisions between particles composing the plasma are generally tremendously rare. Therefore, plasma resistivity cannot originate from collisions between particles. One way out is *anomalous resistivity*.
Such anomalous resistivity is generated by the scattering of particles by electromagnetic waves (i.e., wave-particle interactions). This scattering can introduce effective collisions that lower the conductivity of the plasma (Graham et al., 2022).
As claimed by Che (2017), anomalous resistivity may also lead to a faster Sweet-Parker regime that could explain observations (see also Ji et al., 1998; Kulsrud, 2001).

Indeed, Ma et al. (2018) argue that the fast magnetic reconnection regime is often linked to anomalous resistivity that could arise in the small electron magnetic reconnection diffusion region due to local current-instability-driven turbulence (see also Malyshkin et al., 2005; Eyink et al., 2013).
Although this thesis work follows the Sweet-Parker assumption of a constant physical resistivity, a more realistic resistivity should depend on time, space, and plasma parameters (Ripperda et al., 2019a).
Anomalous resistivity is indeed included in several MHD simulations of astrophysical plasmas (see, e.g., Schumacher and Kliem, 1997; Ohsuga et al., 2009).

2.5 Particle equations

MHD describes the thermal component of plasmas. However, a plasma consists also of a non-thermal component represented by charged particles, or cosmic rays (CR; Mignone et al., 2018). Therefore, we need to introduce particles to model also this non-thermal component.
Particles are defined in terms of their spatial coordinates $\mathbf{x}_p$ and velocity $\mathbf{v}_p$, which are governed by the equations of motion

$$\begin{cases} \dfrac{d\mathbf{x}_p}{dt} = \mathbf{v}_p, \\ \dfrac{d(\gamma\mathbf{v})_p}{dt} = \left(\dfrac{e}{mc}\right)_p (c\mathbf{E} + \mathbf{v}_p \times \mathbf{B}), \end{cases} \tag{2.56}$$

where the suffix p is used to label a single particle. $(e/mc)_p$ is the particle charge to mass ratio and its Lorentz γ-factor is given by $\gamma = 1/\sqrt{1 - v_p^2/\mathbb{C}^2}$, where $\mathbb{C}$ is the speed of light artificial value, as in the MHD equations the actual speed of light does not explicitly appear. In this thesis work $\mathbb{C}$ is set to $10^4\ v_A$ since, for consistency reasons, it must be larger than any characteristic signal velocity.
As seen in Equation (2.37), the electric field $\mathbf{E}$ is composed of a convective ($\mathbf{E}_c$) and a resistive ($\mathbf{E}_r$) contribution. In addition to triggering tearing-driven magnetic reconnection, the resistive term is thought to be of crucial importance in the process of particle acceleration (Li et al., 2017). In fact, while in ideal MHD ($\eta = 0$) no electric field is present in the fluid rest frame, a resistive plasma is still capable of accelerating particles at stagnation points, provided a large current is formed. In reconnecting

current sheet this condition is manifestly evident at X-points, where the condition $|\mathbf{E}| > |\mathbf{B}|$ can easily occur.

3
Numerical methods

This chapter discusses the various numerical methods used to approach the study of particle acceleration in astrophysical plasmas. In this thesis work, the used numerical approach is implemented in the PLUTO code for astrophysical gas dynamics. How the PLUTO code works and the implemented numerical setup are discussed in this chapter.

3.1 MHD vs PIC codes

Plasma simulations are carried out through different numerical approaches, which apply to different scales. The models at the scale extremes are the *particle-in-cell* (PIC; see, e.g., Zenitani and Hoshino, 2001; Oka et al., 2010; Sironi and Spitkovsky, 2014; Guo et al., 2015; Werner et al., 2016) and the *magnetohydrodynamic* (MHD; see, e.g., Onofri et al., 2006; Kowal et al., 2011, 2012; Ripperda et al., 2017a,b) one.
PIC codes work on high frequencies (i.e, $\omega \gg \omega_p, \omega_c, \nu_c$) and therefore provide the most self-consistent approach to model plasma dynamics at small scales. However, these codes must resolve the electron skin depth (see Section 2.1), which, in most cases, is several orders of magnitude smaller than the overall size of a typical astrophysical system. Even with the most powerful supercomputers, PIC simulations become prohibitively expensive for describing astrophysical systems at larger scales.
Fluid models such as the MHD one have been extensively used to investigate, instead, the large-scale dynamics of high-energy astrophysical environments. Because of its nature, however, the fluid approach is applicable on scales much larger than the *Larmor radius* (see Section 2.1), and so on low frequencies. As a consequence, this model is not able to capture important kinetic effects relevant to the microscale.
Therefore, MHD and PIC models apply to too distant spatial and temporal scales. In fact, the large-scale dynamics of the analyzed astrophysical

systems described in the Introduction (see Section 1) are observed at about 1 pc (i.e., 10^{18} cm), while the particle dynamics occur at about 10^4 cm. There are about ten orders of magnitude of difference, and so it is impossible to balance macroscopic effects that trigger the dissipation and the microscopic effects that generate the spectrum. For this reason, the current understanding of astrophysical systems is limited by the range of scales beyond which one or more model assumptions break down or when computational resources become prohibitive.

3.2 Fluid-particle hybrid approach

When the forces exerted on the fluid by particles are negligible (i.e, no feedback on the fluid is present), the limits previously described can be overcome by using a hybrid MHD-PIC model (see, e.g., Bai et al., 2015; Mignone et al., 2018). This hybrid model allows approaching the fluid with the MHD model, while particles are treated kinetically using conventional PIC techniques. This formalism aims to capture the kinetic effects of particles without the need to resolve the plasma skin depth, as is typically required by PIC codes. In the MHD-PIC formalism, only the *Larmor* scale must be properly resolved instead. This extends the range of applicability to much larger spatial and temporal scales when compared to the standard PIC approach, inasmuch as the particle gyroradius largely exceeds the plasma skin depth.
In this thesis work, we used an MHD-PIC approach without feedback on the fluid. In this case, we refer to particles as test-particles. The resistive MHD model coupled with a test-particle approach is already implemented in the PLUTO code.

3.3 The PLUTO code

PLUTO is a multi-dimensional finite-volume code for astrophysical fluid dynamics (see Mignone et al., 2007, 2012a) providing a modular infrastructure whereby distinct physics modules and different algorithms may be independently combined together in order to meet up the user's most appropriate requirements. This code, entirely written in the C programming language, was developed at the Physics Department of the University of Turin and can run on either single or parallel machines. Being a Godunov-

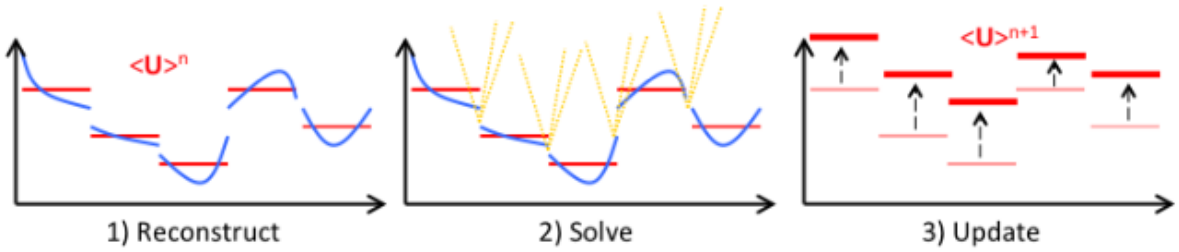

Figure 3.1: The Reconstruct-Solve-Update step sequence typical of a Godunov-type code: 1) the solution is first reconstructed inside a computational zone, 2) a Riemann solver is used to compute the intercell flux, and 3) the solution is updated to the next time level. Credit: A. Mignone.

type code (see Godunov, 1959), PLUTO's flowchart follows a three-step sequence, summarized in Figure 3.1:

1. *Reconstruct*: a piecewise polynomial reconstruction inside each cell.
2. *Solve*: compute the interface flux by solving the Riemann problems between adjacent discontinuous states obtained at zone interfaces during the reconstruction step.
3. *Update*: update the solution array of conserved variables to the next time level.

Finite volume schemes have a long-standing tradition for their ability to capture shocks and discontinuities in general without the need to introduce artificial dissipation. They rely on the conservative form of the equations

$$\frac{\partial \mathcal{U}}{\partial t} + \nabla \cdot \mathrm{F}(\mathcal{U}) = 0, \tag{3.1}$$

which stems from physical principles stating conservation of fundamental quantities such as mass, momentum, and energy. Equation (3.1) represents a system of partial differential equations in which $\mathcal{U}$ is an array of conserved quantities (i.e., density, momentum, and energy), while F is the flux tensor. Equation (3.1) simplifies to

$$\frac{\partial \mathcal{U}}{\partial t} + \frac{\partial \mathrm{F}}{\partial x} = 0 \tag{3.2}$$

if one-dimensional Cartesian coordinates are considered. The computational domain is defined by $x \in [x_b, x_e]$, which is discretized into N_x cells (or zones) of equal length Δx centered around their position center x_i. Cell interfaces are located at $x_{i\pm\frac{1}{2}} = x_i \pm \Delta x/2$. To simplify the notation, in what follows we omit the integer-valued subscripts when referring to the array of conserved quantities $\mathcal{U}$ and the flux tensor F.

3.3.1 Reconstruction step

A high-order non-oscillatory polynomial $\mathcal{P}$ is used to reconstruct interface values from zone averages

$$\begin{cases} \mathcal{V}_{+,L} = \lim\limits_{\mathbf{x}\to\mathbf{x}_+} \mathcal{P}(\mathbf{x}), \\ \mathcal{V}_{-,R} = \lim\limits_{\mathbf{x}\to\mathbf{x}_-} \mathcal{P}(\mathbf{x}). \end{cases} \tag{3.3}$$

where $s = L$ ($s = R$) at $\mathbf{x} = \mathbf{x}_+$ ($\mathbf{x} = \mathbf{x}_-$). Indeed, the subscripts R and L refer to the sides of the interface. Fluxes are more conveniently computed using a different set of physical quantities, that are the primitive coordinates $\mathcal{V}$.
Several reconstruction schemes are available in the PLUTO code, but in this thesis work two of them have been considered, namely

- a 2^{nd}-order piecewise linear reconstruction,
- the 5^{th}-order WENO-Z algorithm (see, e.g., Borges et al., 2008; Mignone et al., 2010).

A 2^{nd}-order linear interpolant is characterized by

$$\mathcal{V}_{\pm,s} = \mathcal{V} \pm \frac{\Delta\tilde{\mathcal{V}}}{2}, \tag{3.4}$$

where $\Delta\tilde{\mathcal{V}}$ are the slopes computed using a limiting procedure that can be applied to primitive or characteristic variables. Different steepening properties characterize different slope limiters, that can be independently assigned to each characteristic field or primitive variable (Mignone et al., 2007).
The WENO-Z scheme presented by Borges et al. (2008) is less dissipative at discontinuities and increases the resolution at critical points as compared to the classical 5^{th}-order weighted WENO scheme by Jiang and Shu (1996). Nevertheless, this scheme does not require a much higher computational cost. WENO-Z reconstructs interface values through the convex combination of several third-order accurate interface values built on the three possible sub-stencils of $i-2 \le s \le i+2$, namely

$$\begin{aligned} \mathcal{I}(f_{[\mathrm{s}]}) = \omega_0 \frac{2f_{\mathrm{i}-2} - 7f_{\mathrm{i}-1} + 11f_i}{6} + \omega_1 \frac{-f_{\mathrm{i}-1} + 5f_i + 2f_{\mathrm{i}+1}}{6} + \\ + \omega_2 \frac{2f_i + 5f_{\mathrm{i}+1} - f_{\mathrm{i}+2}}{6}, \end{aligned} \tag{3.5}$$

where either one of the positive and negative part of the flux is shorten with $f_{[\mathrm{s}]}$, while ω_l $(l = 0, 1, 2)$ represents the weights, defined as

$$\omega_l = \frac{\alpha_l}{\sum_m \alpha_m}, \quad \alpha_l = d_l \left(1 + \frac{|\beta_0 - \beta_2|}{\beta_l + \zeta}\right), \tag{3.6}$$

where $d_0 = 1/10$, $d_1 = 3/5$, $d_2 = 3/10$ are the optimal weights that give a 5^{th}-order accurate approximation, $\zeta = 10^{-40}$ is a small number that avoids division by zero, and β_l are smoothness indicators that give a measure of the regularity of the corresponding polynomial approximation, namely

$$\begin{aligned}
\beta_0 &= \frac{13}{12}\left(\Delta_{i-\frac{1}{2}} - \Delta_{i-\frac{3}{2}}\right)^2 + \frac{1}{4}\left(3\Delta_{i-\frac{1}{2}} - \Delta_{i-\frac{3}{2}}\right)^2, \\
\beta_1 &= \frac{13}{12}\left(\Delta_{i+\frac{1}{2}} - \Delta_{i-\frac{1}{2}}\right)^2 + \frac{1}{4}\left(\Delta_{i+\frac{1}{2}} + \Delta_{i+\frac{1}{2}}\right)^2, \\
\beta_2 &= \frac{13}{12}\left(\Delta_{i+\frac{3}{2}} - \Delta_{i+\frac{1}{2}}\right)^2 + \frac{1}{4}\left(3\Delta_{i+\frac{1}{2}} - \Delta_{i+\frac{3}{2}}\right)^2,
\end{aligned} \tag{3.7}$$

where $\Delta_{i+1/2} = f_{i+1} - f_i$. The analysis of the WENO-Z scheme implementation in the PLUTO code is based on Mignone et al. (2010).

3.3.2 Riemann solvers

The computation of the fluxes at cell interfaces requires knowledge of the solution between t^n and t^{n+1}. In shock-capturing schemes, this is achieved by determining the solution of the *Riemann problem*, i.e., the evolution of a discontinuity separating two constant states initially adjacent to a zone interface

$$\mathcal{U}(x, t^n) = \begin{cases} \mathcal{U}_{+,\mathrm{L}} & \text{for } x < x_+, \\ \mathcal{U}_{+,\mathrm{R}} & \text{for } x > x_+. \end{cases} \tag{3.8}$$

The discontinuity will break into a number of waves whose number and properties depend on the actual system of conservation laws being solved. A *Riemann solver* naturally embeds the concept of *upwinding*, i.e., the discretization stencil should be biased towards the direction from which characteristic waves propagate.

For complex systems of conservation laws, the solution of the *Riemann problem* requires the simultaneous solution of a set of nonlinear systems of equations. In non-relativistic and relativistic MHD (RMHD), for instance, the decay of the initial discontinuity gives rise to a self-similar wave pattern in the $x - t$ plane, where seven wave modes can develop (see Figure

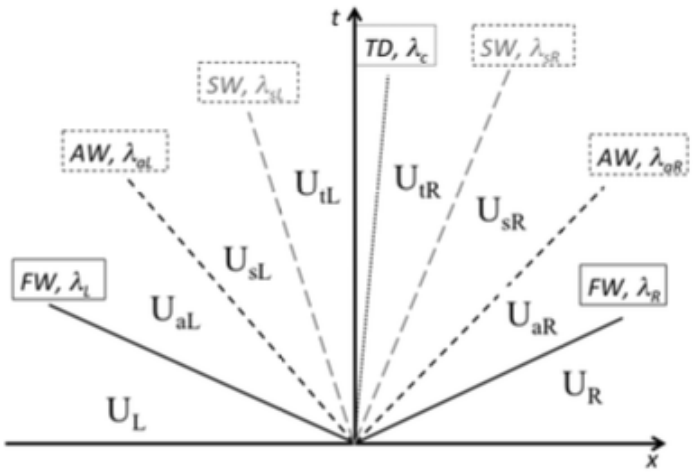

Figure 3.2: General structure of the Riemann fan generated by two initial constant states: $\mathcal{U}_L$ and $\mathcal{U}_R$. The pattern includes 7 waves corresponding to a pair of fast magnetosonic waves, a pair of rotational Alfvén waves, a pair of slow magnetosonic modes, and a contact (or tangential) discontinuity in the middle, propagating at the fluid speed. The seven waves bound six intermediate constant states. Credit: A. Mignone.

3.2). *Fast waves* (FW) are the outermost ones and enclose a pair of *Alfvén waves* (AW), a pair of *slow waves* (SW) bounding a *tangential discontinuity* (TD) in the middle. FW and SW can be either *shock* or *rarefaction waves* where primary flow quantities (density, pressure, velocity, and magnetic field) change discontinuously (for the former) or smoothly (for the latter), depending on the magnetic field topology and pressure jump. Across the AW, thermodynamic quantities remain continuous while the tangential components of magnetic field trace circles, in classical MHD, or ellipses, in the RMHD case (Mignone et al., 2012b). Finally, through the *contact mode*, only density exhibits a jump while thermal pressure, velocity, and magnetic field remain continuous.
Across each wave, the *Rankine-Hugoniot jump conditions* must be satisfied

$$\lambda^{(k)} \left(\mathcal{U}_L^{(k)} - \mathcal{U}_R^{(k)} \right) = \mathrm{F}(\mathcal{U}_L^{(k)}) - \mathrm{F}(\mathcal{U}_R^{(k)}), \tag{3.9}$$

where $k = 1, ..., 7$ lists the waves. An exact solver demands the simultaneous solution of the *Rankine-Hugoniot jump conditions* across each wave through a self-consistent procedure that resolves FW, SW, and AW to the left and the right of the contact (or tangential in the degenerate case) discontinuity, that is always located at the center of the structure. This task is computationally expensive in classical MHD and almost impracticable in the RMHD case (see Giacomazzo and Rezzolla, 2006). For this reason,

approximate methods of solution are usually preferred. The degree of approximation reflects the ability to capture and spread discontinuities over a few or more computational zones and it is ultimately responsible for the amount of numerical dissipation of the numerical scheme (Mignone, 2017). The impact of the numerical diffusion developed by the various schemes on the simulation results is one of the crucial aspects of this thesis work, for which the considered *Riemann solvers* in the MHD case are

- the Roe Riemann solver (see Cargo and Gallice, 1997),
- the HLL Riemann solver (see Harten et al., 1983),
- the HLLD Riemann solver of Miyoshi and Kusano (2005).

The Roe Riemann solver provides intercell fluxes generally written as

$$\hat{\mathrm{F}} = \mathrm{F} - \phi, \tag{3.10}$$

where $\mathrm{F} = (\mathrm{F}_L + \mathrm{F}_R)/2$, while ϕ represents the dissipative term, namely

$$\phi = \frac{1}{2}\mathrm{R}|\Lambda|\mathrm{L}\cdot(\mathcal{U}_R - \mathcal{U}_L), \tag{3.11}$$

where $\mathrm{F}_{L,R}$ are the left and right fluxes, L and R are the left and right eigenvector matrices defined in terms of the Roe average state, while $|\Lambda| = \mathrm{diag}(|\lambda_1|, ..., |\lambda_k|)$ represents the diagonal matrix containing the absolute value of eigenvalues.

In the HLL case, the intercell numerical flux is given by

$$\hat{\mathrm{F}} = \frac{\alpha_R \mathrm{F}_L + \alpha_L \mathrm{F}_R}{\alpha_R + \alpha_L} - \frac{\alpha_R \alpha_L (\mathcal{U}_R - \mathcal{U}_L)}{\alpha_R + \alpha_L}, \tag{3.12}$$

where $\alpha_R = \max(0, \lambda_R) \geq 0$ and $\alpha_L = -\min(0, \lambda_L) \geq 0$, with λ_R and λ_L the rightmost and leftmost characteristic speed. These two solvers are ordinarily employed in numerical simulations of MHD flows and differ in the amount of numerical diffusion (the HLL being more diffusive than the Roe one).

The HLLD Riemann solver approximates the Riemann fan with a five-wave pattern composed of two outermost fast shocks with speed λ_L and λ_R, two rotational waves propagating with speeds

$$\lambda^{*L} = \lambda^* - \frac{|B_x|}{\sqrt{\rho^{*L}}}, \quad \lambda^{*R} = \lambda^* + \frac{|B_x|}{\sqrt{\rho^{*R}}}, \tag{3.13}$$

where $\rho^{*s} = \rho^s(\lambda^s - v^s)/(\lambda^s - \lambda^*)$ with $s = L$ or R and $\lambda^* = m^{\mathrm{hll}}/\rho^{\mathrm{hll}}$ (where "hll" marks a component of the HLL intermediate state), separated, in the

adiabatic case, by a contact wave in the middle propagating with speed λ^*. The HLLD flux is written as

$$\begin{aligned}\hat{\mathrm{F}} = \frac{1}{2}[\mathrm{F}^L + \mathrm{F}^R - |\lambda_L|(B_t^{*L} - B_t^L) - |\lambda^{*L}|(B_t^{**} - B_t^{*L}) - \\ - |\lambda^{*R}|(B_t^{*R} - B_t^{**}) - |\lambda_R|(B_t^R - B_t^{*R})],\end{aligned} \tag{3.14}$$

where $t = y, z$, $\mathrm{F} = v_x B_t - v_t B_x$, while

$$B_t^{**R} = B_t^{**L} = B_t^{**} = \frac{\lambda^{*R} B_t^{*R} - \lambda^{*L} B_t^{*L} + \mathrm{F}^{*L} - \mathrm{F}^{*R}}{\lambda^{*R} - \lambda^{*L}}, \tag{3.15}$$

where $\mathrm{F}^{*s} = \mathrm{F}^s + \lambda^s(B_t^{*s} - B_t^s)$, with B_t^{*s} given by $B_t^{*s} - B_t^s = B_t^s \chi^s$, where

$$\chi^s = \frac{(v_x^s - \lambda^*)(\lambda^s - \lambda^*)}{(\lambda^{*s} - \lambda^s)(\lambda^{*s} + \lambda^s - 2\lambda^*)}. \tag{3.16}$$

The HLLD solver presents excellent stability properties and reduced numerical dissipation when applied to time-dependent magnetized current sheets (see Section 3.3.6 for further details). The Riemann solver description is based on Mignone and Del Zanna (2021).

3.3.3 Final Update step

The Equation

$$\mathcal{U}^{n+1} = \mathcal{U}^n + \Delta t \mathcal{L}^n, \tag{3.17}$$

is obtained in the simplest case of forward Euler discretization, where $\Delta t = t^{n+1} - t^n$ is the time interval, while $\mathcal{L}^n$ is the flux difference operator, namely

$$\mathcal{L}^n = \sum_d \mathcal{L}^d = -\frac{1}{\Delta V}(A_+^d \mathrm{F}_+^d - A_-^d \mathrm{F}_-^d), \tag{3.18}$$

where $d = 1, 2, 3$ is a given direction and $A_\pm^d$ and ΔV are the cell's right (+) and left (-) interface areas and cell volume in that direction, respectively. $\mathrm{F}_\pm$ are the numerical flux functions following the solution of one-dimensional Riemann problems at cell interfaces. When $d = 1, 2$, and 3, $\pm \equiv (i \pm 1/2, j, k)$, $(i, j \pm 1/2, k)$, and $(i, j, k \pm 1/2)$, respectively (see Mignone et al., 2007).

Equation (3.17) is an exact expression relating the change of zone-averaged conserved quantities inside a cell to the net time-averaged flux through its cell boundaries (see Figure 3.3). Therefore, in this step, the solution array of conserved variables is updated to the next time level using Equation (3.17) or a higher order discretization method. This formulation is essential to ensure conservation from a computational perspective (Mignone, 2017).

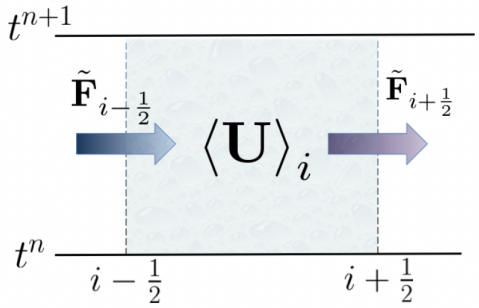

Figure 3.3: Schematic diagram of a finite-volume conservative scheme: the variation of the average value of $\mathcal{U}$ inside a computational cell is related to the net flux F through its boundary. Credit: A. Mignone.

3.3.4 A note on numerical diffusion

Let us consider the equation

$$\frac{\partial \mathcal{U}}{\partial t} + w\frac{\partial \mathcal{U}}{\partial x} = 0, \tag{3.19}$$

which has known analytical solution consisting of a uniform translation of the initial profile, that is $\mathcal{U}(x,t) = \mathcal{U}(x - wt, 0)$. $w > 0$ leads to the so-called *"forward in time, backward in space"* (FTBS) scheme.

The amount of numerical diffusion introduced by the FTBS scheme can be quantified by computing the local truncation error introduced in the discretization equation. Expanding around $\mathcal{U}^n$ and keeping terms up to 2^{nd}-order, the Equation

$$\frac{\partial \mathcal{U}}{\partial t} + w\frac{\partial \mathcal{U}}{\partial x} = \frac{w\Delta x}{2}\left(1 - w\frac{\Delta t}{\Delta x}\right)\frac{\partial^2 \mathcal{U}}{\partial x^2} + \mathrm{O}(\Delta t^2) + \mathrm{O}(\Delta x^2) \tag{3.20}$$

is obtained. Therefore, the grid values $\mathcal{U}^n$ obtained with the FTBS scheme provide a 1^{st}-order approximation to the true solution of the original scalar Equation (3.19) but satisfy exactly a modified partial differential Equation given by (3.20) (see LeVeque, 2002). If the 2^{nd}-order terms are neglected, the grid values $\mathcal{U}^n$ are 2^{nd}-order approximation to the actual solution. For higher order schemes the 1^{st} term on the right-hand side of Equation (3.20) can be eliminated and the amount of dissipation is progressively reduced. In the fluid ideal case ($\eta = 0$) the only present dissipation is the numerical one.

3.3.5 Time-stepping schemes

The three-step sequence of steps shown in Figure 3.1 may be iterated more than once in the case of a multi-stage *Runge-Kutta scheme*. A robust 2^{nd}-order time stepping method (RK2) is the following predictor-corrector scheme

$$\begin{aligned} \mathcal{U}^* &= \mathcal{U}^n + \Delta t \mathcal{L}^n, \\ \mathcal{U}^{n+1} &= \frac{1}{2}(\mathcal{U}^n + \mathcal{U}^* + \Delta t \mathcal{L}^*). \end{aligned} \tag{3.21}$$

By adding an additional step, the 3^{rd}-order Runge-Kutta method (RK3) of Gottlieb and Shu (1998) is obtained, namely

$$\begin{aligned} \mathcal{U}^* &= \mathcal{U}^n + \Delta t \mathcal{L}^n, \\ \mathcal{U}^{**} &= \frac{1}{4}(3\mathcal{U}^n + \mathcal{U}^* + \Delta t \mathcal{L}^*), \\ \mathcal{U}^{n+1} &= \frac{1}{3}(\mathcal{U}^n + 2\mathcal{U}^{**} + 2\Delta t \mathcal{L}^{**}). \end{aligned} \tag{3.22}$$

For these methods, the input states for the Riemann solver are given by the output of the interpolation routine (see Section 3.3.1). The RK2 and RK3 marching schemes have to solve a total of two and three Riemann problems per cell per direction, respectively. Moreover, boundary conditions must be assigned before each step (Mignone et al., 2007). The time step Δt is limited by the Courant–Friedrichs–Lewy (CFL; see Courant et al., 1928) condition, namely

$$\Delta t = C_a \min_d \left(\frac{\Delta l^d_{\min}}{|\lambda^d_{\max}|} \right), \tag{3.23}$$

with $\lambda^d_{\max}$ and $\Delta l^d_{\min}$ representing the largest signal velocity and the smallest cell length in the d direction, respectively. C_a represents the Courant number, which is dimensionless and has a maximum value limited to 1 by stability constraints. These conditions are typically used to limit the time step in *Godunov-type* codes.

3.3.6 Constrained Transport

The magnetic field is evolved using the *constrained transport* (CT) method, which ensures that the solenoidal condition expressed by Equation (2.36) is satisfied to machine precision at all times (see Mignone et al., 2019).

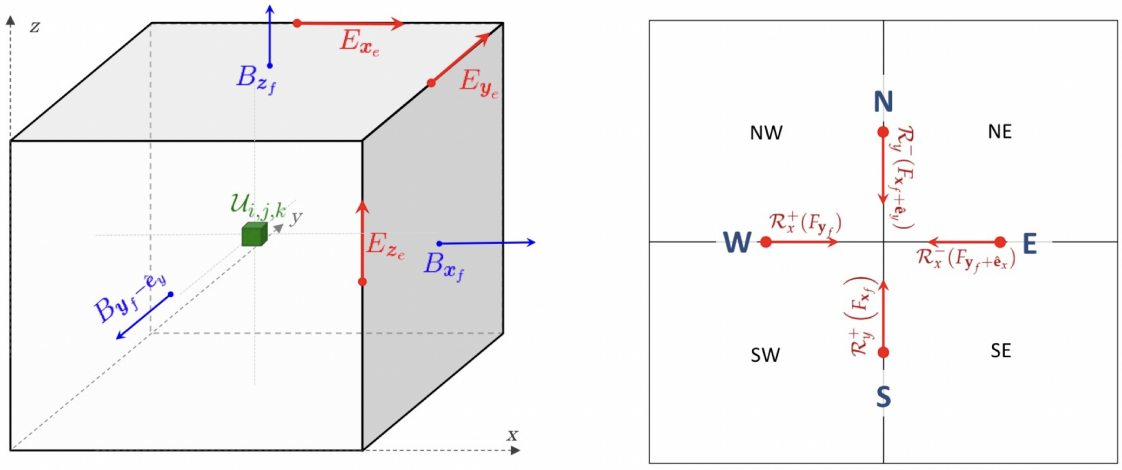

Figure 3.4: *Left panel*: Position of MHD variables by using the CT formalism. *Right panel*: Intersection between four neighbor zones viewed from the top. Credit: Mignone and Del Zanna (2021).

The CT method was originally introduced by Evans and Hawley (1988), and later extended to Godunov-type schemes by Balsara and Spicer (1999), Londrillo and del Zanna (2004) and Gardiner and Stone (2005), to name just a few. This method entails a staggered discretization of magnetic field whereby different components lie on the face they are orthogonal to (Mignone, 2017) so that a discrete version of Stoke's law can be applied when solving the induction equation. Conversely, primary zone-centered flow variables including density, momentum, and energy are stored by their volume averages inside the zone. The position of variables in a cell by using the CT formalism is illustrated in Figure 3.4.

A staggered representation is necessary to preserve the magnetic field divergence-free constraint in Godunov-type shock-capturing schemes, where spatial partial derivatives do not commute when discontinuities are present. Mignone and Del Zanna (2021) defined the staggered electromagnetic quantities as

$$\mathbf{B}_f \equiv \begin{pmatrix} B_{\mathbf{x}_\mathrm{f}} \\ B_{\mathbf{y}_\mathrm{f}} \\ B_{\mathbf{z}_\mathrm{f}} \end{pmatrix} = \begin{pmatrix} B_{x,i+\frac{1}{2},j,k} \\ B_{y,i,j+\frac{1}{2},k} \\ B_{z,i,j,k+\frac{1}{2}} \end{pmatrix}, \qquad \mathbf{E}_e \equiv \begin{pmatrix} E_{\mathbf{x}_\mathrm{e}} \\ E_{\mathbf{y}_\mathrm{e}} \\ E_{\mathbf{z}_\mathrm{e}} \end{pmatrix} = \begin{pmatrix} E_{x,i,j+\frac{1}{2},k+\frac{1}{2}} \\ E_{y,i+\frac{1}{2},j,k+\frac{1}{2}} \\ E_{z,i+\frac{1}{2},j+\frac{1}{2},k} \end{pmatrix}, \tag{3.24}$$

where the subscripts $\mathbf{x}_f$, $\mathbf{y}_f$, and $\mathbf{z}_f$ identify the face-centered staggered location inside the control volume, while $\mathbf{x}_e$, $\mathbf{y}_e$, and $\mathbf{z}_e$ represent the corresponding positions of the different edge-centered electric field components. When a finite-volume approach is considered, conserved variables are evolved

in terms of their volume-averages $\mathcal{U}_c$, namely

$$\frac{d\mathcal{U}_c}{dt} = -\left(\frac{\Delta_x \hat{F}_{\mathbf{x}_f}}{\Delta x} + \frac{\Delta_y \hat{F}_{\mathbf{y}_f}}{\Delta y} + \frac{\Delta_z \hat{F}_{\mathbf{z}_f}}{\Delta z}\right), \tag{3.25}$$

where Δx, Δy, and Δz are the coordinate grid spacing, Δ_x, Δ_y, Δ_z are the backward difference operators defined as

$$\Delta_x \mathcal{Q}_c \equiv \mathcal{Q}_c - \mathcal{Q}_{c-\hat{\mathbf{e}}_x}, \quad \Delta_y \mathcal{Q}_c \equiv \mathcal{Q}_c - \mathcal{Q}_{c-\hat{\mathbf{e}}_y}, \quad \Delta_z \mathcal{Q}_c \equiv \mathcal{Q}_c - \mathcal{Q}_{c-\hat{\mathbf{e}}_z}, \tag{3.26}$$

where $\mathcal{Q}$ can be either a face-centered quantity ($\mathcal{Q}_f$) or a edge-centered quantity ($\mathcal{Q}_e$), while $\hat{\mathbf{e}}_x = (1,0,0)$, $\hat{\mathbf{e}}_y = (0,1,0)$, and $\hat{\mathbf{e}}_z = (0,0,1)$ are unit vectors. The evolution of $\mathcal{U}_c$ implies a surface-average representation of the fluxes at the zone interface, leading to

$$\begin{aligned}
\hat{F}_{\mathbf{x}_f} &= \frac{1}{\Delta y \Delta z} \int \hat{\mathbf{e}}_x \cdot \mathrm{F}(\mathcal{U}(x_{\mathrm{i}+\frac{1}{2}}, y, z, t)) dy dz, \\
\hat{F}_{\mathbf{y}_f} &= \frac{1}{\Delta z \Delta x} \int \hat{\mathbf{e}}_y \cdot \mathrm{F}(\mathcal{U}(x, y_{\mathrm{j}+\frac{1}{2}}, z, t)) dz dx, \\
\hat{F}_{\mathbf{z}_f} &= \frac{1}{\Delta x \Delta y} \int \hat{\mathbf{e}}_z \cdot \mathrm{F}(\mathcal{U}(x, y, z_{\mathrm{k}+\frac{1}{2}}, t)) dx dy,
\end{aligned} \tag{3.27}$$

as required by direct application of Gauss' theorem.
The staggered magnetic field components are also interpreted as face-averages and are updated using a discrete version of Stokes' theorem:

$$\begin{aligned}
\frac{dB_{\mathbf{x}_f}}{dt} &= -\left(\frac{\Delta_y \hat{E}_{\mathbf{z}_e}}{\Delta y} - \frac{\Delta_z \hat{E}_{\mathbf{y}_e}}{\Delta z}\right), \\
\frac{dB_{\mathbf{y}_f}}{dt} &= -\left(\frac{\Delta_z \hat{E}_{\mathbf{x}_e}}{\Delta z} - \frac{\Delta_x \hat{E}_{\mathbf{z}_e}}{\Delta x}\right), \\
\frac{dB_{\mathbf{z}_f}}{dt} &= -\left(\frac{\Delta_x \hat{E}_{\mathbf{y}_e}}{\Delta x} - \frac{\Delta_y \hat{E}_{\mathbf{x}_e}}{\Delta y}\right),
\end{aligned} \tag{3.28}$$

where

$$\begin{aligned}
\hat{E}_{\mathbf{x}_e} &= \frac{1}{\Delta x} \int E_x(x, y_{j+\frac{1}{2}}, z_{k+\frac{1}{2}}, t) dx, \\
\hat{E}_{\mathbf{y}_e} &= \frac{1}{\Delta y} \int E_y(x_{i+\frac{1}{2}}, y, z_{k+\frac{1}{2}}, t) dy, \\
\hat{E}_{\mathbf{z}_e} &= \frac{1}{\Delta z} \int E_z(x_{i+\frac{1}{2}}, y_{j+\frac{1}{2}}, z, t) dz.
\end{aligned} \tag{3.29}$$

In PLUTO, the line-average electric field (i.e., the electromotive force or emf) is constructed using the information available from one-dimensional, face-centered *Riemann solver* by a proper emf averaging/reconstruction scheme, chosen from

- CT-Contact (following the approach of Gardiner and Stone, 2005),
- UCT-HLL (see Del Zanna et al., 2003; Londrillo and del Zanna, 2004),
- UCT-HLLD described in Mignone and Del Zanna (2021).

The approach proposed by Balsara and Spicer (1999) was later improved by Gardiner and Stone (2005), leading to the CT-Contact method, which can operate reconstruction from any one of the four nearest face centers to the zone edge. In the notations of Mignone and Del Zanna (2021), the zone-centered emf is given by

$$\hat{E}_{\mathbf{z}_e} = \hat{E}^{\rm arithm}_{\mathbf{z}_e} + \frac{\Delta y}{8}\left[\left(\frac{\partial E_z}{\partial y}\right)^S - \left(\frac{\partial E_z}{\partial y}\right)^N\right] + \frac{\Delta x}{8}\left[\left(\frac{\partial E_z}{\partial x}\right)^W - \left(\frac{\partial E_z}{\partial x}\right)^E\right], \tag{3.30}$$

where N, S, E and W represent the four cardinal directions with respect to the zone edge (see the right panel of Figure 3.4), while $\hat{E}^{\rm arithm}_{\mathbf{z}_e}$ is the arithmetic average, namely

$$\hat{E}_{\mathbf{z}_e} = \frac{1}{4}\left(-\hat{F}^{[B_y]}_{\mathbf{x}_f} - \hat{F}^{[B_y]}_{\mathbf{x}_f+\hat{\mathbf{e}}_y} + \hat{F}^{[B_x]}_{\mathbf{y}_f} + \hat{F}^{[B_x]}_{\mathbf{y}_f+\hat{\mathbf{e}}_x}\right), \tag{3.31}$$

where the square bracket indicates the flux component. However, this method could not be generalized to higher-order methods, as it could be at most 2$^{\rm nd}$-order accurate. A more rigorous approach for computational MHD is the upwind constrained transport (UCT) method originally proposed by Londrillo and del Zanna (2004). We refer to this approach as the UCT-HLL scheme, in which the edge-centered electric field is given by

$$\begin{aligned}\hat{E}_{\mathbf{z}_e} = &\frac{\alpha_x^+\alpha_y^+ E_z^{SW} + \alpha_x^+\alpha_y^- E_z^{NW} + \alpha_x^-\alpha_y^+ E_z^{SE} + \alpha_x^-\alpha_y^- E_z^{SW}}{(\alpha_x^+ + \alpha_x^-)(\alpha_y^+ + \alpha_y^-)} + \\ &+ \frac{\alpha_x^+\alpha_x^-}{\alpha_x^+ + \alpha_x^-}(B_y^E - B_y^W) - \frac{\alpha_y^+\alpha_y^-}{\alpha_y^+ + \alpha_y^-}(B_x^N - B_x^S),\end{aligned} \tag{3.32}$$

where $\alpha_x^+ = \max(0, \lambda^R_{\mathbf{x}_f}, \lambda^R_{\mathbf{x}_f+\hat{\mathbf{e}}_y})$ and $\alpha_x^- = -\min(0, \lambda^L_{\mathbf{x}_f}, \lambda^L_{\mathbf{x}_f+\hat{\mathbf{e}}_y})$. $\lambda^R_{\mathbf{x}_f}$ and $\lambda^L_{\mathbf{x}_f}$ represent the rightmost and leftmost characteristic speed, respectively. This method was simplified by Del Zanna et al. (2007) for the general

RMHD case, namely

$$\hat{E}_{\mathbf{z}_e} = -\frac{\alpha_x^+(\bar{v}_x B_y)^W + \alpha_x^-(\bar{v}_x B_y)^E - \alpha_x^+\alpha_x^-(B_y^E - B_y^W)}{\alpha_x^+ + \alpha_x^-} + \\ + \frac{\alpha_y^+(\bar{v}_y B_x)^S + \alpha_y^-(\bar{v}_y B_x)^N - \alpha_y^+\alpha_y^-(B_x^N - B_x^S)}{\alpha_y^+ + \alpha_y^-}, \tag{3.33}$$

with, e.g., $(\bar{v}_x B_y)^W = \bar{v}_x^W B_y^W$, where $\bar{v}_x = (v_x^L + v_x^R)_{\mathbf{y}_f}/2$, while $\bar{v}_y = (v_y^L + v_y^R)_{\mathbf{x}_f}/2$. The velocities in the transverse direction at an x-interface are first computed as

$$\bar{v}_{\mathrm{t},\mathbf{x}_f} = \frac{\alpha_x^+ \mathbf{v}_{\mathbf{x}_f}^L + \alpha_x^- \mathbf{v}_{\mathbf{x}_f}^R}{\alpha_x^+ + \alpha_x^-} \cdot \bar{\mathbf{e}}_{\mathrm{t}}, \tag{3.34}$$

where $t = y, z$ and then accurately reconstructed in the transverse direction. Mignone and Del Zanna (2021) extended this method to less dissipative solvers like HLLD, leading to the UCT-HLLD scheme. By using this scheme, the edge-centered emf can be constructed from

$$\hat{E}_{\mathbf{z}_e} = -[(a_x \bar{v}_x B_y)^W + (a_x \bar{v}_x B_y)^E] + [(a_y \bar{v}_y B_x)^N + (a_y \bar{v}_y B_x)^S] + \\ + [(d_x B_y)^E - (d_x B_y)^W] - [(d_y B_x)^N - (d_y B_x)^S], \tag{3.35}$$

where $a_x^{W,E}$ (or $a_x^{N,S}$) and $d_x^{W,E}$ (or $d_x^{N,S}$), that are the flux and diffusion coefficients respectively, are computed by averaging the corresponding expressions obtained at x- (or y-) interfaces with a 1D Riemann solver, with

$$a^L = \frac{1 + \mathbf{v}^*}{2}, \quad a^R = \frac{1 - \mathbf{v}^*}{2}, \quad d^s = \frac{1}{2}(\mathbf{v}^s - \mathbf{v}^*)\tilde{\chi}^s + \frac{1}{2}(|\lambda^{*s}| - \mathbf{v}^*\lambda^{*s}), \tag{3.36}$$

where $\tilde{\chi}^s = (\lambda^{*s} - \lambda^s)\chi^s$ (see Equation 3.16, while

$$\mathbf{v}^s = \frac{\lambda^{*s} + \lambda^s}{|\lambda^{*s}| + |\lambda^s|}, \quad \mathbf{v}^* = \frac{\lambda^{*R} + \lambda^{*L}}{|\lambda^{*R}| + |\lambda^{*L}|}. \tag{3.37}$$

The partial differential equations for $\mathcal{U}_c$ are solved by coupling the CT schemes to the Godunov-type method. Indeed, the inter-cell fluxes in Equation (3.27) are calculated by solving the Riemann problem (see Section 3.3.2). Mignone and Del Zanna (2021) shows that the UCT-HLLD emf reconstruction scheme for the magnetic field and velocity components from nearby intercell faces to cell edges coupled to the base HLLD Riemann solver employed for the fluid part is an accurate numerical scheme.

Figure 3.5 shows the thermal pressure of an ideal fluid at a time subsequent to the initial one (left panel) and the volume-integrated magnetic energy as a function of time (right panel) for different emf methods and using the HLLD Riemann solver in the case of a magnetized current sheet. We clearly note that the UCT-HLLD scheme is characterized by excellent stability and low diffusion when coupled with the HLLD Riemann solver. Indeed, magnetic reconnection is not triggered by numerical diffusion and the current sheet remains stable in its initial configuration, as we expected for an ideal fluid. The same seems to occur for the CT-Contact scheme. However, the amount of numerical dissipation obtained with the UCT-HLLD scheme could be even lower and this scheme can be extended to higher than 2^{nd}-order schemes. Consequently, it is crucial to use the HLLD scheme both in the fluid and induction equation. Indeed, the left panel of Fig. 3.5 for the HLLD base Riemann solver coupled with the UCT-HLL emf reconstruction shows that the current sheet reconnects even in the ideal case. This means that magnetic reconnection is triggered by the numerical diffusivity introduced by the UCT-HLL scheme for the induction equation. This is confirmed by the right panel, which shows that the magnetic energy remains nearly constant in time for the UCT-HLLD scheme (red curve) while it decreases when the UCT-HLL scheme (yellow curve) is used. Therefore, the UCT-HLL emf reconstruction is inherently more diffusive.

3.3.7 Particle mover: Boris integrator

Particle equations of motion (see Eq. 2.56) are solved using the standard Boris pusher, which is a time-reversible integrator and features good conservation properties for long-time simulations. Boris pusher is an implicit-position Verlet algorithm, described by the equations reported by Mignone

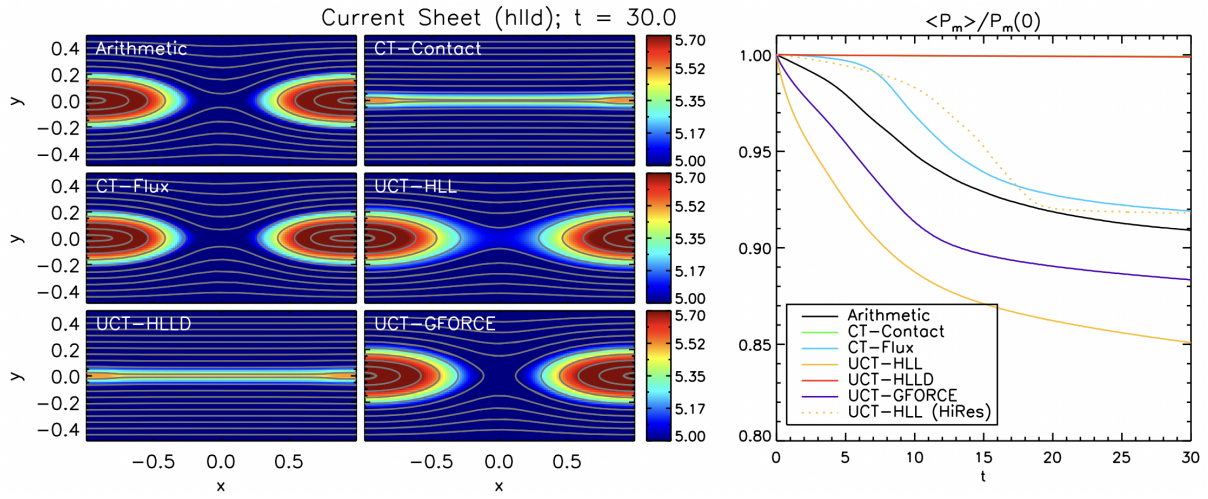

Figure 3.5: Current sheet evolution. *Left panels:* Thermal pressure of an ideal fluid at a time subsequent to the initial one, obtained with different emf methods and the HLLD Riemann solver. *Right panel:* Volume-integrated magnetic energy as a function of time again for different emf methods and the same Riemann solver (HLLD). Credit: Mignone and Del Zanna (2021).

et al. (2018), namely

$$
\begin{aligned}
\mathbf{x}_p^{n+\frac{1}{2}} &= \mathbf{x}_p^n + \frac{\Delta t^n}{2}\mathbf{v}_p^n, \\
\mathbf{u}_p^- &= \mathbf{u}_p^n + \frac{h}{2}c\mathbf{E}^{n+\frac{1}{2}}, \\
\mathbf{u}_p^+ &= \mathbf{u}_p^- + 2\frac{\mathbf{u}_p^- + \mathbf{u}_p^- \times \mathbf{b}}{1+\mathbf{b}^2} \times \mathbf{b}, \\
\mathbf{u}^{n+1} &= \mathbf{u}_p^+ + \frac{h}{2}c\mathbf{E}^{n+\frac{1}{2}}, \\
\mathbf{x}_p^{n+1} &= \mathbf{x}_p^{n+\frac{1}{2}} + \frac{\Delta t^n}{2}\mathbf{v}_p^{n+1},
\end{aligned}
\tag{3.38}
$$

where $\mathbf{b} = (h/2)\mathbf{B}^{n+\frac{1}{2}}/\gamma^{n+\frac{1}{2}}$, while $h = \Delta t^n (e/mc)_p$ is related to the simulation time step Δt^n. The particle mass is taken to be equal to the mass of the particles composing the fluid, so that, when written in code units, the charge to mass ratio $(e/mc)_p$ becomes unity. In other words, the results described in Section 4 and 5 are equally applicable to protons embedded in protons-electrons thermal fluid or to a electron-positron pair plasma. The electric and magnetic fields $\mathbf{E}$ and $\mathbf{B}$ are computed from the magnetized fluid and are properly interpolated at the particle position, following the approach of Mignone et al. (2018).

As discussed in Mignone et al. (2018), the particle time step can be constrained either by (the inverse of) their gyration frequency or by the maximum number of computational zones that can be crossed during a single time step. In the simulations carried out during this thesis work, both are found to be smaller than the fluid time step by a factor of ~ 5 at nominal resolutions. While gyration dominates the time step restriction at low grid resolutions, the opposite situation is found as the mesh becomes finer, since the most energetic particles can cross increasingly more cells in a single time step.
In our code, particles and fluid are evolved simultaneously, the former with the Boris algorithm and the latter with the RK3 time-stepping method. The fluid evolves for a whole step, then particles are updated using the fields calculated at time $n+1/2$ (obtained as the arithmetic mean between values at n and $n+1$).

3.4 Numerical setup

The initial configuration considers a 2D rectangular domain of size $L \times L/2$ where $L = 2 \times 10^4\ c/\omega_p$. The equilibrium magnetic field follows a *Harris-sheet profile*,

$$B_x(y) = B_0 \tanh\left(\frac{y}{a}\right), \tag{3.39}$$

where a denotes the initial width of the current sheet, which is set to $a = 250\ c/\omega_p$ in all the simulations, while B_0 denotes the magnetic field strength, normalized such that out unit velocity is the Alfvén speed ($\rho_0 = B_0 = 1$ in code units). The guide field B_z is not present and an initial equilibrium condition is obtained by counteracting the Lorenz-force term with a thermal pressure gradient,

$$P(y) = \frac{1}{2}B_0^2(\beta + 1) - \frac{1}{2}B_x^2(y), \tag{3.40}$$

so that the total pressure remains constant through the sheet (i.e., no magnetic tension is present initially). β is set to 0.01 in all simulations. For convenience, resistivity is prescribed from $\bar{S}$, that is the Lundquist number corresponding to the current sheet width (see Equation 2.51). v_A is set to one, while the resistivity η is assumed constant throughout the domain.

The system is perturbed by introducing a fixed number of small-amplitudes modes with different wavenumbers k. This is best achieved by redefining the vector potential as $A_z(x,y) = A_0(y) + \delta A_z(x,y)$ where $A_0(y) = aB_0 \log(\cosh(y/a))$ corresponds to the equilibrium field (see Equation 3.39), while

$$\delta A_z(x,y) = \frac{\epsilon B_0}{N_m} \sum_{m=0}^{N_m} \frac{1}{k} \sin(kx + \phi_m) \operatorname{sech}\left(\frac{y}{a}\right) \tag{3.41}$$

is the perturbed term, where N_m is the number of modes (set to 20), $\epsilon = 10^{-3}$ is the perturbation amplitude, ϕ_m are random phases and $k = (m+1)k_0 = 2\pi(m+1)/L$. We note that we also tried two types of perturbation on the vertical velocity (i.e, v_y). However, these resulted in a perturbation growth that was too small for our purposes.
Test-particles are evenly assigned to grid zones (1 particle/cell) and their velocities follow a Maxwellian distribution with standard deviation $\sigma_d = \sqrt{P_0/2\rho_0}$, where $P_0 = P(\infty)$ in Equation (3.40). Test-particles are evolved together with the fluid until the end of the computational time.
Boundary conditions in the x-direction are periodic, while in the y-direction are reflective.

3.4.1 Chosen numerical schemes

As one of the aims of this thesis is to quantify the impact of the numerical scheme on simulation results, three different numerical schemes based on different combinations of the base Riemann solver (see Section 3.3.2) and the emf averaging/reconstruction scheme (see Section 3.3.6) are compared, namely,

i) the HLL Riemann solver with the UCT-HLL reconstruction (see Londrillo and del Zanna, 2004; Del Zanna et al., 2007);
ii) the Roe Riemann solver with the CT-Contact emf averaging scheme;
iii) the HLLD Riemann solver of Miyoshi and Kusano (2005) with the more recent UCT-HLLD emf averaging scheme;

which, for brevity, will be shortened as HLL (i), Roe (ii), and HLLD (iii). The HLLD scheme is characterized by a reduced amount of numerical dissipation, as discussed in Section 6.2 of Mignone and Del Zanna (2021), for which the diffusive flux terms eventually contributing to the emf evaluation are proportional to the jump in magnetic fields alone.
While the code retains a global 2$^{\text{nd}}$-order accuracy, the amount of numerical

dissipation can be further controlled by the spatial reconstruction of fluid variables inside each grid zone. For this reason, both 2nd-order piecewise linear reconstruction and the 5th-order WENO-Z algorithm are considered (see Section 3.3.1).
A 3rd-order Runge Kutta stepping is used to advance the equations in time (see Section 3.3.5). Unless otherwise stated, the final integration time is $\omega_p t_{\rm stop} = 6 \cdot 10^5$, as it is enough for all models to capture both the linear stages as well as the nonlinear evolution. Notice that, for convenience, time can also be measured in units of the Alfvén time-scale $\bar{\tau}_A = a/v_A = 250c/(v_A\omega_p)$. In practice, the corresponding Alfvén time can be obtained from the simulation time (in units of $1/\omega_p$) as $t/\bar{\tau}_A = \omega_p t v_A/(250c)$.
Numerical simulations are conducted using different values of the Lundquist number $\bar{S}$ defined in Equation (2.51), namely, $\bar{S} = 10^3, 10^4, 10^5$ and $\bar{S} = \infty$ (ideal case, i.e., $\eta = 0$) with varying grid resolutions ($N_x \times N_x/2$), starting from $N_x = 192$ (which corresponds to $a/\Delta x \sim 2.5$ zones on the initial current sheet width a) up to $N_x = 3072$ ($a/\Delta_x \sim 40$). Correspondingly, the number of particles varies from $18,432$ (at the lowest resolution) and reaches $4,718,592$ (at the largest one).

3.4.2 Dynamical contributions of convective and resistive electric fields

In addition to studying the impact of the numerical method and resistivity on the simulation results, this thesis work focuses on the relative importance of the two electric field contributions shown in Equation (2.37) in the particle acceleration mechanism.
Each electric field contribution exerts a work on particles with a corresponding change in their kinetic energy $E_{\rm kin} = (\gamma - 1)\mathbb{C}^2$. During a single time step Δt^n this variation is given by the sum of the two contributions

$$\Delta E^n_{\rm kin} = h^n c(\mathbf{E}_c \cdot \mathbf{v}_p + \mathbf{E}_r \cdot \mathbf{v}_p)^n. \tag{3.42}$$

To quantify the importance of the two contributions, the energy gained by the particles is used, which, following Equation (3.42), is split into

$$W = \sum_n (hc\mathbf{E}_c \cdot \mathbf{v}_p)^n + \sum_n (hc\mathbf{E}_r \cdot \mathbf{v}_p)^n \equiv W_c + W_r, \tag{3.43}$$

where n indicates the step number. This equation can be rewritten in

terms of the particle four-velocity $\mathbf{u}_p$ this way

$$W = \sum_n \left(\frac{h}{\gamma}\mathbf{E}_c \cdot \mathbf{u}_p\right)^n + \sum_n \left(\frac{h}{\gamma}\mathbf{E}_r \cdot \mathbf{u}_p\right)^n \equiv W_c + W_r, \tag{3.44}$$

where $\gamma = \sqrt{1 + u_p^2/\mathbb{C}^2}$ is the Lorentz γ-factor. Simulations for this analysis are carried out with the 5^{th}-order WENO-Z reconstruction algorithm in combination with the HLLD Riemann solver and the UCT-HLLD emf averaging scheme. The final integration time is $\omega_p t = 7.8 \cdot 10^5$ to capture even the non-linear evolution of the current sheet. The redefined Lundquist number $\bar{S}$ is set to 10^4. The grid resolution is set to 1536×768 (i.e., $a/\Delta x \sim 20$) and then progressively doubled up to 6144×3072 (i.e., $a/\Delta x \sim 80$ and 18,874,368 particles), in order to determine convergence even in the non-linear evolution phase of the current sheet. Moreover, to investigate the importance of the resistive field, numerical computations are carried out twice by first including and then removing the resistive contribution from the equation of motion of the particles, while always keeping it during the fluid evolution. This means that the fluid evolution is the same in both cases while only the particles evolution differs.

4

The impact of the numerical method

This chapter is based on the paper published on the *Monthly Notices of the Royal Astronomical Society* by Eleonora Puzzoni, Andrea Mignone, and Gianluigi Bodo, titled: On the impact of the numerical method on magnetic reconnection and particle acceleration - I. The MHD case (Puzzoni et al., 2021). The author of this thesis carried out all the simulations, created all the figures, and mostly discussed and interpreted the data presented in this chapter.
In this chapter, the results regarding the impact of the numerical method and the resistivity on magnetic reconnection and particle acceleration in the MHD case are presented. First, a convergence study for the background plasma alone is introduced, in which the effect of spatial reconstruction, Reimann solver, emf averaging scheme, and resistivity on the evolution of the current sheet is presented. After, the same study is applied to particle acceleration.

4.1 Convergence study for the background plasma

The impact of the numerical method and resistivity on the dynamical evolution of the tearing-unstable current sheet is first studied.
The temporal evolution of the plasma density, obtained with the HLLD scheme and $\bar{S} = 10^4$ at the largest grid resolution (i.e., $N_x = 3072$), is shown in Figure 4.1. For $10^5 \lesssim \omega_p t \lesssim 2.1 \cdot 10^5$ (upper left-hand panel) the current sheet starts to shrink at the edges of the computational domain and the tearing-mode heads its linear phase. The process continues as the current sheet becomes thinner and thinner for $2.1 \cdot 10^5 \lesssim \omega_p t \lesssim 3.4 \cdot 10^5$ (upper right-hand panel), therefore this phase is called the second linear phase in this thesis work. Subsequently, at about $3.4 \cdot 10^5 \lesssim \omega_p t \lesssim 4.6 \cdot 10^5$ the current sheet starts to fragment into plasmoids that begin to merge (lower left-hand panel). Eventually, for $\omega_p t \gtrsim 4.6 \cdot 10^5$ the system reaches

a saturation phase where plasmoids merged into a single large island with a large filling factor (lower right-hand panel).
Regardless of the numerical scheme, these four evolutionary stages are observed at all resolutions, albeit the beginning of each phase may occur at a different time. A convenient way to label the different evolutionary stages can be quantified by counting the number of X-points formed over time. The algorithm, based on locating the null points of $|\mathbf{B}|$, is illustrated in Appendix A and is compatible with the one developed by Zhdankin et al. (2013).
As an additional diagnostic tool, a quantitative measure of the growth rate γ_{TM} is provided, obtained as

$$\gamma_{\mathrm{TM}} = \frac{f(t_2) - f(t_1)}{t_2 - t_1}, \tag{4.1}$$

where t_1 and t_2 correspond to two simulation snapshot times, while

$$f(t) = \frac{1}{2} \log \left(\frac{1}{L^2} \int B_y^2(t)\, dx\, dy \right). \tag{4.2}$$

Equation (4.1) is employed to evaluate the growth rate within the 1$^{\mathrm{st}}$- and 2$^{\mathrm{nd}}$-linear phases in what follows.

4.1.1 The effect of spatial reconstruction

The temporal evolution of the spatially averaged transverse component of the magnetic field at different resolutions using linear reconstruction and WENO-Z 5$^{\mathrm{th}}$-order reconstruction are plotted in the top and middle left panels of Figure 4.2, respectively. The right panels give the corresponding number of X-points at the largest resolutions ($768 \leq N_x \leq 3072$). For the sake of comparison, results with both reconstruction schemes at $N_x = 3072$ are superimposed in the lower panels.
For this case, the Lundquist number is set to $\bar{S} = 10^4$ and the HLLD Riemann solver with the UCT-HLLD reconstruction scheme for emf computation at cell edges is employed. The different evolutionary stages, described above, have been marked by the vertical dashed lines. During the linear phases, the perturbations are expected to grow exponentially at the rate of the fastest growing mode, as predicted by linear theory (see Section 2.4.2). The same does not hold during the subsequent phase where a variation of the magnetic energy is visible depending on the chosen scheme and grid

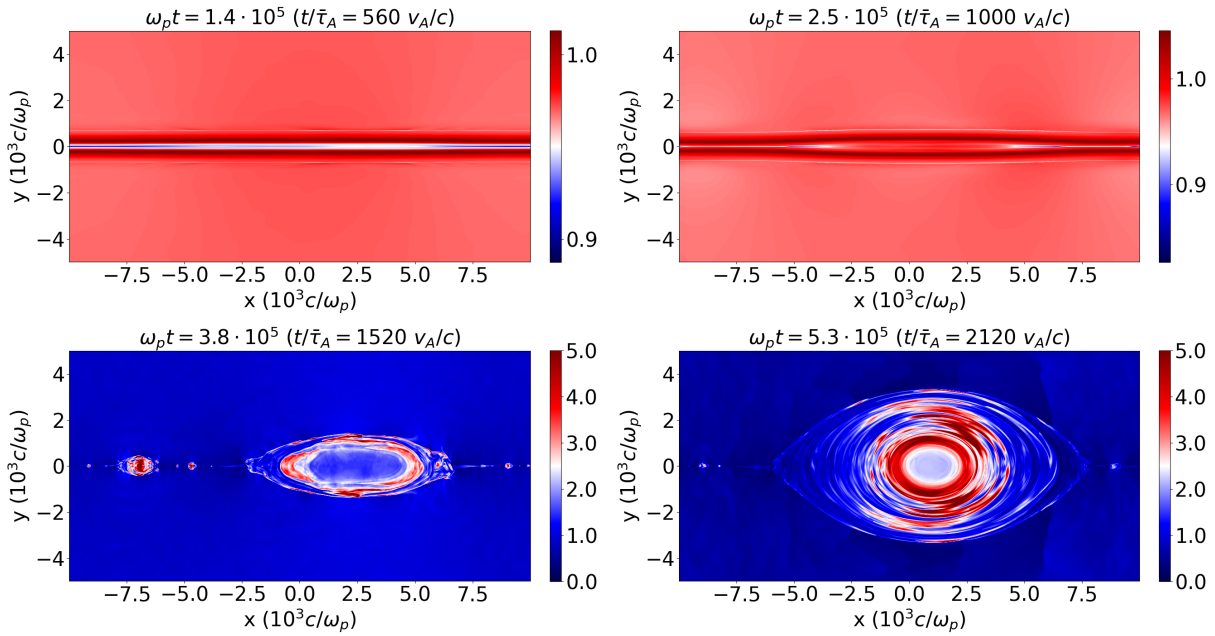

Figure 4.1: Plasma density (colorbar) at four simulation snapshots, obtained with a grid resolution $N_x = 3072$, the UCT-HLLD scheme and the HLLD Riemann solver with $\bar{S} = 10^4$ and the WENO-Z reconstruction scheme. Time is expressed in units of both the inverse plasma frequency and the Aflvénic time scale (in parenthesis).

size. In fact, during the second phase, the width of the current sheet continues to decrease, eventually leading to its fragmentation through the formation of X-points. To accurately capture this phase, an even larger resolution is needed for resolving the increasingly thinner sheets.

A direct inspection of the left and corresponding right panel reveals that the growth of the perturbation raises with the number of newly formed X-points. Since this process occurs more rapidly as the numerical diffusion is reduced, higher resolution runs with WENO-Z reconstruction evolve towards the growth of saturation earlier. On the contrary, at low resolutions, the saturation stage is attained at later times or may not be reached at all by the end of the simulation, especially with linear reconstruction where numerical diffusion is larger. Focusing on the linear phases, convergence is eventually reached for $N_x \gtrsim 1536$ ($a/\Delta x \simeq 20$) for the linear reconstruction case and $N_x \gtrsim 768$ ($a/\Delta x \simeq 10$) using WENO-Z. At the highest resolution, both linear and WENO-Z schemes show similar growths (see lower panels of Figure 4.2).

Growth rates for the 1$^{\text{st}}$ and 2$^{\text{nd}}$-linear phase, computed using Equation (4.1), are reported in Table 4.1. During the 1$^{\text{st}}$-linear stage, both compu-

Table 4.1: Average growth rates (for $\bar{S} = 10^4$ case) for the tearing mode instability, γ_{TM}, measured from the simulations at different grid resolutions (left column) using HLLD with linear and WENO-Z reconstructions. These are calculated within what we call the 1st- ($10^5 \lesssim \omega_p t \lesssim 2.1 \cdot 10^5$ or, equivalently, $400 \lesssim t/\bar{\tau}_A \lesssim 840$) and the 2nd-linear phase ($2.1 \cdot 10^5 \lesssim \omega_p t \lesssim 3.4 \cdot 10^5$ or, equivalently, $840 \lesssim t/\bar{\tau}_A \lesssim 1360$).

		1st-linear phase γ_{TM} ($10^{-5}\omega_p$)		2nd-linear phase γ_{TM} ($10^{-6}\omega_p$)	
Resolution	$a/\Delta x$	Linear	WENO-Z	Linear	WENO-Z
192 × 96	~ 2.5	0.80	1.29	6.38	9.24
384 × 192	~ 5	1.40	1.68	8.93	9.14
768 × 384	~ 10	1.76	1.88	9.58	9.80
1536 × 768	~ 20	1.88	1.89	10.2	8.85
3072 × 1536	~ 40	1.89	1.90	12.3	12.2

tations eventually converge to the same result, albeit the employment of WENO-Z favors faster convergence (approximately half the resolution is needed), owing to the reduced numerical dissipation. The 2nd-linear phase takes place more rapidly and starts earlier as the numerical dissipation is reduced, either with the reconstruction order or with a finer mesh spacing.

4.1.2 The impact of the Riemann solver and emf averaging

Next, the influence of the Riemann solver as well as the emf-averaging scheme on the computations is determined. Figure 4.3 shows the evolution over time of the spatially averaged transverse component of the magnetic field at different grid resolutions for selected Riemann solvers and emf-averaging schemes (see Section 3.4). Resistive ($\bar{S} = 10^4$) and ideal ($\bar{S} = \infty$) cases are shown in the left and right panels, respectively.

In the resistive case, using the HLL and Roe schemes (top and middle left-hand panels, respectively), the growth rate flattens as the mesh becomes finer and convergence during the 1st- and 2nd-linear phase is achieved for $N_x \gtrsim 768$. Conversely, computations using the HLLD method (bottom left panel) reveal a more homogeneous profile where the different evolutionary phases are clearly distinguished at (nearly) all resolutions, giving comparable growth and convergence properties. This behavior has to be attributed to the reduced amount of numerical dissipation of the HLLD Riemann solver with the UCT-HLLD emf scheme, as discussed in Section 3.3.6.

Note that, in the ideal case ($\bar{S} = \infty$, right panels), the equilibrium con-

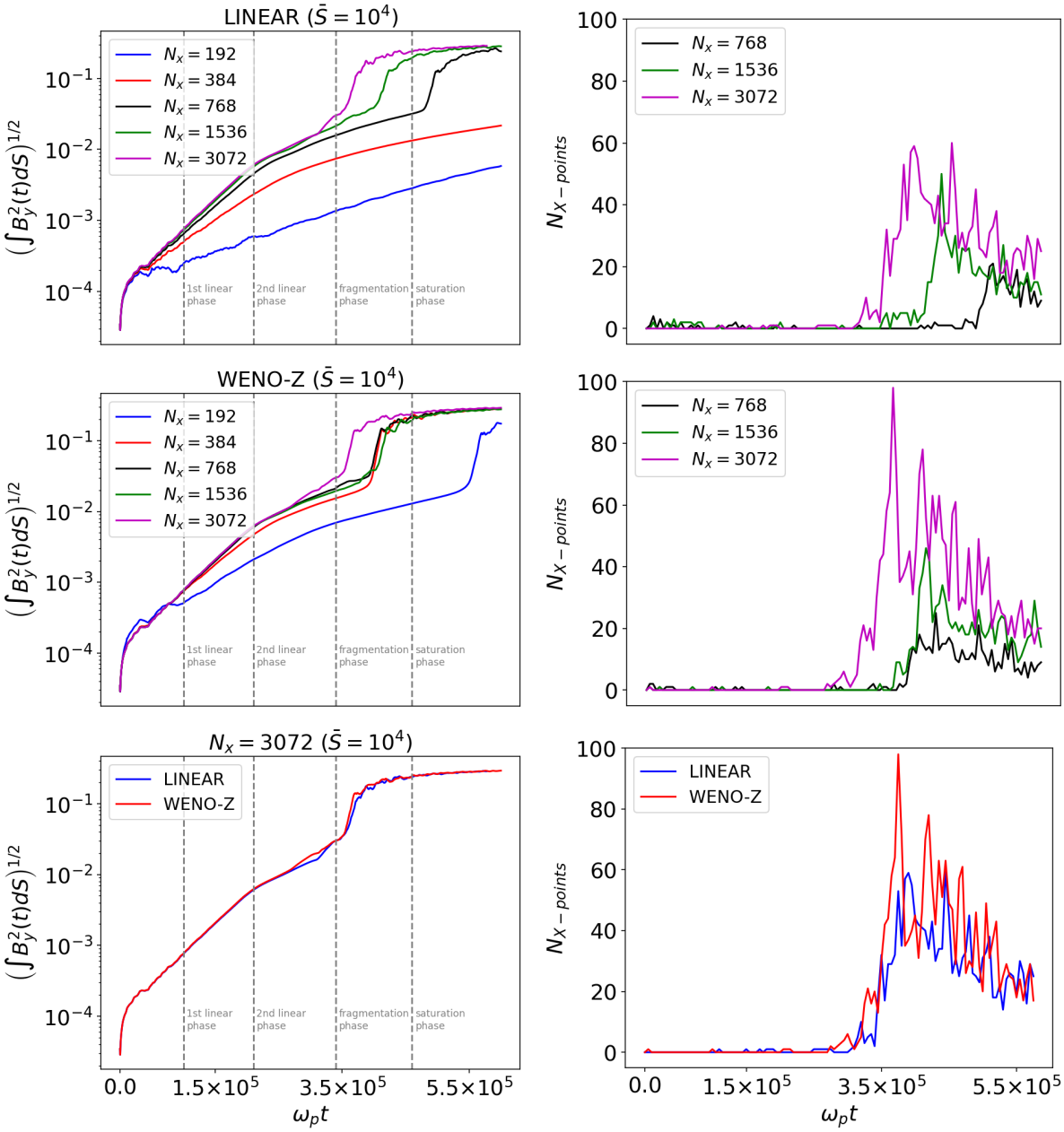

Figure 4.2: *Left panels:* spatially-averaged transverse component of magnetic field as a function of time at different grid resolutions, using linear (top panel) and WENO-Z (middle panel) reconstructions. The bottom panel compares the two reconstructions at the largest resolution ($N_x = 3072$). Note that time is expressed in units of the inverse plasma frequency and it can be converted to Alfvénic time units using $t/\bar{\tau}_A = \omega_p t/250$. *Right panels*: number of X-points formed over time at higher resolutions using linear (top panel) and WENO-Z (middle panel) reconstruction with a comparison of these at $N_x = 3072$ (bottom panel). We used $\bar{S} = 10^4$ and the HLLD Riemann solver with the UCT-HLLD scheme in all cases.

dition given by Equation (3.40) is a stationary solution of the ideal MHD equations and any dissipative process should be absent. In practice, however, the discretization process introduces a numerical viscosity/resistivity which allows the current sheet to reconnect to some extent. Generally speaking, the rate at which field dissipation occurs should depend on the amount of numerical diffusion: more dissipative schemes or lower resolutions will trigger reconnection events earlier. This is clearly the case for the Roe and the HLL schemes for which convergence will never be reached owing to the resolution-dependent numerical resistivity. The employment of the HLLD scheme reveals, once more, an unexpected benefit: the system remains stable with minimal dissipation at all resolutions and no perturbation growth, as one would expect for an ideal system. The same behavior has been witnessed in simulations of ideal current sheets, as described by Mignone and Del Zanna (2021) (see Section 6.2 of that paper). This proves that the introduction of a physical resistivity is absolutely essential to ensure convergence concerning the numerical method and mesh size in simulations of reconnecting current sheets. This is remarkably true during the linear phase(s), although a word of caution is noteworthy. For the sake of comparison, in fact, Figure 4.4 plots the spatially averaged transverse component of the magnetic field over time at the two largest resolutions for the selected schemes. While convergence is reached during the 1^{st}-linear phase ($\omega_p t \lesssim 2.1 \cdot 10^5$), the same does not hold during the subsequent phase where a variation of the magnetic energy is visible depending on the chosen scheme and grid size. In fact, during the 2^{nd}-linear phase, the width of the current sheet continues to decrease, eventually leading to its fragmentation through the formation of X-points. To accurately capture this phase, an even larger resolution is needed for resolving the increasingly thinner sheets.

From these initial results, it is clear that the HLLD combination scheme with WENO-Z reconstruction seems to produce the most accurate results and it will be employed as the fiducial numerical scheme.

4.1.3 Dependence on the Lundquist number

Figure 4.5 shows the spatially averaged transverse component of the magnetic field over time for different values of $\bar{S}$ and grid resolutions. Note that the saturation phase occurs at later times when $\bar{S}$ increases, i.e., as

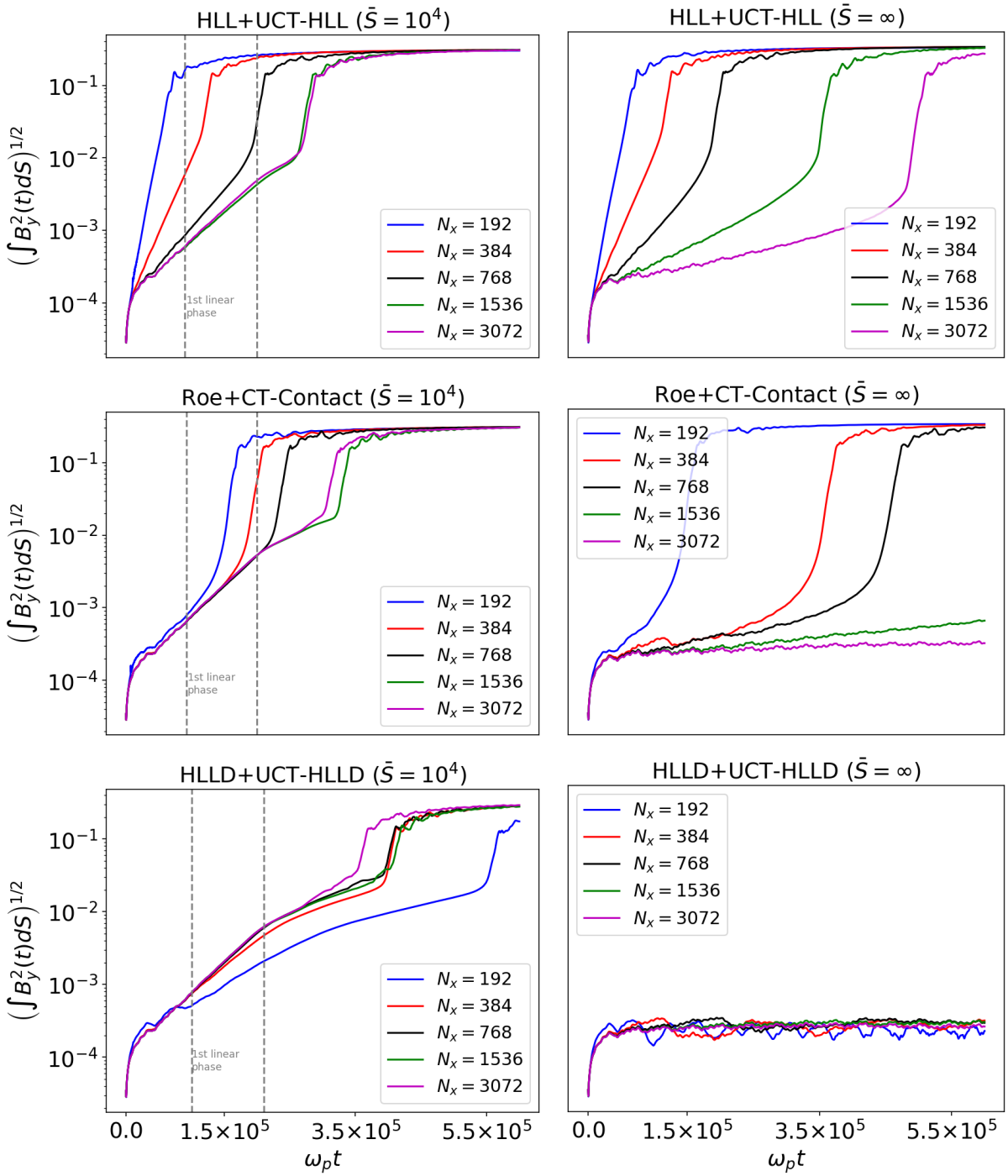

Figure 4.3: Spatially-averaged transverse component of magnetic field as a function of time for different resolutions and selected numerical schemes, with $\bar{S} = 10^4$ (left panels) and $\bar{S} = \infty$ (right panels). The WENO-Z reconstruction is used for all computations. Convergence refers to the 1$^{\text{st}}$ linear phase only (larger resolution is needed to resolve smaller current sheets forming after the fragmentation phase).

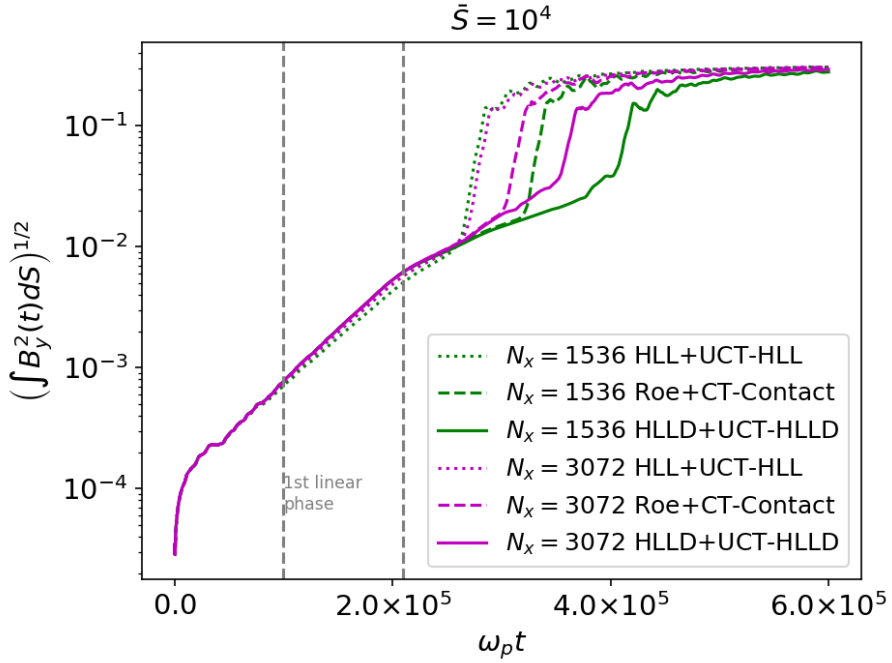

Figure 4.4: Same as Figure 4.3 but with plots from different numerical methods overlapping at the two largest resolutions ($\bar{S} = 10^4$). As before, convergence refers to the 1st-linear phase only.

the physical resistivity decreases. For this reason, when $\bar{S} = 10^5$ (see lower panel), the final simulation time has been extended to $\omega_p t_{\rm stop} \approx 1.8 \cdot 10^6$, i.e., three times than for the previous cases. The results indicate that the system evolution converges at an increasingly larger grid resolution depending, as expected, on the relative magnitude between numerical and physical resistivity, scaling as $\eta_{\rm num} \sim {\rm O}(\Delta x^2)$ and $\eta \sim 1/\bar{S}$, respectively[1]. Therefore, as an order of magnitude, the resolution threshold for convergence is expected to scale approximately as $a/\Delta x \sim 10\sqrt{\bar{S}/10^4}$ for a 2nd-order accurate scheme. Indeed, for $\bar{S} = 10^3$ (see upper-left panel), convergence is observed at all resolutions ($a/\Delta x \gtrsim 3$). On the contrary, at $\bar{S} = 10^5$, convergence is fully attained only at $N_x \sim 3072$, while the low-resolution simulation (i.e., $N_x = 192$) shows that the linear growth proceeds slowly and the saturation phase is not even reached by the end of the simulation ($\omega_p t_{\rm stop} \approx 1.8 \cdot 10^6$).

It is interesting to compare the measured growth rate for the 1st-linear phase with the theoretical expectation (as done by Del Zanna et al., 2016,

[1]Note that, albeit the employment of 5th-order accurate reconstruction, the computations remain 2nd-order accurate.

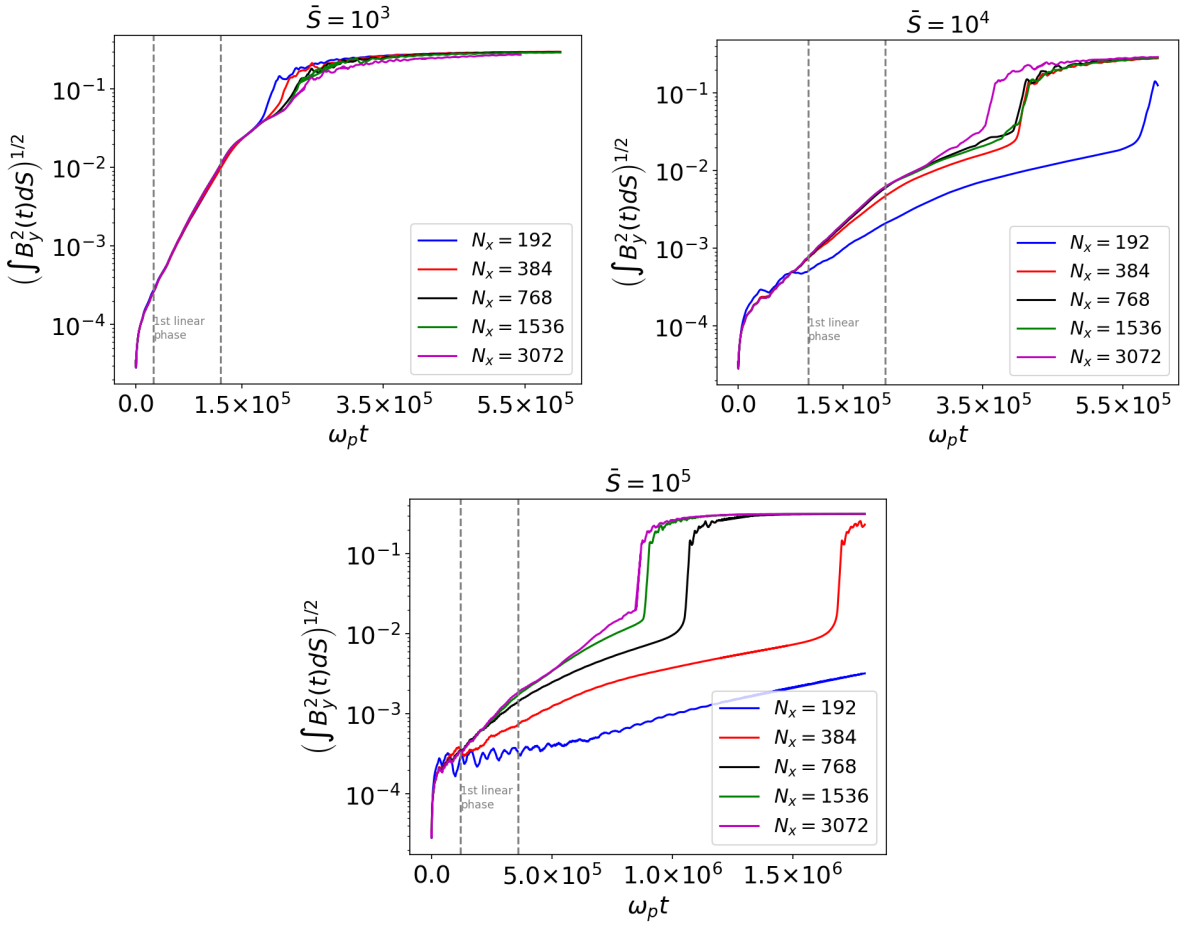

Figure 4.5: Spatially-averaged transverse component of magnetic field over time for different values of $\bar{S}$ at different resolutions. The HLLD scheme with WENO-Z reconstruction has been used. The vertical dashed lines mark the temporal range of the 1$^{\text{st}}$-linear phase during which convergence is reached.

see Section 2.4.2). Figure 4.6 shows the growth rate obtained from Equation (2.54) compared with that obtained from the simulations (Equation 4.1) for different values of $S = L\bar{S}/a$ with $\bar{S} = 10^3, 10^4, 10^5$. It is clear that $\gamma_{\text{TM}}\tau_A$ approaches the asymptotic value $\gamma_{\max}\tau_A$ as S increases. In fact, for $\bar{S} = 10^5$, $\gamma_{\text{TM}}\tau_A \approx 0.149$ and $\gamma_{\max}\tau_A \approx 0.152$ are obtained.

4.2 Test particle acceleration

The attention is now turned to the impact of the numerical method and resistivity on the dynamics and energetics of test-particles which evolve concurrently with the fluid.

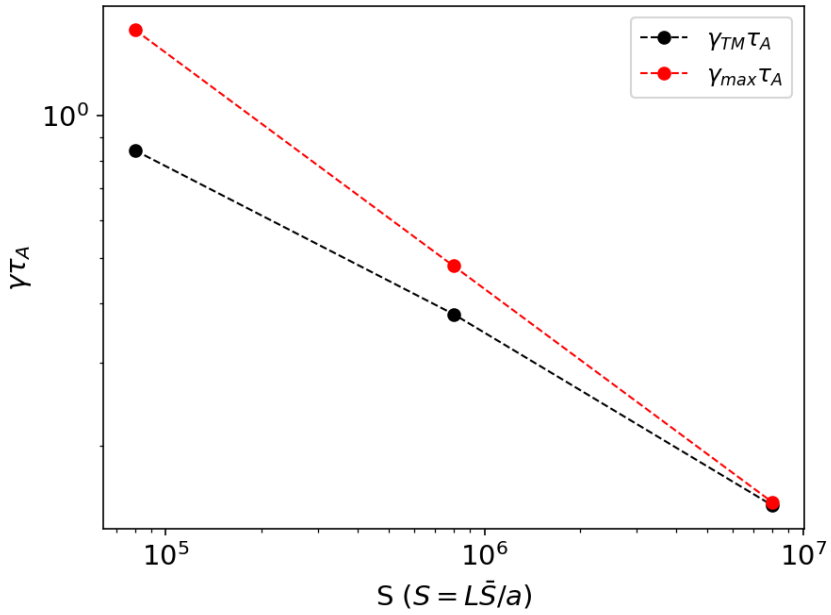

Figure 4.6: Comparison between the theoretical growth rate obtained from Eq. (2.54), in red, and that obtained from the simulations, in black, for different values of S.

4.2.1 Particle acceleration and energetics

The upper panel of Figure 4.7 shows the kinetic energy history of the most energetic particle, that is $E_{\rm kin} = u_p^2/(\gamma + 1)$. Notice that, as $\mathbb{C} = 10^4$, particles remain non-relativistic for the entire evolution ($\gamma \sim 1$). A sharp increase is first observed for $\omega_p t \gtrsim 3.6 \cdot 10^5$ when the particle enters one of the small magnetic islands after crossing an X-point (panel a), where a strong electric field boosts the particle velocity. Secondary acceleration events occur and continue concurrently with the process of repeated island merging (panel b) until the merger (panel c) with a large final plasmoid, within the most energetic particles remain trapped (panel d). Island mergers can lead to an extra particle energy boost, due to the anti-reconnection electric field at the secondary current sheet that forms perpendicular to the main one, at the interface between both islands (see, e.g., Oka et al., 2010; Sironi and Spitkovsky, 2014; Nalewajko et al., 2015; Cerutti, 2019). Once the particle enters the larger magnetic island, it undergoes a sharp acceleration inside the magnetized ring around the plasmoid center within which it is trapped. The particle increases its kinetic energy through the first-order Fermi process since the hosting plasmoid compresses while it merges with smaller islands while accreting particles and magnetic flux (see, e.g., Drake et al., 2010; Kowal et al., 2011; Guo et al., 2014; de Gou-

veia Dal Pino and Kowal, 2015; Guo et al., 2015; Petropoulou and Sironi, 2018; Hakobyan et al., 2021). When major mergers no longer occur and the plasmoid stabilizes, the particle energy remains approximately constant in time. Note that other energetic particles are also subject to the same acceleration mechanisms. As an illustrative example, Figure 4.8 shows a map of the magnetic field module (normalized to its maximum value), together with the position of the most energetic particles at the end of the simulation overplotted. As also found by Petropoulou and Sironi (2018), this figure indeed highlights that particles dominating the high-energy spectral cut-off reside in a strongly magnetized ring around the plasmoid core.

The upper panel of Figure 4.9 shows the temporal evolution of the particles energy distribution. For convenience, the energy range is broken into three portions identified with the low-energy end ($10^{-3} \lesssim E_{\rm kin} \lesssim 10^{-1}$), the power-law section $dN/dE_{\rm kin} \propto E_{\rm kin}^{-p}$ with slope $p \approx 1.7$ ($10^{-1} \lesssim E_{\rm kin} \lesssim 10^{2}$) and the high-energy cut-off ($10^{2} \lesssim E_{\rm kin} \lesssim 10^{4}$). The spectrum reaches an almost asymptotic shape during the saturation phase when $\omega_p t \gtrsim 4.4 \cdot 10^5$ ($t/\bar{\tau}_A \gtrsim 1760$, see bottom left-hand panel of Figure 4.3). Note that all spectra shown in this thesis are normalized to the total number of particles, which varies with the grid resolution. The middle and lower panels of Figure 4.9 show the particles spatial distribution at $\omega_p t \approx 4 \cdot 10^5$ and $\omega_p t \approx 6 \cdot 10^5$ coloured by the chosen energy ranges. The low-energy end of the spectra (i.e., the blue region) is determined by most of the particles in the domain which do not experience significant acceleration. These particles are predominantly found in the regions outside the plasmoids with spatial and velocity distributions remaining close to the initial values. Particles populating the power-law component of the spectrum (i.e., the orange region), on the contrary, are found in the proximity of the current sheet or settle in the outermost rings of the magnetic islands. Their number increases in time as the acceleration mechanism produces more energetic particles. Particles with the highest energy approximately (i.e., the red region), are settled inside the current sheet as reconnection begins and then gradually fill the central regions of the plasmoids as they form and merge with each other. At the end of the computation (see bottom panel), approximately ~ 51 per cent of particles fill the low-energy domain, ~ 47 per cent of particles populate the power-law section of the spectrum while ~ 2 per cent is represented by high-energy particles.

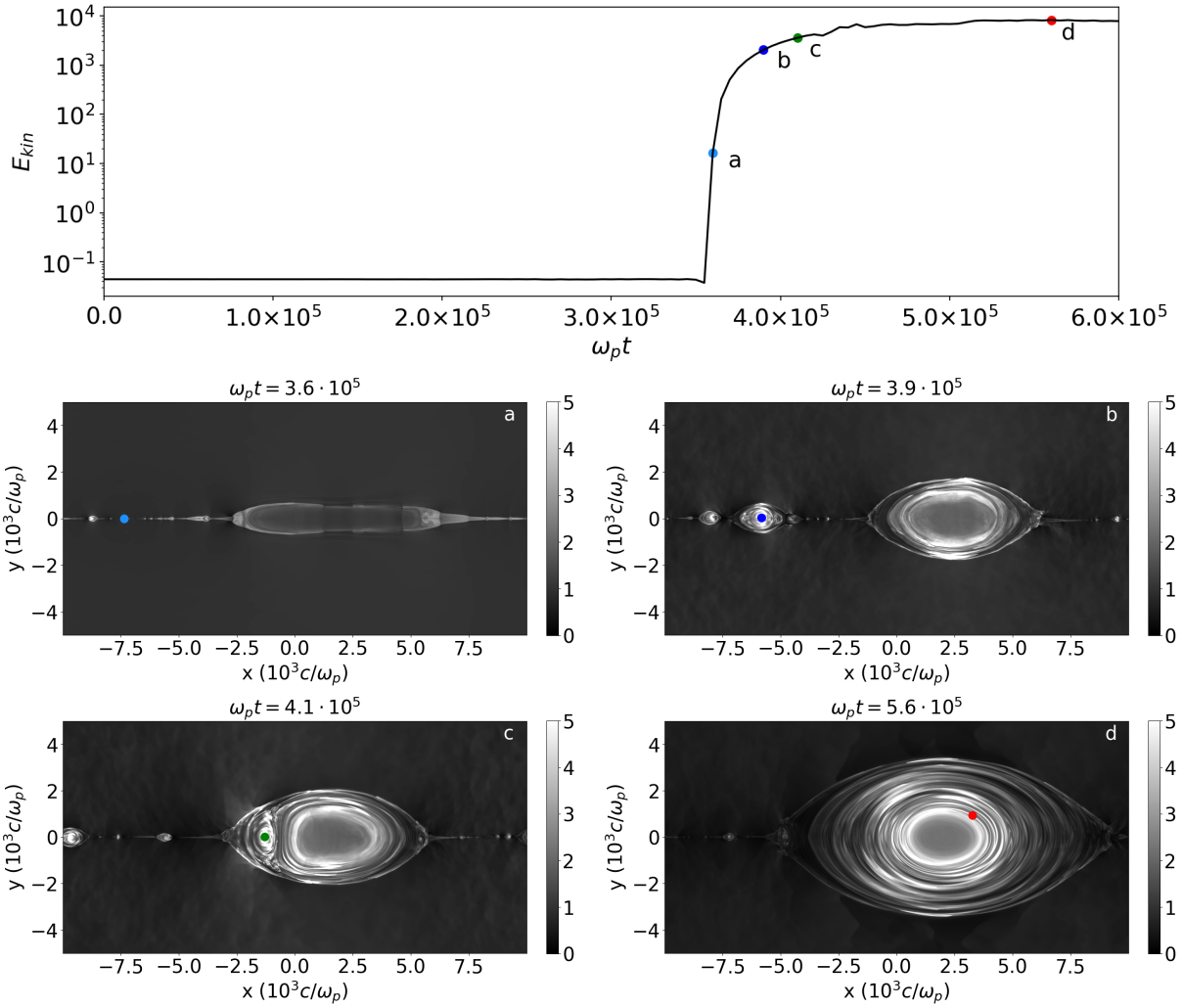

Figure 4.7: *Top panel*: Evolution over time of the kinetic energy of the most energetic particle, where the points represent the four instants of time corresponding to the plots in the lower panels. *Middle and bottom panels*: Overplot of the position of the most energetic particle, colored according to its Lorentz γ-factor, on the plasma density (colorbar) snapshots in four main moments of its evolution, obtained with a grid resolution $N_x = 3072$ and $\bar{S} = 10^4$.

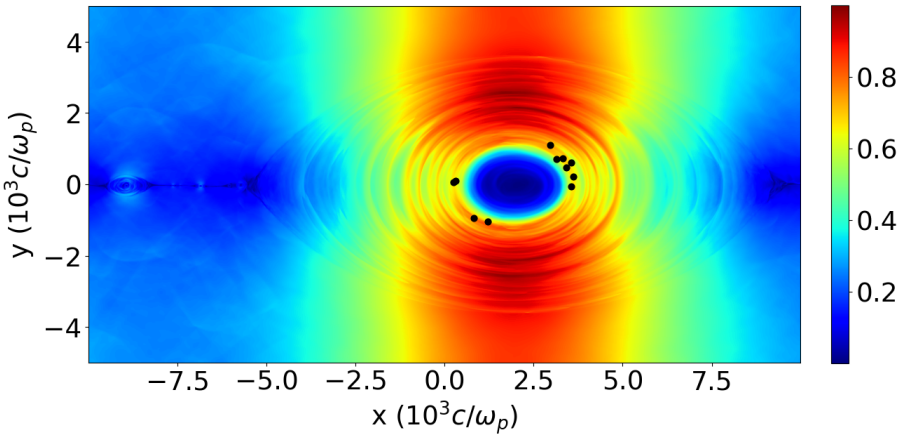

Figure 4.8: Position of the most energetic particles on the snapshot of the magnetic field module, normalized to its maximum value, at the end of the simulation obtained with a grid resolution $N_x = 3072$ and $\bar{S} = 10^4$.

4.2.2 Dependence on grid resolution and numerical method

The impact of grid resolution and physical resistivity on the particle energy distribution is now assessed.

A comparison between particles energy spectra at the end of the simulation ($\omega_p t \approx 6 \cdot 10^5$) at different resolutions is shown in Figure 4.10, in the resistive ($\bar{S} = 10^4$; left-hand panels) and ideal ($\bar{S} = \infty$; right-hand panels) simulation cases, for the most and least diffusive numerical schemes, HLL (lower panels) and HLLD (upper panels), respectively. Table 4.2 shows the corresponding spectral index p of the power-law part of the spectrum.

In the presence of a physical resistivity (see left-hand panels), the spectrum remains almost unchanged once $N_x \gtrsim 768$ ($a/\Delta x \simeq 10$), and it quickly converges to a power-law with index $1.7 \lesssim p \lesssim 1.8$ for both numerical methods, as shown in the first two columns of Table 4.2. This indicates that once the tearing instability is triggered and the reconnection cascade commences, the acceleration properties are virtually independent of the numerical resolution and numerical diffusion.

However, if an ideal plasma is considered (see right-hand panels), the results differ depending on the chosen numerical method. For the HLLD scheme, which has the least dissipation, the tearing instability is gradually quenched (as already discussed in Section 4.1.2) as the resolution increases and no significant particle acceleration takes place so that the particle energy distribution remains close to the initial Maxwellian (see top right panel of Figure 4.10). Conversely, the presence of a larger numerical diffu-

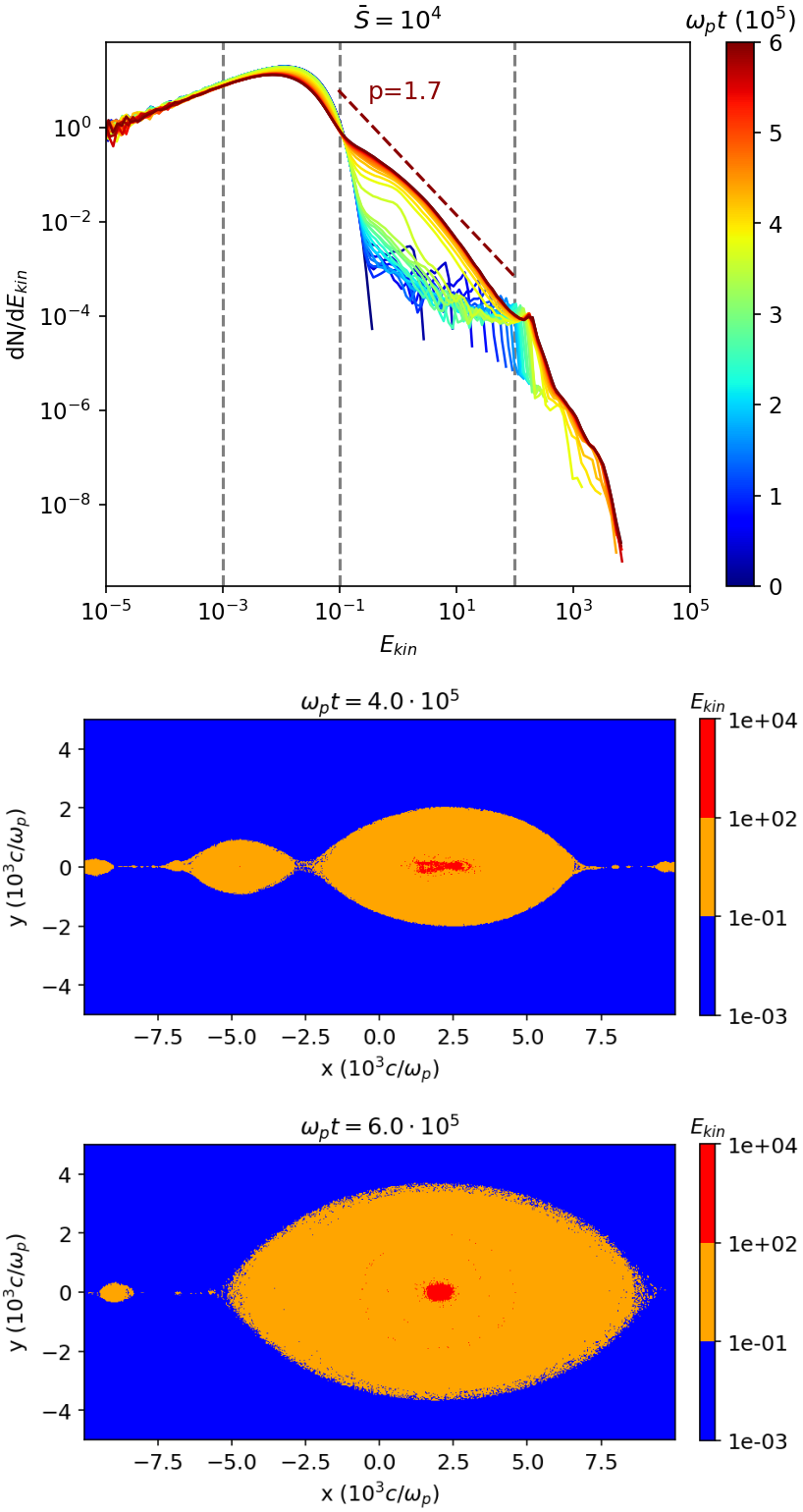

Figure 4.9: *Top panel*: temporal (colorbar) evolution of particles energy spectrum and the p-index of the power law to which it converges (red dashed line). *Middle and bottom panel*: Spatial distribution of the particles, colored according to their energy (colorbar), at two different instants of time. The energy ranges of the colorbar correspond to the three different parts of the spectra shown in the top panel. The graphs are obtained with a grid resolution $N_x = 3072$ and with $\bar{S} = 10^4$.

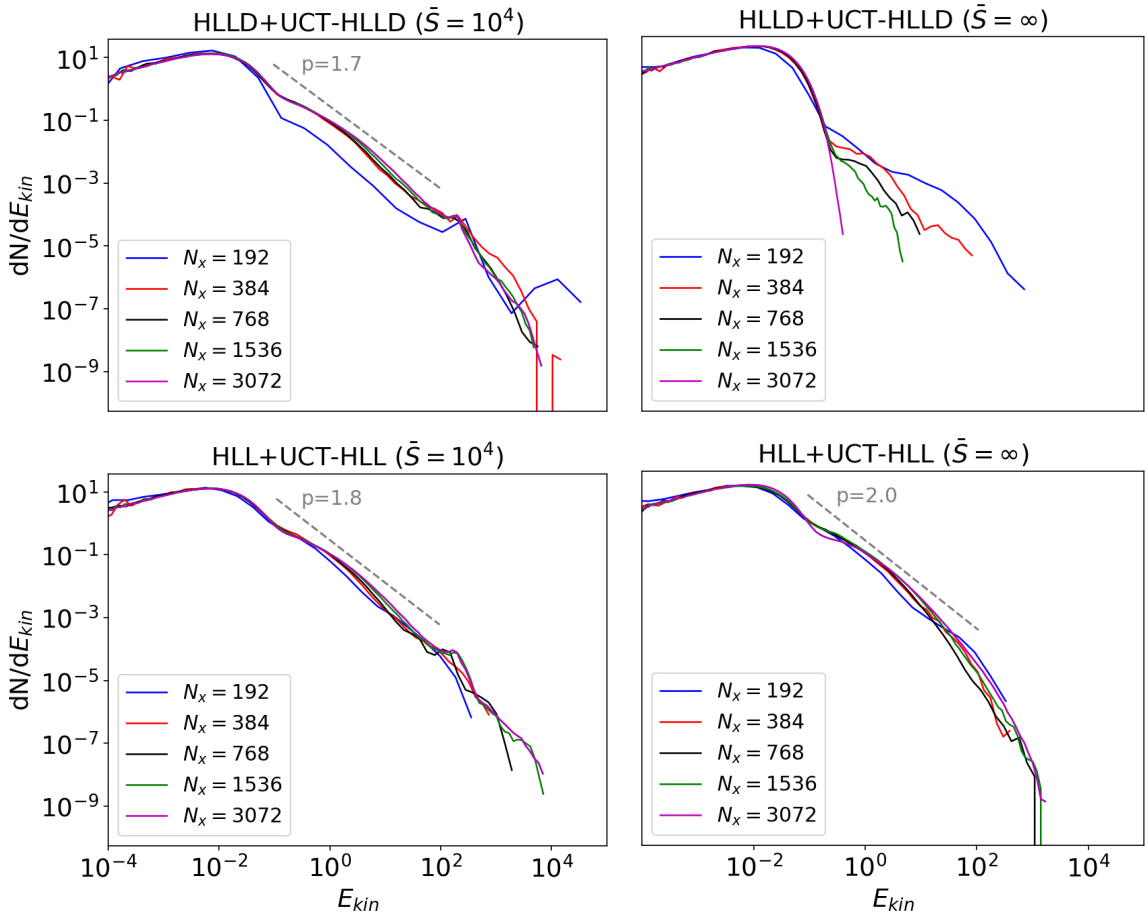

Figure 4.10: Comparison of particle energy spectra at the end of the simulation ($\omega_p t = 6 \cdot 10^5$) for different grid resolutions in the case of a resistive with $\bar{S} = 10^4$ (left panels) and an ideal (right panels) plasma. The HLLD (+ UCT-HLLD) scheme is used in the upper panels, with the HLL (+ UCT-HLL) one being used in the lower panels. The dashed gray lines represent the power law to which the spectra converge, with the corresponding p-index. In all the cases the WENO-Z reconstruction has been used.

sion in the HLL scheme, triggers magnetic reconnection even in the ideal limit, thus spawning a spectral distribution with power-law index $p \approx 2.0$ (see the last column of Table 4.2). In this case, fluid convergence (in the sense discussed in Section 4.1.2) could not be achieved (see Figure 4.3) While the spectral index obtained in the ideal case is not significantly different from the resistive case, our results indicate that the outcome of ideal MHD computations should be interpreted with some caution as the mechanisms triggering resistive instabilities may be driven in a rather unpredictable way by numerical diffusion rather than by actual physical effects. This conclusion may differ if we consider the case of fast reconnection driven by turbulence.

Table 4.2: p-index of the power-law part of the spectra (referring to Fig. 4.10) at different resolutions for different combinations of schemes in the case of resistive ($\bar{S} = 10^4$) and ideal ($\bar{S} = \infty$) plasma. The ideal HLLD+UCT-HLLD case is not shown as magnetic reconnection does not start.

Resolution	$a/\Delta x$	Power-law index p		
		HLLD ($\bar{S} = 10^4$)	HLL ($\bar{S} = 10^4$)	HLL ($\bar{S} = \infty$)
192×96	~ 2.5	1.5	1.3	1.5
384×192	~ 5	1.6	1.7	2.2
768×384	~ 10	1.7	1.8	2.4
1536×768	~ 20	1.7	1.8	2.2
3072×1536	~ 40	1.7	1.8	2.0

4.2.3 Spectral distribution versus Lundquist number

The resolution study is repeated by varying the value of the redefined Lundquist number $\bar{S}$. Figure 4.11 shows a comparison between the particle energy spectra during the saturation phase, for different values of $\bar{S}$ and grid resolutions. As shown in Figure 4.5, the beginning of the saturation phase is delayed as $\bar{S}$ increases, for this reason the spectra shown in Figure 4.11 correspond to different computational times. Also, for higher value of the Lundquist number ($\bar{S} = 10^5$) the results from low-resolution simulation ($N_x = 192$, i.e., $a/\Delta x \simeq 2.5$) are omitted, since, as mentioned in Section 4.1.3, magnetic reconnection at that time has just started.
From Figure 4.11 it appears that the power-law index weakly depends on the Lundquist number and it converges to a value $1.5 \lesssim p \lesssim 1.7$ again for grid resolutions at around $N_x \gtrsim 768$ ($a/\Delta x \simeq 10$). A quantitative measure of the p-index is provided, for different values of $\bar{S}$, in Table 4.3 at the largest grid resolution ($N_x = 3072$, i.e., $a/\Delta x \simeq 40$). Note that it remains substantially the same for $\bar{S} \gtrsim 10^4$ (or $S \gtrsim 8 \cdot 10^5$), that is a result that may be connected to the onset of the fast reconnection regime (see Landi et al., 2015).
These results lead to the conclusion that, once magnetic reconnection has started, the amount of resistivity, either of numerical or physical origin, has a weak (or almost negligible) impact on the particle energization process.
These findings favorably compare to previous works using test-particles in MHD snapshots, in particular with Gordovskyy et al. (2010a,b), who found a power-law index $p \approx 1.5 - 3.0$ at the end of reconnection (i.e., the O-point stage). In addition, PIC simulations of merging plasmoids reveal

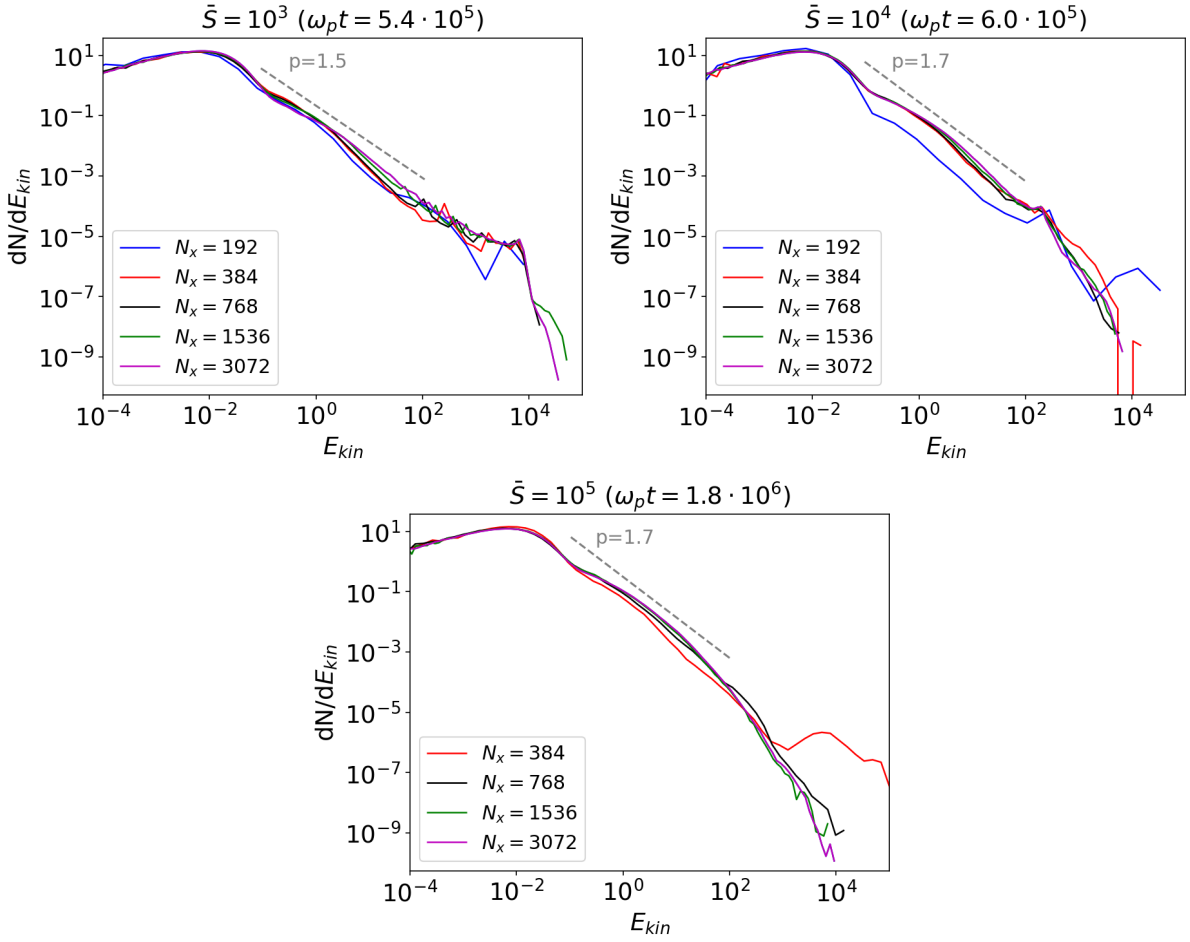

Figure 4.11: Comparison of particle energy spectra in the saturation phase at different $\bar{S}$ for several grid resolutions, obtained using the HLLD+UCT-HLLD with the WENO-Z scheme.

a spectral index compatible with these results, that is $p \approx 1.5$ (see, for instance, Drake et al., 2010, 2013; de Gouveia Dal Pino and Kowal, 2015).

Table 4.3: p-index of the power-law part of the spectra (referring to Fig. 4.11) at at the highest grid resolution ($N_x = 3072$) for different values of $\bar{S}$.

		Power-law index p			
Resolution	$a/\Delta x$	$\bar{S} = 10^3$	$\bar{S} = 10^4$	$\bar{S} = 10^5$	$\bar{S} = \infty$
3072×1536	~ 40	1.5	1.7	1.7	-

5

The importance of the resistive electric field

This chapter is based on the paper published on the *Monthly Notices of the Royal Astronomical Society* by Eleonora Puzzoni, Andrea Mignone, and Gianluigi Bodo, titled: The impact of resistive electric fields on particle acceleration in reconnection layers (Puzzoni et al., 2022). The author of this thesis carried out all the simulations, created all the figures, and mostly discussed and interpreted the data presented in this chapter.

This chapter is intended to be part of the ongoing debate on the importance of the resistive term of the electric field compared to the convective one in the context of particle acceleration in high-energy astrophysical environments featuring magnetic reconnection. Indeed, this chapter investigates whether the resistive field plays a role in accelerating particles to high energies.

5.1 2D Histogram analysis

A detailed analysis of the resistive contribution is provided by the histograms in Figure 5.1 at the $N_x = 1536, 3072$, and 6144 grid zones for the $\bar{S} = 10^4$ case. The 2D histograms show the percentage of energy gained by particles due to the resistive electric field at the end of the computational time ($\omega_p t = 7.8 \cdot 10^5$), as a function of their final kinetic energy. Notice that a steady state (i.e, the saturation phase) is reached at this time. The colors indicate the fraction of particles ($f_{\rm part}$) in each energy bin, normalized to the total number of particles in that bin ($N_{\rm part}$), in turn, reported in the corresponding uppermost panels.

As an illustrative example, it is worth looking at the first gray pixel in the first energy bin (lower left corner of the figure) of the upper right-handed 2D histogram of Figure 5.1. 50% of particles in this energy bin ($N_{\rm part} \approx$

10^5, from the corresponding upper panel) is energized between $0-5\%$ by the resistive field. The corresponding 2D histogram for the convective contribution would be mirrored with respect to the x-axis. Therefore, 50% of particles in the example bin are energized between $95-100\%$ by the convective electric field.
By looking at Figure 5.1, the 2D histograms at different grid resolutions show a similar shape. The resistive electric field has a small contribution ($W_r \lesssim 30\%$) at low energies ($E_{\rm kin} \lesssim 10\ v_A^2$). On the contrary, it has a non-negligible contribution at intermediate energies ($10 \lesssim E_{\rm kin}/v_A^2 \lesssim 10^3$). Indeed, up to about 30% of particles are energized up to 100% by the resistive field (see the purple, blue and green pixels). At high energies ($E_{\rm kin} \gtrsim 10^3\ v_A^2$), the resistive contribution slightly decreases with the grid resolution, but still leaves the corresponding energy gain significant. Indeed, even in the high-resolution case (see lower panel), for about 40% of the particles in the last energy bin, the resistive contribution accounts for $40-45\%$ of their energy gain (see orange pixel). A smaller percentage of particles ($\lesssim 10\%$) are accelerated up to 100% by the resistive field (see purple pixels in the upper right corner). At lower resolution (see upper left-hand panel), owing to increased numerical diffusion, the amount of work exerted by the resistive electric field is somewhat larger at high-energies ($W_r \gtrsim 50\%$, purple, blue, and green pixels).
Our simulation results indicate that the contribution of the resistive electric field converges with grid resolution at intermediate energies ($10 \lesssim E_{\rm kin}/v_A^2 \lesssim 10^3$). At high energies ($E_{\rm kin} \gtrsim 10^3\ v_A^2$), however, convergence assessment is somewhat more uncertain, as the contribution of the resistive field appears to decrease as resolution increases. Further details on plasma convergence are presented in Appendix B, where we conclude that it was not possible - with the current computational resources - to resolve the typical critical current sheet (i.e., the smallest current layer found in the system; see Uzdensky et al., 2010). Nevertheless, the resistive contribution is non-negligible at all resolutions. Indeed, in the following sections, we will assess its fundamental importance in the particle acceleration mechanism.

5.2 Resistive field role on high-energy particles

Figure 5.2 shows the 1D histograms of the particles kinetic energy at the end of the computational time ($\omega_p t = 7.8 \cdot 10^5$) for $\bar{S} = 10^4$ at different grid

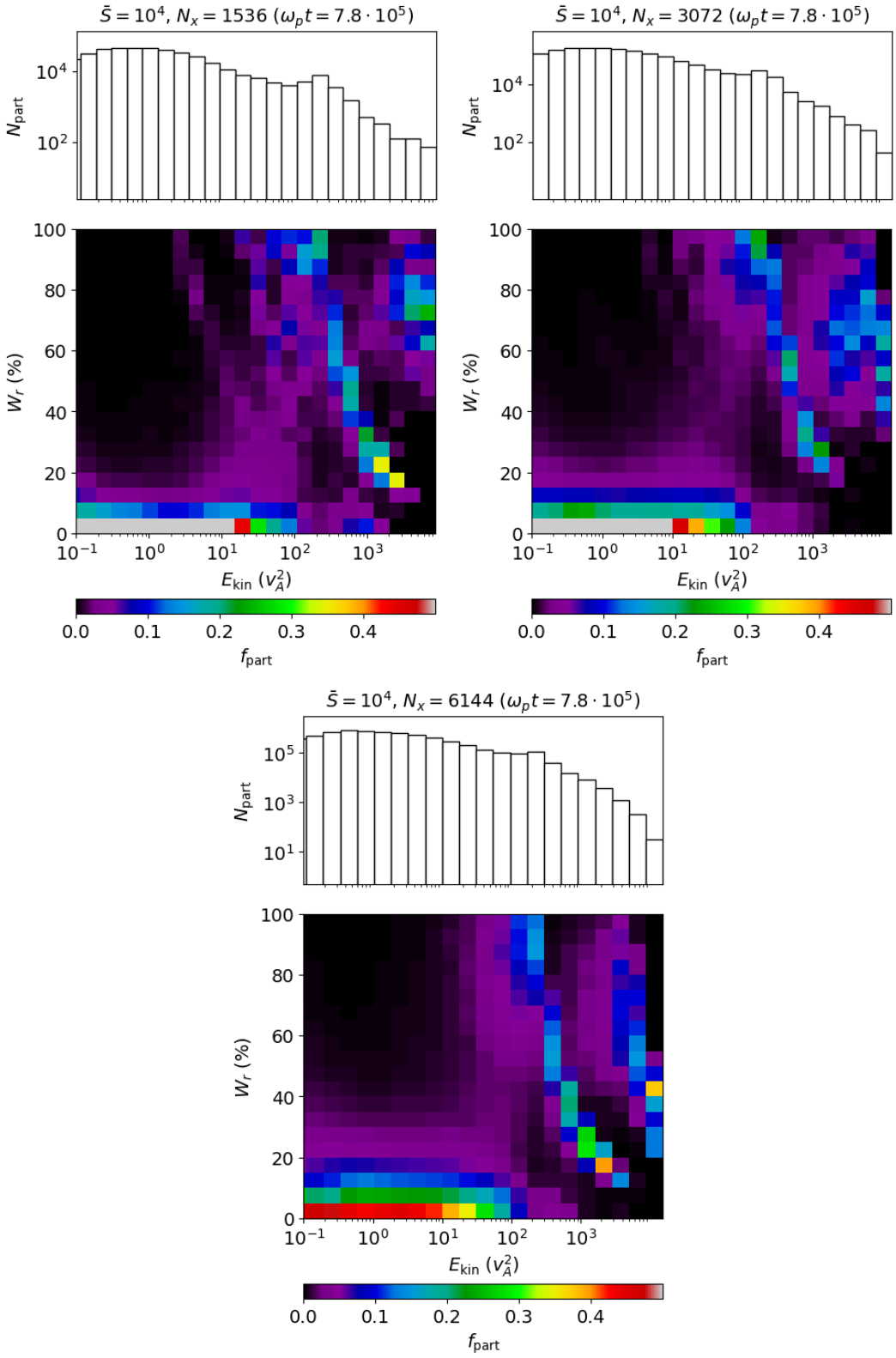

Figure 5.1: 2D histograms of the energy gained (%) due to the resistive electric field by particles as functions of their final kinetic energy. The colorbar represents the fraction of particles in each energy bin. The total number of particles in each bin is shown in the corresponding upper panels. These histograms are reproduced at the $N_x = 1536$ (upper left panel), $N_x = 3072$ (upper right panel) and $N_x = 6144$ (lower panel) grid resolutions, with $\bar{S} = 10^4$.

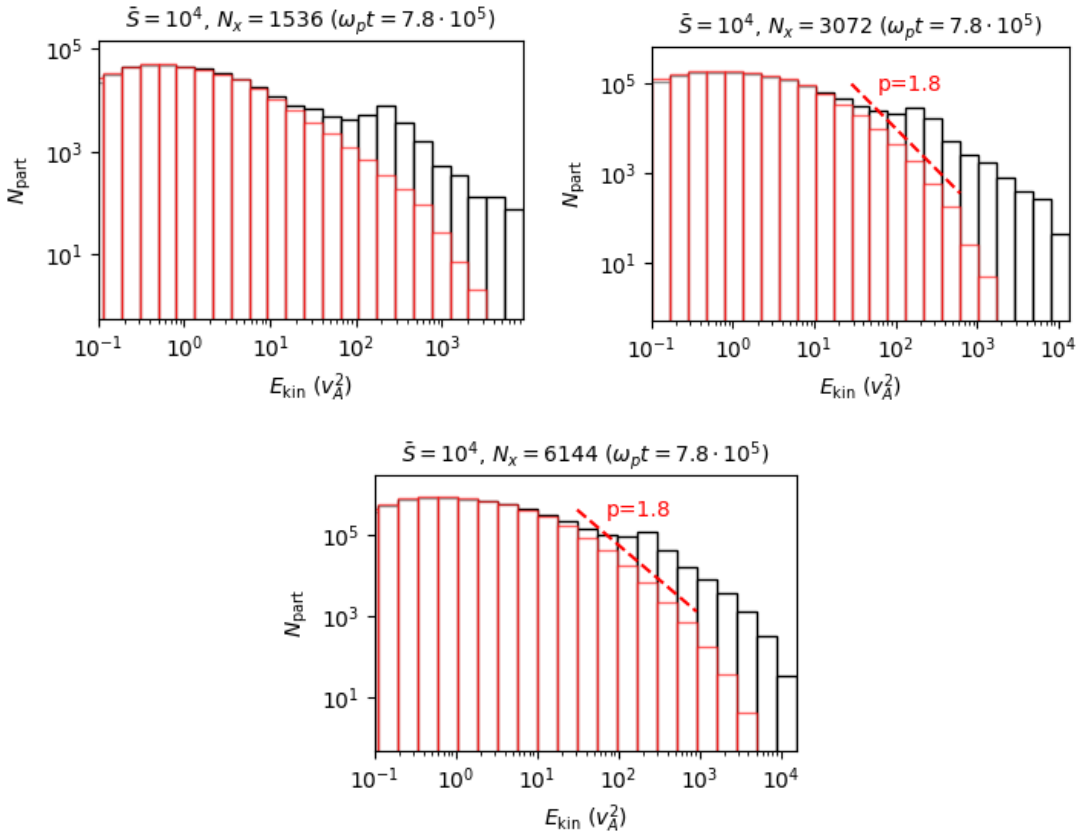

Figure 5.2: Histograms of the particles kinetic energy at the end of the computational time for $\bar{S} = 10^4$ at different grid resolutions, obtained with (black bars) and without (red bars) the resistive term in the particle equations of motion. The dashed red lines represent the power-law part of the spectra, with the corresponding p-index.

resolutions ($N_x = 1536, 3072, 6144$). The black and red bars are obtained, respectively, by including or excluding the resistive term in the particle equations of motion. Following the work of Sironi (2022), we have decided to remove all the particles that are initially found within the current sheet ($|y_0/a| < 1$) as they have peculiar behavior depending on the initial conditions. Moreover, we removed the particles initially farthest from the current sheet ($|y_0/a| > 16$), as they will never reach it within the final simulation time. This avoids a box size effect or a statistic bias. A direct comparison between the two cases clearly indicates that, when the resistive contribution is neglected, the particle spectra are somewhat steeper, characterized by a power-law with index $p \approx 1.8$ at the largest resolutions ($N_x = 3072, 6144$), and the maximum kinetic energy achieved by the particles is lower. This discrepancy occurs at all resolutions considered here. For instance, in the $N_x = 3072$ case, the maximum kinetic energy achieved by particles by considering the resistive term is $E_{\rm kin} \approx 1.3 \cdot 10^4\ v_A^2$, versus the maximum kinetic energy $E_{\rm kin} \approx 1.4 \cdot 10^3\ v_A^2$ achieved without including this term. Similarly, in the $N_x = 6144$ case, the maximum kinetic energy reached by particles is lower when the resistive term is neglected ($E_{\rm kin} \approx 4.2 \cdot 10^3\ v_A^2$ versus $E_{\rm kin} \approx 1.6 \cdot 10^4\ v_A^2$). This confirms, as also argued by Sironi (2022), that the resistive electric field contribution is fundamental in building the high-energy tail. As we shall see shortly, this effect takes place in the early stages of the acceleration process.

To this end, we now focus on the resistive contribution in accelerating particles over time and consider only those particles that at the end of the computational time achieved a kinetic energy $E_{\rm kin} > E_{\rm thr}$. We set three different energy threshold: $E_{\rm thr}/v_A^2 = 10^3, 5 \cdot 10^3, 10^4$. For these particles we calculated the fraction of energy gained due to the resistive contribution, namely $\sum_p W_{\rm r,p}/W_{\rm tot}$, where $W_{\rm tot} = \sum_p W_{\rm r,p} + \sum_p W_{\rm c,p}$ is the total energy gained by these particles (i.e., also due to the convective contribution). Figure 5.3 shows the fractional energy gain of selected particles due to the action of the resistive field as a function of time, for different energy thresholds and for $\bar{S} = 10^4$ with a grid resolution $N_x = 3072$ (left panel) and $N_x = 6144$ (right panel). By looking at this figure, it is clear that the resistive contribution is dominant in accelerating particles at $3.6 \cdot 10^5 \lesssim \omega_p t \lesssim 4.4 \cdot 10^5$ for all the kinetic energy thresholds. Subsequently, the resistive contribution gradually decreases. In the $N_x = 6144$ case (see right panel), the resistive contribution towards the end of computational

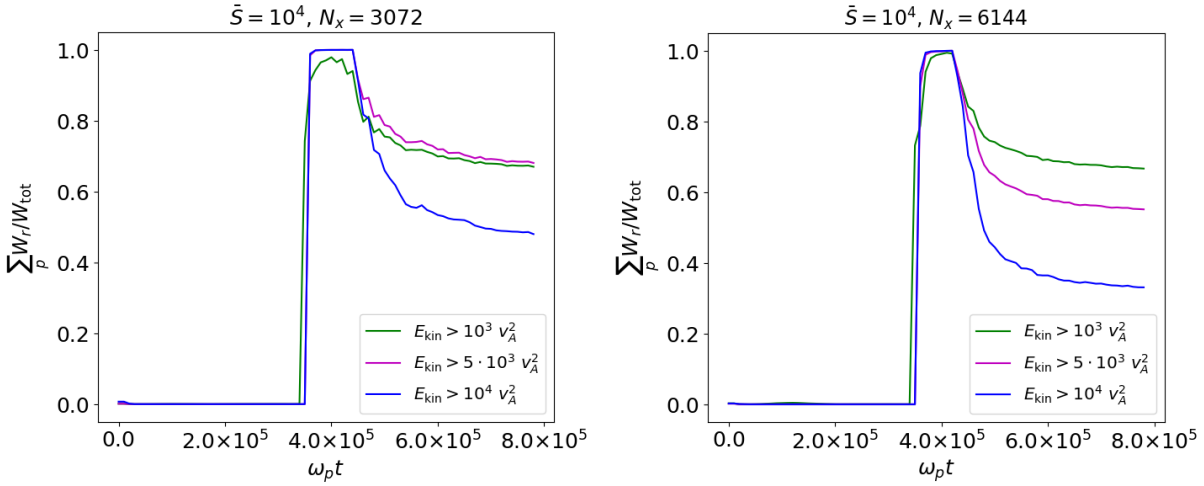

Figure 5.3: *Left panel*: Resistive contribution over time on particles that at the end of the computational time reach a kinetic energy of $10^3\ v_A^2$ (green line), $5 \cdot 10^3\ v_A^2$ (magenta line), and $10^4\ v_A^2$ (blue line) for the $\bar{S} = 10^4$ case with a grid resolution $N_x = 3072$. *Right panel*: Same but for $N_x = 6144$.

time is lower (see $E_{\rm kin} > 5 \cdot 10^3\ v_A^2$ and $E_{\rm kin} > 10^4\ v_A^2$). This result is in agreement with the decline at high-energies observed in the lower panel of Figure 5.1. Accordingly, if the resistive contribution is removed from the particle equations of motion, particles cannot achieve the same high energies.

5.3 Relation between particle energization and current sheet evolution

Figure 5.4 shows the fluid pressure colored maps at four specific times. These instants are marked with red points in corresponding lower panels, where we show the resistive field contribution for the particles with final kinetic energies above $E_{\rm thr} = 10^3\ v_A^2$. By looking at the upper left panels ($\omega_p t = 3.4 \cdot 10^5$), it is clear that the current sheet has reached the 2$^{\rm nd}$-linear phase. At subsequent times ($\omega_p t = 3.6 \cdot 10^5$, for instance), the current sheet fragments in X- and O-points (see upper right panel). This fragmentation phase corresponds to a net increase of the resistive electric field contribution in the particle acceleration mechanism (see corresponding lower panel). The increase of the resistive contribution during the fragmentation phase may be explained by the formation of X-points, in which the resistive electric field is strong. During the fragmentation phase, plasmoids merge

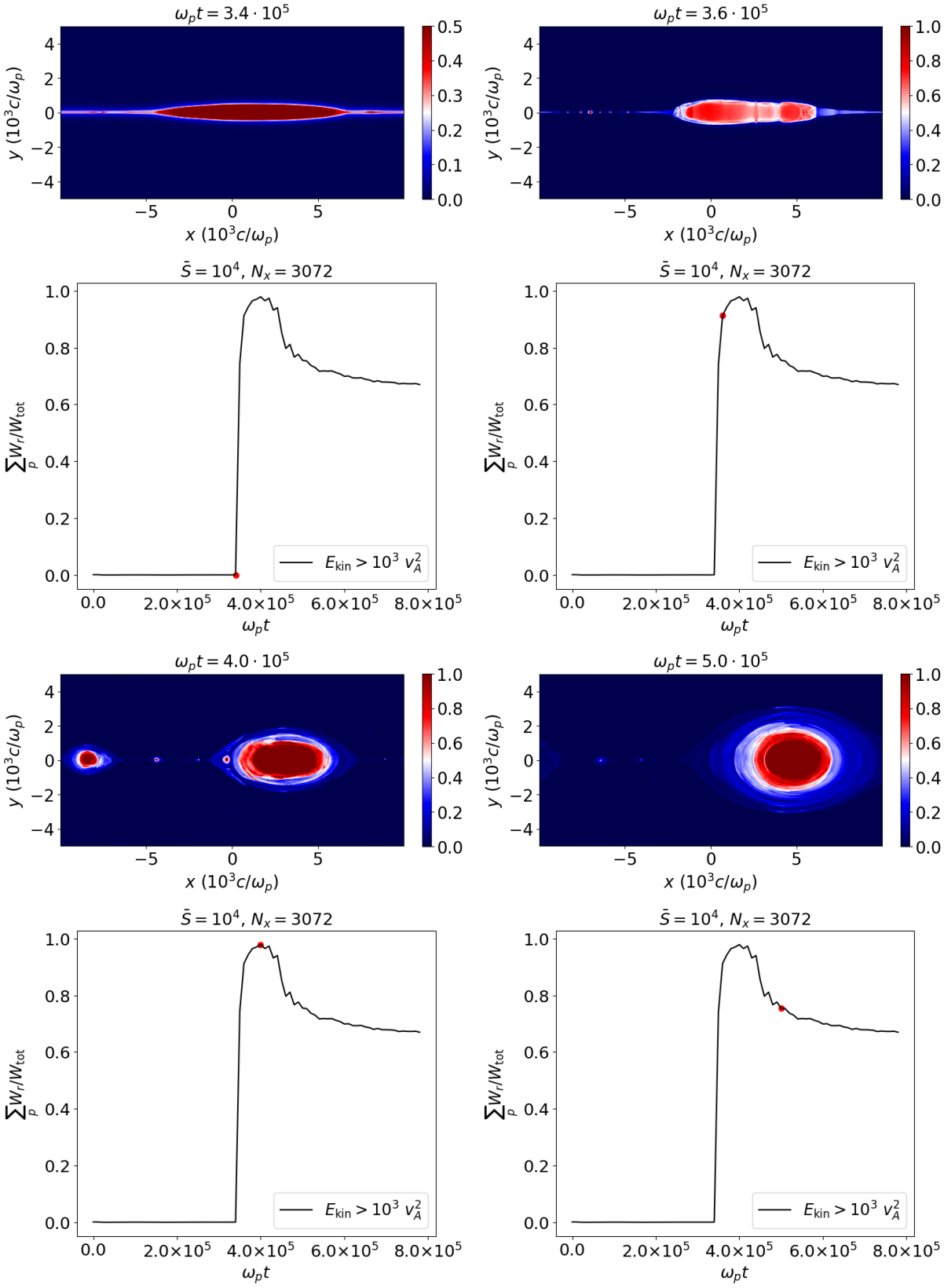

Figure 5.4: Resistive field contribution on the most energetic particles ($E_{\rm kin} > 10^3\ v_A^2$) over time, obtained with $\bar{S} = 10^4$ and a grid resolution $N_x = 3072$. This plot is repeated four times being marked with red points, that characterized four evolutionary phases of the current sheet, whose pressure is shown in the corresponding upper panels.

with each other and during this merging process the resistive contribution remains strong, reaching a peak at $\omega_p t = 4.0 \cdot 10^5$ (see lower left panels). Indeed, when two plasmoids merge, a secondary current sheet forms at the interface between the two (see, e.g., Oka et al., 2010; Sironi and Spitkovsky, 2014; Nalewajko et al., 2015). Plasmoids merge until a large final magnetic island is formed. When major mergers no longer occur and the final giant plasmoid stabilizes (i.e, the saturation phase is reached), the resistive field contribution begins to smoothly decrease (see lower right panels). Indeed, towards the end of the computational time, the resistive contribution seems to approach a saturation value.
Therefore, high-energy particles are accelerated by the resistive electric field when they cross an X-point (and are shortly after injected into a plasmoid, see, e.g., Zenitani and Hoshino, 2001; Bessho and Bhattacharjee, 2007; Lyubarsky and Liverts, 2008; Sironi and Spitkovsky, 2014; Ball et al., 2019) and during islands merging. When particles are finally trapped inside a plasmoid that no longer merges with other islands, the resistive contribution decreases, leaving room for the more gradual action of the convective electric field. These results are in agreement with those of Sironi (2022), who demonstrated that high-energy particles must have crossed non-ideal regions during the early stages (called "injection" by the author) of their acceleration process. On the contrary, our results are in contrast with those of Guo et al. (2019), who claim that the non-ideal field can be neglected in the particle acceleration mechanism, as the Fermi mechanism is the dominant one. Similarly, our results are different from those of Kowal et al. (2011, 2012) (see also de Gouveia Dal Pino and Kowal, 2015; del Valle et al., 2016; Medina-Torrejón et al., 2021), who argue that the resistive contribution is completely negligible in the particle acceleration mechanism.

6

Conclusions and outlooks

In this thesis, we investigated particle acceleration in magnetized current sheets with a particular emphasis on the impact of the numerical and physical resistivity on magnetic reconnection and particle acceleration mechanisms. To this end, we have presented high-resolution 2D numerical simulations of tearing-unstable MHD current sheet embedding a non-thermal population of test particles evolving along with the fluid. Computations have been performed using the PLUTO code for computational plasma astrophysics.
In this chapter, the major results presented in the previous chapters of this thesis are summarized. Moreover, possible future developments are briefly discussed.

6.1 Summary

In Chapter 4, we have investigated the impact of the numerical method, grid resolution, and physical resistivity on both the current sheet evolution and its convergence properties as well as on the spectral properties of non-thermal test-particles evolving within the background thermal plasma.
We initially focused only on the fluid evolution, identifying four main temporal phases characterized by a growing number of newly forming X-points. After an initial 1^{st}-linear phase characterized by a shrinking of the initial current sheet ($t/\bar{\tau}_A \lesssim 840$, where $\bar{\tau}_A = a/v_A = 250/\omega_p$), a 2^{nd}-linear phase (ending at $t/\bar{\tau}_A \approx 1360$) marks the evolution of smaller current sheets, resulting from the breaking of the initial one. Subsequently, a more rapid fragmentation phase leads to the appearance of several X- and O-points feeding the formation of dynamically interacting plasmoids ($t/\bar{\tau}_A \lesssim 1840$). In the end, a final non-linear saturated phase is accompanied by the presence of a single large magnetic island.
Several simulations using different numerical methods and mesh resolu-

tions have demonstrated that convergence during the initial linear stages of the evolution can be achieved only for finite values of the Lundquist number $\bar{S} = av_A/\eta$, where a, v_A, and η are, respectively, the initial current sheet width, Alfvén velocity, and physical resistivity. The minimum resolution at which convergence is attained depends on the amount of numerical diffusion inherited from the underlying discretization method. Below this resolution, the linear growth phase is dominated by spurious numerical effects, which, as a general trend, are likely to delay the onset of the tearing instability as the resolution becomes coarser. In this respect, we have found that the combination of the HLLD Riemann solver and the UCT-HLLD emf averaging scheme of Mignone and Del Zanna (2021), together with 5^{th}-order WENO-Z reconstruction, yields the best performance achieving convergence already at $a/\Delta x \simeq 10$ when $\bar{S} = 10^4$. This is about half the grid resolution when compared to either linear reconstruction or more diffusive numerical methods based on more approximate Riemann solvers (e.g., HLL; see Del Zanna et al., 2007, and reference therein) or 2^{nd}-order emf averaging schemes (e.g., CT-Contact; see Gardiner and Stone, 2005) for which convergence is ensured when $a/\Delta x \gtrsim 20$.

For larger (smaller) values of the Lundquist number, the mesh size has to be increased (decreased) at the point where numerical diffusion falls below the physical one. For a globally 2^{nd}-order accurate scheme, we have shown that this is expected to hold if the number of computational zones covering the initial current sheet width scales approximately as $a/\Delta x \sim 10\sqrt{\bar{S}/10^4}$. We also have verified that the linear growth rate matches the theoretical prediction for asymptotically large $\bar{S}$. Conversely, in the ideal case ($\bar{S} = \infty$), we have observed that the discretization scheme introduces a grid-dependent numerical resistivity that still allows the current sheet to reconnect, although convergence can never be actually achieved. This is easily explained by the fact that a change in grid resolution is tantamount to a different problem with another value of the (spurious) resistivity. Only with the employment of the HLLD + UCT-HLLD scheme, the system remains stable as one would expect for an ideal current sheet. Based on these results, we have picked the HLLD scheme (with 5^{th}-order WENO-Z spatial reconstruction) as our optimal numerical method. This suggests that genuinely higher than 2^{nd}-order schemes may be more suited for this kind of problems.

In the second part of Chapter 4, we focused on the effect of the numerical

method and resistivity on particle acceleration and energization. Several computations at different grid resolutions indicate that the particle energy distribution remains almost unchanged for $a/\Delta x \gtrsim 10$ and it quickly converges to a power-law with index $p \approx 1.7$, when $\bar{S} \geq 10^4$. Different values of the Lundquist number, in fact, appear to have a weak influence on the power-law index, once the fast reconnection regime ($\bar{S} \geq 10^4$) has been reached. These results do not generally depend on the integration method or its numerical diffusion but seem to have a general validity inasmuch as the magnetic reconnection process is operating. Indeed, we have found that this holds even for ideal MHD ($\bar{S} = \infty$, albeit with a different spectral index) for which the island formation process, when present, could be triggered solely by numerical resistivity. This has been clearly observed in the presence of a more dissipative scheme such as the HLL Riemann solver (for which $p \approx 2$), but it does not appear with the more accurate HLLD Riemann solver/emf averaging combination.

Our conclusion is that, in the context of reconnection-driven test-particle acceleration, there is no need to reach very high grid resolutions and that the amount of resistivity, beyond a certain threshold (i.e., $\bar{S} \geq 10^4$), has a very weak or almost negligible impact on the particle energization process. It must be emphasized that in this chapter we have investigated convergence by concentrating on the particle spectra.

More subtle aspects, not captured by the convergence in the spectrum, have been addressed in Chapter 5, where we shift our focus on the convergence properties of the *resistive* field, by investigating its behaviour in the process of particle acceleration in a reconnecting 2D Harris current sheet at different grid resolutions.

Our results indicate clear convergence at intermediate energies ($10 \lesssim E_{\rm kin}/v_A^2 \lesssim 10^3$), while at high energies ($E_{\rm kin} \gtrsim 10^3\ v_A^2$) convergence achievement is not clear-cut. However, even if the contribution of the resistive field slightly decreases with grid resolution (at high energies), a more detailed analysis reveals that its omission from the particle equations of motion leads to lower (within a factor of 10) maximum energies and steeper cuts ($p \approx 1.8$ at the largest resolutions) in the particle energy spectra. This behavior remains essentially unaffected by grid resolution.

We found that the resistive contribution is strongest as the current sheet starts to fragment and plasmoids start to merge. During this phase, in fact, the resistive contribution sharply increases as a large number of X-

points is created (where the resistive electric field is predominant). The presence of X-points is indeed essential in producing abrupt acceleration of particles at this stage (see, e.g., Zenitani and Hoshino, 2001; Bessho and Bhattacharjee, 2007; Lyubarsky and Liverts, 2008; Sironi and Spitkovsky, 2014; Nalewajko et al., 2015; Ball et al., 2019). Moreover, particle energy is boosted also during plasmoids merging, due to the anti-reconnection electric field therein (see, e.g., Oka et al., 2010; Sironi and Spitkovsky, 2014; Nalewajko et al., 2015).
Our results lead us to conclude that not only the resistive field is non-negligible (in agreement with the works, for example, of Onofri et al., 2006; Zhou et al., 2016; Ball et al., 2019; Sironi, 2022), but it plays a fundamental role in accelerating high-energy particles. In particular, our results favorably agree with Sironi (2022), who argues that the non-ideal field is crucial in the early-stages of particle acceleration. On the other hand, our outcomes disagree with those of Kowal et al. (2011, 2012), de Gouveia Dal Pino and Kowal (2015), del Valle et al. (2016) and Medina-Torrejón et al. (2021), who neglect the resistive electric field in the particle equations of motion as they do not consider it important in the acceleration process. Similarly, our results also differ from those of Guo et al. (2019), who argue that the Fermi mechanism is dominant and the non-ideal field can be neglected in the particle acceleration process during large-scale reconnection events, as it is unimportant for the formation of the power-law distribution.

6.2 Outlooks

In addition to the results discussed in this thesis, there are still several numerical and physical aspects that need further investigation.

- First of all, it is essential to extend this work to the relativistic (fluid) case (RMHD), as relativistic outflows appear in GRBs and AGNs. Moreover, a more precise comparison could be made with the works on particle acceleration by magnetic reconnection, which considers relativistic fluids (see, e.g. Sironi and Spitkovsky, 2014; Guo et al., 2015; Ripperda et al., 2019a).
- At the same time, the impact of the guide field (null in this thesis work) should be considered, as it is still a matter of debate (see, e.g., Drake et al., 2010; Kowal et al., 2011).
- In many works particles are evolved on a static background magnetic

configuration (i.e, a fluid snapshot; see, e.g., Gordovskyy et al., 2010a; Kowal et al., 2011; de Gouveia Dal Pino and Kowal, 2015; Ripperda et al., 2017a). Analyzing this case would allow us to understand if the contemporary evolution of the current sheet really affects particle energization.

- The extension to the 3D case would enable us to perform more consistent and realistic simulations. However, achieving convergence requires a high computational cost. Indeed, we explained that the $N_x = 6144$ case included about 80 points on the initial width of our two-dimensional current sheet. In 3D, the number of points would be enormous. Nevertheless, there are advanced numerical techniques, such as adaptive mesh refinement (AMR; see Mignone et al., 2012a) or the guiding center approximation (GCA; see, Ripperda et al., 2018; Mignone et al., 2022), which can be used to reduce computational time.
- As mentioned earlier, future studies will probably take advantage of genuine fourth-order schemes, as well as address the issue of longer simulations and different choices of boundary conditions. Indeed, we have a kind of "artificial" state introduced by periodic boundary conditions. During the non-linear phase, plasmoids merge creating a large final plasmoid, as the process dynamically goes from small scales to large scales. However, when the largest plasmoid is created, the limit imposed by the periodic boundary conditions is reached: there is only one big final plasmoid and then the smallest ones that end up in it. This may not occur when different boundary conditions are considered.

A

X-points number algorithm

The algorithm employed to locate X-points from the simulation results is illustrated.
Since, at an X-point, the magnetic field $|\mathbf{B}|$ vanishes (and so do the B_x and B_y components), we first identify computational zones hosting a local minimum of $|\mathbf{B}|$ over a stencil of 3×3 zones. These zones, therefore, may potentially contain a null point. Let (i, j) be the indices of a zone hosting a local minimum of $|\mathbf{B}|$. A bilinear interpolation is used to represent the B_x and B_y components of magnetic field inside a square delimited by the four corner points $(x_{i\pm1}, y_{j\pm1})$:

$$\begin{aligned} H(\hat{x}, \hat{y}) =& H_{i-1,j-1}(1-\hat{x})(1-\hat{y}) + H_{i+1,j-1}\hat{x}(1-\hat{y}) + \\ &+ H_{i-1,j+1}(1-\hat{x})\hat{y} + H_{i+1,j+1}\hat{x}\hat{y}, \end{aligned} \tag{A.1}$$

where $H(\hat{x}, \hat{y})$ denotes either the x- or y-component of $\mathbf{B}$ while $\hat{x}$ and $\hat{y}$ are normalized coordinates in $[0, 1]$.
Then is required that both $B_x(x, y)$ and $B_y(x, y)$ have a root:

$$\begin{cases} B_x(\hat{x}, \hat{y}) = a_0 + a_1\hat{x} + a_2\hat{y} + a_3\hat{x}\hat{y} = 0, \\ B_y(\hat{x}, \hat{y}) = b_0 + b_1\hat{x} + b_2\hat{y} + b_3\hat{x}\hat{y} = 0, \end{cases} \tag{A.2}$$

where the coefficients $a_0, a_1, ..., b_3$ are readily found from Equation (A.1). Equation (A.2) leads to a quadratic equation whose solutions are considered null points only if they fall inside the unit square.

B

Plasma convergence study

Here we focus on the plasma convergence study, following the methodology adopted in Chapter 4 (see Fig. 4.2). Figure B.1 shows the temporal evolution of the spatially-averaged transverse component of the magnetic field at different grid resolutions (left panel) and the corresponding number of X-points formed (right panel). The number of X-points is obtained through the algorithm based on locating the null points of $|\mathbf{B}|$ discussed in Appendix A.

Although the growth of the perturbation shown in the left panel seems to indicate convergence at $N_x = 3072$ even in the non-linear phase, we cannot conclude the same by looking at the right panel. Indeed, the number of X-points increases with the grid resolution. This leads us to conclude that, during the fragmentation phase, very thin current sheets are created, which are not completely resolved even at these high resolutions. However, as emphasized in Chapter 5, there are strong indications that our results are valid even if we have not achieved complete convergence.

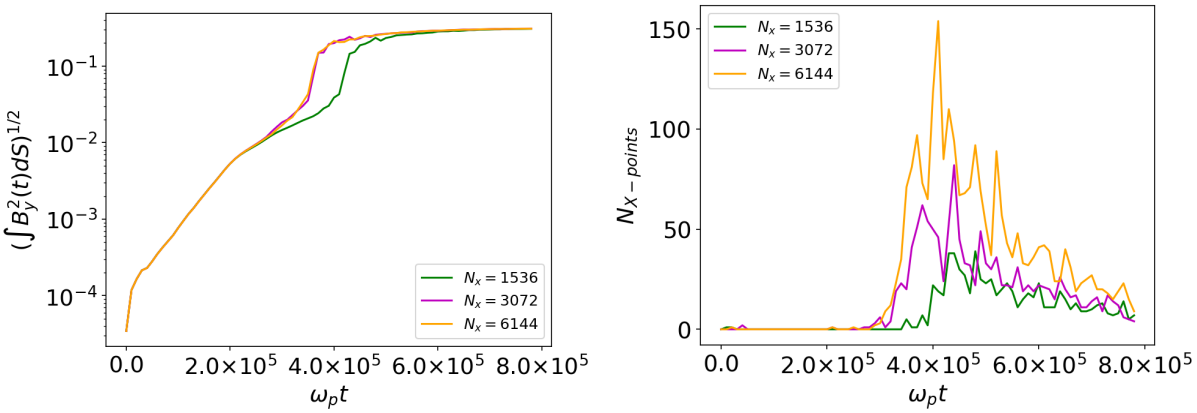

Figure B.1: *Left panel*: Spatially-averaged transverse component of magnetic field as a function of time at different grid resolutions. *Right panel*: Number of X-points formed over time at the same grid resolutions.

Publications list

1. **Puzzoni Eleonora**, Mignone Andrea, Bodo Gianluigi. The impact of resistive electric fields on particle acceleration in reconnection layers, *MNRAS*, 517(1):1452–1459.

2. **Puzzoni Eleonora**, Mignone Andrea, Bodo Gianluigi. On the impact of the numerical method on magnetic reconnection and particle acceleration - I. The MHD case, *MNRAS*, 508(2):2771–2783.

Bibliography

Abdo, A. A., Ackermann, M., and et al., A. Fermi Discovery of Gamma-ray Emission from NGC 1275. *ApJ*, 699(1):31–39, July 2009. doi:10.1088/0004-637X/699/1/31.

Akiyama, K. and Event Horizon Telescope Collaboration. First Sagittarius A* Event Horizon Telescope Results: Imaging the Galactic Supermassive Black Hole Sgr A*. In *American Astronomical Society Meeting Abstracts*, volume 54 of *American Astronomical Society Meeting Abstracts*, page 211.03, June 2022.

Allard, D. and Protheroe, R. J. Interactions of UHE cosmic ray nuclei with radiation during acceleration: consequences for the spectrum and composition. *A&A*, 502(3):803–815, August 2009. doi:10.1051/0004-6361/200911839.

Angel, J. R. P. and Stockman, H. S. Optical and infrared polarization of active extragalactic objects. *ARA&A*, 18:321–361, January 1980. doi:10.1146/annurev.aa.18.090180.001541.

Bai, X.-N., Caprioli, D., Sironi, L., and Spitkovsky, A. Magnetohydrodynamic-particle-in-cell Method for Coupling Cosmic Rays with a Thermal Plasma: Application to Non-relativistic Shocks. *ApJ*, 809(1):55, August 2015. doi:10.1088/0004-637X/809/1/55.

Ball, D., Sironi, L., and Özel, F. The Mechanism of Electron Injection and Acceleration in Transrelativistic Reconnection. *ApJ*, 884(1):57, October 2019. doi:10.3847/1538-4357/ab3f2e.

Balsara, D. S. and Spicer, D. S. A Staggered Mesh Algorithm Using High Order Godunov Fluxes to Ensure Solenoidal Magnetic Fields in Magnetohydrodynamic Simulations. *Journal of Computational Physics*, 149(2): 270–292, March 1999. doi:10.1006/jcph.1998.6153.

Baring, M. G. Diffusive Shock Acceleration : the Fermi Mechanism. In Giraud-Heraud, Y. and Tran Thanh van, J., editors, *Very High Energy Phenomena in the Universe; Moriond Workshop*, page 97, January 1997.

Beniamini, P. and Giannios, D. Prompt gamma-ray burst emission from gradual magnetic dissipation. *MNRAS*, 468(3):3202–3211, July 2017. doi:10.1093/mnras/stx717.

Beniamini, P. and Piran, T. The emission mechanism in magnetically dominated gamma-ray burst outflows. *MNRAS*, 445(4):3892–3907, December 2014. doi:10.1093/mnras/stu2032.

Bessho, N. and Bhattacharjee, A. Fast collisionless reconnection in electron-positron plasmasa). *Physics of Plasmas*, 14(5):056503, May 2007. doi:10.1063/1.2714020.

Blandford, R., Meier, D., and Readhead, A. Relativistic Jets from Active Galactic Nuclei. *ARA&A*, 57:467–509, August 2019. doi:10.1146/annurev-astro-081817-051948.

Borges, R., Carmona, M., Costa, B., and Don, W. S. An improved weighted essentially non-oscillatory scheme for hyperbolic conservation laws. *Journal of Computational Physics*, 227(6):3191–3211, March 2008. doi:10.1016/j.jcp.2007.11.038.

Böttcher, M. Modeling the emission processes in blazars. *ApSS*, 309(1-4): 95–104, June 2007. doi:10.1007/s10509-007-9404-0.

Burgess, J. M., Greiner, J., Bégué, D., Giannios, D., Berlato, F., and Lipunov, V. M. Viewing short Gamma-ray Bursts from a different angle. *Frontiers in Astronomy and Space Sciences*, 7:40, August 2020. doi:10.3389/fspas.2020.00040.

Caprioli, D., Amato, E., and Blasi, P. The contribution of supernova remnants to the galactic cosmic ray spectrum. *Astroparticle Physics*, 33 (3):160–168, April 2010. doi:10.1016/j.astropartphys.2010.01.002.

Cargo, P. and Gallice, G. Roe Matrices for Ideal MHD and Systematic Construction of Roe Matrices for Systems of Conservation Laws. *Journal of Computational Physics*, 136(2):446–466, September 1997. doi:10.1006/jcph.1997.5773.

Cerutti, B. Present Status Of Particle Acceleration In Relativistic Outflows. In *High Energy Phenomena in Relativistic Outflows VII*, page 12, July 2019.

Chael, A. A., Johnson, M. D., Narayan, R., Doeleman, S. S., Wardle, J. F. C., and Bouman, K. L. High-resolution Linear Polarimetric Imaging for the Event Horizon Telescope. *ApJ*, 829(1):11, September 2016. doi:10.3847/0004-637X/829/1/11.

Che, H. How anomalous resistivity accelerates magnetic reconnection. *Physics of Plasmas*, 24(8):082115, August 2017. doi:10.1063/1.5000071.

Chiuderi, C. and Velli, M. *Fisica del Plasma*. 2012. doi:10.1007/978-88-470-1848-8.

Condon, J. J. and Ransom, S. M. *Essential Radio Astronomy*. 2016.

Costa, E., Frontera, F., Heise, J., Feroci, M., in't Zand, J., Fiore, F., Cinti, M. N., Dal Fiume, D., Nicastro, L., Orlandini, M., Palazzi, E., Rapisarda#, M., Zavattini, G., Jager, R., Parmar, A., Owens, A., Molendi, S., Cusumano, G., Maccarone, M. C., Giarrusso, S., Coletta, A., Antonelli, L. A., Giommi, P., Muller, J. M., Piro, L., and Butler, R. C. Discovery of an X-ray afterglow associated with the γ-ray burst of 28 February 1997. *Nature*, 387(6635):783–785, June 1997. doi:10.1038/42885.

Courant, R., Friedrichs, K., and Lewy, H. Über die partiellen Differenzengleichungen der mathematischen Physik. *Mathematische Annalen*, 100: 32–74, January 1928. doi:10.1007/BF01448839.

Dainotti, M. G., Del Vecchio, R., and Tarnopolski, M. Gamma-Ray Burst Prompt Correlations. *Advances in Astronomy*, 2018:4969503, January 2018. doi:10.1155/2018/4969503.

de Gouveia Dal Pino, E. M. and Kowal, G. Particle Acceleration by Magnetic Reconnection. In Lazarian, A., de Gouveia Dal Pino, E. M., and Melioli, C., editors, *Magnetic Fields in Diffuse Media*, volume 407 of *Astrophysics and Space Science Library*, page 373, January 2015. doi:10.1007/978-3-662-44625-6_13.

del Valle, M. V., de Gouveia Dal Pino, E. M., and Kowal, G. Properties of the first-order Fermi acceleration in fast magnetic reconnection driven

by turbulence in collisional magnetohydrodynamical flows. *MNRAS*, 463 (4):4331–4343, December 2016. doi:10.1093/mnras/stw2276.

Del Zanna, L., Bucciantini, N., and Londrillo, P. An efficient shock-capturing central-type scheme for multidimensional relativistic flows. II. Magnetohydrodynamics. *A&A*, 400:397–413, March 2003. doi:10.1051/0004-6361:20021641.

Del Zanna, L., Zanotti, O., Bucciantini, N., and Londrillo, P. ECHO: a Eulerian conservative high-order scheme for general relativistic magnetohydrodynamics and magnetodynamics. *A&A*, 473(1):11–30, October 2007. doi:10.1051/0004-6361:20077093.

Del Zanna, L., Papini, E., Landi, S., Bugli, M., and Bucciantini, N. Fast reconnection in relativistic plasmas: the magnetohydrodynamics tearing instability revisited. *MNRAS*, 460(4):3753–3765, August 2016. doi:10.1093/mnras/stw1242.

Demianski, M., Piedipalumbo, E., Sawant, D., and Amati, L. Cosmology with gamma-ray bursts. I. The Hubble diagram through the calibrated $E_{p,I}$-E_{iso} correlation. *A&A*, 598:A112, February 2017. doi:10.1051/0004-6361/201628909.

Doeleman, S. S., Fish, V. L., Schenck, D. E., Beaudoin, C., Blundell, R., Bower, G. C., Broderick, A. E., Chamberlin, R., Freund, R., Friberg, P., Gurwell, M. A., Ho, P. T. P., Honma, M., Inoue, M., Krichbaum, T. P., Lamb, J., Loeb, A., Lonsdale, C., Marrone, D. P., Moran, J. M., Oyama, T., Plambeck, R., Primiani, R. A., Rogers, A. E. E., Smythe, D. L., SooHoo, J., Strittmatter, P., Tilanus, R. P. J., Titus, M., Weintroub, J., Wright, M., Young, K. H., and Ziurys, L. M. Jet-Launching Structure Resolved Near the Supermassive Black Hole in M87. *Science*, 338(6105): 355, October 2012. doi:10.1126/science.1224768.

Drake, J. F., Opher, M., Swisdak, M., and Chamoun, J. N. A Magnetic Reconnection Mechanism for the Generation of Anomalous Cosmic Rays. *ApJ*, 709(2):963–974, February 2010. doi:10.1088/0004-637X/709/2/963.

Drake, J. F., Swisdak, M., and Fermo, R. The Power-law Spectra of Energetic Particles during Multi-island Magnetic Reconnection. *ApJL*, 763 (1):L5, January 2013. doi:10.1088/2041-8205/763/1/L5.

Evans, C. R. and Hawley, J. F. Simulation of Magnetohydrodynamic Flows: A Constrained Transport Model. *ApJ*, 332:659, September 1988. doi:10.1086/166684.

Event Horizon Telescope Collaboration, Akiyama, K., Alberdi, A., Alef, W., Asada, K., Azulay, R., Baczko, A.-K., Ball, D., Baloković, M., Barrett, J., and al. First M87 Event Horizon Telescope Results. I. The Shadow of the Supermassive Black Hole. *ApJL*, 875(1):L1, April 2019. doi:10.3847/2041-8213/ab0ec7.

Eyink, G., Vishniac, E., Lalescu, C., Aluie, H., Kanov, K., Bürger, K., Burns, R., Meneveau, C., and Szalay, A. Flux-freezing breakdown in high-conductivity magnetohydrodynamic turbulence. *Nature*, 497(7450): 466–469, May 2013. doi:10.1038/nature12128.

Fermi, E. On the Origin of the Cosmic Radiation. *Physical Review*, 75(8): 1169–1174, April 1949. doi:10.1103/PhysRev.75.1169.

Foschini, L. What we talk about when we talk about blazars? *Frontiers in Astronomy and Space Sciences*, 4:6, July 2017. doi:10.3389/fspas.2017.00006.

Frank-Kamenetskii, D. A. *Plasma, the fourth state of matter*. 1972.

Gardiner, T. A. and Stone, J. M. An unsplit Godunov method for ideal MHD via constrained transport. *Journal of Computational Physics*, 205 (2):509–539, May 2005. doi:10.1016/j.jcp.2004.11.016.

Giacomazzo, B. and Rezzolla, L. The exact solution of the Riemann problem in relativistic magnetohydrodynamics. *Journal of Fluid Mechanics*, 562:223–259, September 2006. doi:10.1017/S0022112006001145.

Giannios, D. Prompt GRB emission from gradual energy dissipation. *A&A*, 480(2):305–312, March 2008. doi:10.1051/0004-6361:20079085.

Giannios, D. Reconnection-driven plasmoids in blazars: fast flares on a slow envelope. *MNRAS*, 431(1):355–363, May 2013. doi:10.1093/mnras/stt167.

Godunov, S. K. A Finite Difference Method for the Computation of Discontinuous Solutions of the Equations of Fluid Dynamics. *Mat. Sb.*, 47 (8-9):357–393, 1959.

Gordovskyy, M., Browning, P. K., and Vekstein, G. E. Particle acceleration in a transient magnetic reconnection event. *A&A*, 519:A21, September 2010a. doi:10.1051/0004-6361/200913569.

Gordovskyy, M., Browning, P. K., and Vekstein, G. E. Particle Acceleration in Fragmenting Periodic Reconnecting Current Sheets in Solar Flares. *ApJ*, 720(2):1603–1611, September 2010b. doi:10.1088/0004-637X/720/2/1603.

Gottlieb, S. and Shu, C. W. Total variation diminishing Runge-Kutta schemes. *Mathematics of Computation*, 67(221):73–85, January 1998.

Graham, D. B., Khotyaintsev, Y. V., André, M., Vaivads, A., Divin, A., Drake, J. F., Norgren, C., Le Contel, O., Lindqvist, P. A., Rager, A. C., Gershman, D. J., Russell, C. T., Burch, J. L., Hwang, K. J., and Dokgo, K. Direct observations of anomalous resistivity and diffusion in collisionless plasma. *Nature Communications*, 13:2954, May 2022. doi:10.1038/s41467-022-30561-8.

Greisen, K. End to the Cosmic-Ray Spectrum? *PhRvL*, 16(17):748–750, April 1966. doi:10.1103/PhysRevLett.16.748.

Guo, F., Li, H., Daughton, W., and Liu, Y.-H. Formation of Hard Power Laws in the Energetic Particle Spectra Resulting from Relativistic Magnetic Reconnection. *PhRvL*, 113(15):155005, October 2014. doi:10.1103/PhysRevLett.113.155005.

Guo, F., Liu, Y.-H., Daughton, W., and Li, H. Particle Acceleration and Plasma Dynamics during Magnetic Reconnection in the Magnetically Dominated Regime. *ApJ*, 806(2):167, June 2015. doi:10.1088/0004-637X/806/2/167.

Guo, F., Li, X., Daughton, W., Kilian, P., Li, H., Liu, Y.-H., Yan, W., and Ma, D. Determining the Dominant Acceleration Mechanism during Relativistic Magnetic Reconnection in Large-scale Systems. *ApJL*, 879 (2):L23, July 2019. doi:10.3847/2041-8213/ab2a15.

Hakobyan, H., Petropoulou, M., Spitkovsky, A., and Sironi, L. Secondary Energization in Compressing Plasmoids during Magnetic Reconnection. *ApJ*, 912(1):48, May 2021. doi:10.3847/1538-4357/abedac.

Harten, A., Lax, P. D., and Leer, B. v. On Upstream Differencing and Godunov-Type Schemes for Hyperbolic Conservation Laws. *SIAM Review*, 25(1):35, January 1983. doi:10.1137/1025002.

Heckman, T. M. and Best, P. N. The Coevolution of Galaxies and Supermassive Black Holes: Insights from Surveys of the Contemporary Universe. *ARA&A*, 52:589–660, August 2014. doi:10.1146/annurev-astro-081913-035722.

Hillas, A. M. The Origin of Ultra-High-Energy Cosmic Rays. *ARA&A*, 22: 425–444, January 1984. doi:10.1146/annurev.aa.22.090184.002233.

Honda, M. Ultra-high Energy Cosmic-ray Acceleration in the Jet of Centaurus A. *ApJ*, 706(2):1517–1526, December 2009. doi:10.1088/0004-637X/706/2/1517.

Hoshino, M. Nonthermal Particle Acceleration in Shock Front Region: "Shock Surfing Accelerations". *Progress of Theoretical Physics Supplement*, 143:149–181, January 2001. doi:10.1143/PTPS.143.149.

Ishibashi, W. and Courvoisier, T. J. L. X-ray power law spectra in active galactic nuclei. *A&A*, 512:A58, March 2010. doi:10.1051/0004-6361/200913587.

Janssen, M., Falcke, H., Kadler, M., Ros, E., Wielgus, M., Akiyama, K., Baloković, M., Blackburn, L., Bouman, K. L., Chael, A., and al. Event Horizon Telescope observations of the jet launching and collimation in Centaurus A. *Nature Astronomy*, 5:1017–1028, July 2021. doi:10.1038/s41550-021-01417-w.

Ji, H., Yamada, M., Hsu, S., and Kulsrud, R. Experimental Test of the Sweet-Parker Model of Magnetic Reconnection. *PhRvL*, 80(15):3256–3259, April 1998. doi:10.1103/PhysRevLett.80.3256.

Jiang, G.-S. and Shu, C.-W. Efficient Implementation of Weighted ENO Schemes. *Journal of Computational Physics*, 126(1):202–228, June 1996. doi:10.1006/jcph.1996.0130.

Kono, K. T., Takeuchi, T., Tashiro, H., Ichiki, K., and Takeuchi, T. T. Constraining the luminosity function of active galactic nuclei through the reionization observations in the SKA era. *arXiv e-prints*, art. arXiv:2104.05212, April 2021.

Kouveliotou, C., Meegan, C. A., Fishman, G. J., Bhat, N. P., Briggs, M. S., Koshut, T. M., Paciesas, W. S., and Pendleton, G. N. Identification of Two Classes of Gamma-Ray Bursts. *ApJ*, 413:L101, August 1993. doi:10.1086/186969.

Kowal, G., Lazarian, A., Vishniac, E. T., and Otmianowska-Mazur, K. Numerical Tests of Fast Reconnection in Weakly Stochastic Magnetic Fields. *ApJ*, 700(1):63–85, July 2009. doi:10.1088/0004-637X/700/1/63.

Kowal, G., de Gouveia Dal Pino, E. M., and Lazarian, A. Magnetohydrodynamic Simulations of Reconnection and Particle Acceleration: Three-dimensional Effects. *ApJ*, 735(2):102, July 2011. doi:10.1088/0004-637X/735/2/102.

Kowal, G., de Gouveia Dal Pino, E. M., and Lazarian, A. Particle Acceleration in Turbulence and Weakly Stochastic Reconnection. *PhRvL*, 108 (24):241102, June 2012. doi:10.1103/PhysRevLett.108.241102.

Kulsrud, R. M. Magnetic reconnection: Sweet-Parker versus Petschek. *Earth, Planets and Space*, 53:417–422, June 2001. doi:10.1186/BF03353251.

Kumar, P. and Zhang, B. The physics of gamma-ray bursts & relativistic jets. *Phys. Rep.*, 561:1–109, February 2015. doi:10.1016/j.physrep.2014.09.008.

Landi, S., Del Zanna, L., Papini, E., Pucci, F., and Velli, M. Resistive Magnetohydrodynamics Simulations of the Ideal Tearing Mode. *ApJ*, 806(1):131, June 2015. doi:10.1088/0004-637X/806/1/131.

Lazarian, A., Vlahos, L., Kowal, G., Yan, H., Beresnyak, A., and de Gouveia Dal Pino, E. M. Turbulence, Magnetic Reconnection in Turbulent Fluids and Energetic Particle Acceleration. *SSRv*, 173(1-4):557–622, November 2012. doi:10.1007/s11214-012-9936-7.

Lazzati, D. Short Duration Gamma-Ray Bursts and Their Outflows in Light of GW170817. *Frontiers in Astronomy and Space Sciences*, 7:78, November 2020. doi:10.3389/fspas.2020.578849.

LeVeque, R. J. *Finite volume methods for hyperbolic problems*. 2002.

Li, Y., Wu, N., and Lin, J. Charged-particle acceleration in a reconnecting current sheet including multiple magnetic islands and a nonuni-

form background magnetic field. *A&A*, 605:A120, September 2017. doi:10.1051/0004-6361/201630026.

Lloyd-Ronning, N. M., Dolence, J. C., and Fryer, C. L. A MAD model for gamma-ray burst variability. *MNRAS*, 461(1):1045–1052, September 2016. doi:10.1093/mnras/stw1366.

Londrillo, P. and del Zanna, L. On the divergence-free condition in Godunov-type schemes for ideal magnetohydrodynamics: the upwind constrained transport method. *Journal of Computational Physics*, 195 (1):17–48, March 2004. doi:10.1016/j.jcp.2003.09.016.

Loureiro, N. F. and Uzdensky, D. A. Magnetic reconnection: from the Sweet-Parker model to stochastic plasmoid chains. *Plasma Physics and Controlled Fusion*, 58(1):014021, January 2016. doi:10.1088/0741-3335/58/1/014021.

Loureiro, N. F., Schekochihin, A. A., and Uzdensky, D. A. Plasmoid and Kelvin-Helmholtz instabilities in Sweet-Parker current sheets. *PhRvE*, 87(1):013102, January 2013. doi:10.1103/PhysRevE.87.013102.

Lu, R.-S., Broderick, A. E., Baron, F., Monnier, J. D., Fish, V. L., Doeleman, S. S., and Pankratius, V. Imaging the Supermassive Black Hole Shadow and Jet Base of M87 with the Event Horizon Telescope. *ApJ*, 788(2):120, June 2014. doi:10.1088/0004-637X/788/2/120.

Lyubarsky, Y. and Liverts, M. Particle Acceleration in the Driven Relativistic Reconnection. *ApJ*, 682(2):1436–1442, August 2008. doi:10.1086/589640.

Ma, Z. W., Chen, T., Zhang, H. W., and Yu, M. Y. Effective Resistivity in Collisionless Magnetic Reconnection. *Scientific Reports*, 8:10521, July 2018. doi:10.1038/s41598-018-28851-7.

Malyshkin, L. M., Linde, T., and Kulsrud, R. M. Magnetic reconnection with anomalous resistivity in two-and-a-half dimensions. I. Quasistationary case. *Physics of Plasmas*, 12(10):102902–102902, October 2005. doi:10.1063/1.2084847.

Marcowith, A., Ferrand, G., Grech, M., Meliani, Z., Plotnikov, I., and Walder, R. Multi-scale simulations of particle acceleration in astro-

physical systems. *Living Reviews in Computational Astrophysics*, 6(1):1, March 2020. doi:10.1007/s41115-020-0007-6.

Massaro, E., Giommi, P., Leto, C., Marchegiani, P., Maselli, A., Perri, M., Piranomonte, S., and Sclavi, S. Roma-BZCAT: a multifrequency catalogue of blazars. *A&A*, 495(2):691–696, February 2009. doi:10.1051/0004-6361:200810161.

Mattia, G. and Fendt, C. Magnetohydrodynamic Accretion-Ejection: Jets Launched by a Nonisotropic Accretion-disk Dynamo. I. Validation and Application of Selected Dynamo Tensorial Components. *ApJ*, 900(1):59, September 2020a. doi:10.3847/1538-4357/aba9d7.

Mattia, G. and Fendt, C. Magnetohydrodynamic Accretion-Ejection: Jets Launched by a Nonisotropic Accretion-disk Dynamo. II. A Dynamo Tensor Defined by the Disk Coriolis Number. *ApJ*, 900(1):60, September 2020b. doi:10.3847/1538-4357/aba9d6.

McKinney, J. C. and Uzdensky, D. A. A reconnection switch to trigger gamma-ray burst jet dissipation. *MNRAS*, 419(1):573–607, January 2012. doi:10.1111/j.1365-2966.2011.19721.x.

Medina-Torrejón, T. E., de Gouveia Dal Pino, E. M., Kadowaki, L. H. S., Kowal, G., Singh, C. B., and Mizuno, Y. Particle Acceleration by Relativistic Magnetic Reconnection Driven by Kink Instability Turbulence in Poynting Flux-Dominated Jets. *ApJ*, 908(2):193, February 2021. doi:10.3847/1538-4357/abd6c2.

Melandri, A., Mundell, C. G., Kobayashi, S., Guidorzi, C., Gomboc, A., Steele, I. A., Smith, R. J., Bersier, D., Mottram, C. J., Carter, D., Bode, M. F., O'Brien, P. T., Tanvir, N. R., Rol, E., and Chapman, R. The Early-Time Optical Properties of Gamma-Ray Burst Afterglows. *ApJ*, 686(2):1209–1230, October 2008. doi:10.1086/591243.

Mignone, A. MHD Modeling: Aims, Usage, Scales Assessed, Caveats, Codes. In Torres, D. F., editor, *Modelling Pulsar Wind Nebulae*, volume 446 of *Astrophysics and Space Science Library*, page 187, January 2017. doi:10.1007/978-3-319-63031-1_9.

Mignone, A. and Del Zanna, L. Systematic construction of upwind constrained transport schemes for MHD. *Journal of Computational Physics*,

424:109748, January 2021. doi:10.1016/j.jcp.2020.109748.

Mignone, A., Bodo, G., Massaglia, S., Matsakos, T., Tesileanu, O., Zanni, C., and Ferrari, A. PLUTO: A Numerical Code for Computational Astrophysics. *ApJS*, 170(1):228–242, May 2007. doi:10.1086/513316.

Mignone, A., Zanni, C., Tzeferacos, P., van Straalen, B., Colella, P., and Bodo, G. The PLUTO Code for Adaptive Mesh Computations in Astrophysical Fluid Dynamics. *ApJS*, 198(1):7, January 2012a. doi:10.1088/0067-0049/198/1/7.

Mignone, A., Bodo, G., Vaidya, B., and Mattia, G. A Particle Module for the PLUTO Code. I. An Implementation of the MHD-PIC Equations. *ApJ*, 859(1):13, May 2018. doi:10.3847/1538-4357/aabccd.

Mignone, A., Mattia, G., Bodo, G., and Del Zanna, L. A constrained transport method for the solution of the resistive relativistic MHD equations. *MNRAS*, 486(3):4252–4274, July 2019. doi:10.1093/mnras/stz1015.

Mignone, A., Haudemand, H., and Puzzoni, E. A Guiding Center Implementation for Relativistic Particle Dynamics the PLUTO Code. *Submitted to Comput. Phys. Commun.*, 2022.

Mignone, A., Tzeferacos, P., and Bodo, G. High-order conservative finite difference GLM-MHD schemes for cell-centered MHD. *Journal of Computational Physics*, 229(17):5896–5920, August 2010. doi:10.1016/j.jcp.2010.04.013.

Mignone, A., Bodo, G., and Ugliano, M. Approximate Harten-Lax-van Leer Riemann solvers for relativistic magnetohydrodynamics. In *Numerical Methods for Hyperbolic Equations - Vázquez-Cendón et al. (eds*, pages 219–226. 2012b.

Miyoshi, T. and Kusano, K. A multi-state HLL approximate Riemann solver for ideal magnetohydrodynamics. *Journal of Computational Physics*, 208(1):315–344, September 2005. doi:10.1016/j.jcp.2005.02.017.

Morlino, G. and Caprioli, D. Strong evidence for hadron acceleration in Tycho's supernova remnant. *A&A*, 538:A81, February 2012. doi:10.1051/0004-6361/201117855.

Morris, P. J., Potter, W. J., and Cotter, G. The feasibility of magnetic reconnection powered blazar flares from synchrotron self-Compton emission. *MNRAS*, 486(2):1548–1562, June 2019. doi:10.1093/mnras/stz920.

Nalewajko, K., Uzdensky, D. A., Cerutti, B., Werner, G. R., and Begelman, M. C. On the Distribution of Particle Acceleration Sites in Plasmoid-dominated Relativistic Magnetic Reconnection. *ApJ*, 815(2):101, December 2015. doi:10.1088/0004-637X/815/2/101.

Netzer, H. Revisiting the Unified Model of Active Galactic Nuclei. *ARA&A*, 53:365–408, August 2015. doi:10.1146/annurev-astro-082214-122302.

Ohsuga, K., Mineshige, S., Mori, M., and Kato, Y. Global Radiation-Magnetohydrodynamic Simulations of Black-Hole Accretion Flow and Outflow: Unified Model of Three States. *PASJ*, 61(3):L7–L11, June 2009. doi:10.1093/pasj/61.3.L7.

Oka, M., Phan, T. D., Krucker, S., Fujimoto, M., and Shinohara, I. Electron Acceleration by Multi-Island Coalescence. *ApJ*, 714(1):915–926, May 2010. doi:10.1088/0004-637X/714/1/915.

Onofri, M., Isliker, H., and Vlahos, L. Stochastic Acceleration in Turbulent Electric Fields Generated by 3D Reconnection. *PhRvL*, 96(15):151102, April 2006. doi:10.1103/PhysRevLett.96.151102.

Padovani, P., Alexander, D. M., Assef, R. J., De Marco, B., Giommi, P., Hickox, R. C., Richards, G. T., Smolčić, V., Hatziminaoglou, E., Mainieri, V., and Salvato, M. Active galactic nuclei: what's in a name? *A&A Rev.*, 25(1):2, August 2017. doi:10.1007/s00159-017-0102-9.

Page, K. L., Reeves, J. N., O'Brien, P. T., and Turner, M. J. L. XMM-Newton spectroscopy of high-redshift quasars. *MNRAS*, 364(1):195–207, November 2005. doi:10.1111/j.1365-2966.2005.09550.x.

Panaitescu, A. and Kumar, P. Fundamental Physical Parameters of Collimated Gamma-Ray Burst Afterglows. *ApJL*, 560(1):L49–L53, October 2001. doi:10.1086/324061.

Papini, E., Landi, S., and Del Zanna, L. Fast Magnetic Reconnection: Secondary Tearing Instability and Role of the Hall Term. *ApJ*, 885(1): 56, November 2019. doi:10.3847/1538-4357/ab4352.

Parker, E. N. Sweet's Mechanism for Merging Magnetic Fields in Conducting Fluids. *JGR*, 62(4):509–520, December 1957. doi:10.1029/JZ062i004p00509.

Paul, A. and Vaidya, B. Effects of a velocity shear on double current sheet systems: Explosive reconnection and particle acceleration. *Physics of Plasmas*, 28(8):082903, August 2021. doi:10.1063/5.0054501.

Perna, R., Lazzati, D., and Giacomazzo, B. Short Gamma-Ray Bursts from the Merger of Two Black Holes. *ApJ*, 821(1):L18, April 2016. doi:10.3847/2041-8205/821/1/L18.

Pescalli, A., Ghirlanda, G., Salvaterra, R., Ghisellini, G., Vergani, S. D., Nappo, F., Salafia, O. S., Melandri, A., Covino, S., and Götz, D. The rate and luminosity function of long gamma ray bursts. *A&A*, 587:A40, March 2016. doi:10.1051/0004-6361/201526760.

Petropoulou, M. and Sironi, L. The steady growth of the high-energy spectral cut-off in relativistic magnetic reconnection. *MNRAS*, 481(4): 5687–5701, December 2018. doi:10.1093/mnras/sty2702.

Petropoulou, M., Giannios, D., and Sironi, L. Blazar flares powered by plasmoids in relativistic reconnection. *MNRAS*, 462(3):3325–3343, November 2016. doi:10.1093/mnras/stw1832.

Piconcelli, E., Jimenez-Bailón, E., Guainazzi, M., Schartel, N., Rodríguez-Pascual, P. M., and Santos-Lleó, M. The XMM-Newton view of PG quasars. I. X-ray continuum and absorption. *A&A*, 432(1):15–30, March 2005. doi:10.1051/0004-6361:20041621.

Piron, F. Gamma-ray bursts at high and very high energies. *Comptes Rendus Physique*, 17(6):617–631, June 2016. doi:10.1016/j.crhy.2016.04.005.

Priest, E. R. Magnetohydrodynamics: Overview. *Oxford Research Encyclopedia of Physics*, July 2020. doi:https://doi.org/10.1093/acrefore/9780190871994.013.6.

Pucci, F. and Velli, M. Reconnection of Quasi-singular Current Sheets: The "Ideal" Tearing Mode. *ApJ*, 780(2):L19, January 2014. doi:10.1088/2041-8205/780/2/L19.

Pudritz, R. E. and Ray, T. P. The Role of Magnetic Fields in Protostellar Outflows and Star Formation. *Frontiers in Astronomy and Space Sciences*, 6:54, July 2019. doi:10.3389/fspas.2019.00054.

Puzzoni, E., Mignone, A., and Bodo, G. On the impact of the numerical method on magnetic reconnection and particle acceleration - I. The MHD case. *MNRAS*, 508(2):2771–2783, December 2021. doi:10.1093/mnras/stab2813.

Puzzoni, E., Mignone, A., and Bodo, G. The impact of resistive electric fields on particle acceleration in reconnection layers. *MNRAS*, 517(1): 1452–1459, November 2022. doi:10.1093/mnras/stac2807.

Rembiasz, T., Obergaulinger, M., Cerdá-Durán, P., Aloy, M.-Á., and Müller, E. On the Measurements of Numerical Viscosity and Resistivity in Eulerian MHD Codes. *ApJS*, 230(2):18, June 2017. doi:10.3847/1538-4365/aa6254.

Ripperda, B., Porth, O., Xia, C., and Keppens, R. Reconnection and particle acceleration in interacting flux ropes - I. Magnetohydrodynamics and test particles in 2.5D. *MNRAS*, 467(3):3279–3298, May 2017a. doi:10.1093/mnras/stx379.

Ripperda, B., Porth, O., Xia, C., and Keppens, R. Reconnection and particle acceleration in interacting flux ropes - II. 3D effects on test particles in magnetically dominated plasmas. *MNRAS*, 471(3):3465–3482, November 2017b. doi:10.1093/mnras/stx1875.

Ripperda, B., Bacchini, F., Teunissen, J., Xia, C., Porth, O., Sironi, L., Lapenta, G., and Keppens, R. A Comprehensive Comparison of Relativistic Particle Integrators. *ApJS*, 235(1):21, March 2018. doi:10.3847/1538-4365/aab114.

Ripperda, B., Porth, O., Sironi, L., and Keppens, R. Relativistic resistive magnetohydrodynamic reconnection and plasmoid formation in merging flux tubes. *MNRAS*, 485(1):299–314, May 2019a. doi:10.1093/mnras/stz387.

Ripperda, B., Porth, O., and Keppens, R. Test particles in relativistic resistive magnetohydrodynamics. In *Journal of Physics Conference Series*,

volume 1225 of *Journal of Physics Conference Series*, page 012018, May 2019b. doi:10.1088/1742-6596/1225/1/012018.

Romero, G. E., Boettcher, M., Markoff, S., and Tavecchio, F. Relativistic Jets in Active Galactic Nuclei and Microquasars. *Space Science Reviews*, 207(1-4):5–61, July 2017. doi:10.1007/s11214-016-0328-2.

Santos-Lima, R., Lazarian, A., de Gouveia Dal Pino, E. M., and Cho, J. Diffusion of Magnetic Field and Removal of Magnetic Flux from Clouds Via Turbulent Reconnection. *ApJ*, 714(1):442–461, May 2010. doi:10.1088/0004-637X/714/1/442.

Sari, R., Piran, T., and Narayan, R. Spectra and Light Curves of Gamma-Ray Burst Afterglows. *ApJL*, 497(1):L17–L20, April 1998. doi:10.1086/311269.

Schumacher, J. and Kliem, B. Coalescence of magnetic islands including anomalous resistivity. *Physics of Plasmas*, 4(10):3533–3543, October 1997. doi:10.1063/1.872250.

Sironi, L. Nonideal Fields Solve the Injection Problem in Relativistic Reconnection. *PhRvL*, 128(14):145102, April 2022. doi:10.1103/PhysRevLett.128.145102.

Sironi, L. and Giannios, D. A Late-time Flattening of Light Curves in Gamma-Ray Burst Afterglows. *ApJ*, 778(2):107, December 2013. doi:10.1088/0004-637X/778/2/107.

Sironi, L. and Spitkovsky, A. Relativistic Reconnection: An Efficient Source of Non-thermal Particles. *ApJL*, 783(1):L21, March 2014. doi:10.1088/2041-8205/783/1/L21.

Sironi, L., Petropoulou, M., and Giannios, D. Relativistic jets shine through shocks or magnetic reconnection? *MNRAS*, 450(1):183–191, June 2015. doi:10.1093/mnras/stv641.

Stenson, E., Horn-Stanja, J., Stoneking, M., and Pedersen, T. Debye length and plasma skin depth: Two length scales of interest in the creation and diagnosis of laboratory pair plasmas. *J. Plasma Phys.*, 83(1):595830106, February 2017. doi:10.1017/S0022377817000022.

Stepanovs, D. and Fendt, C. Modeling MHD Accretion-Ejection—from the Launching Area to Propagation Scales. *ApJ*, 793(1):31, September 2014. doi:10.1088/0004-637X/793/1/31.

Striani, E., Mignone, A., Vaidya, B., Bodo, G., and Ferrari, A. MHD simulations of three-dimensional resistive reconnection in a cylindrical plasma column. *MNRAS*, 462(3):2970–2979, November 2016. doi:10.1093/mnras/stw1848.

Sweet, P. A. The Neutral Point Theory of Solar Flares. In Lehnert, B., editor, *Electromagnetic Phenomena in Cosmical Physics*, volume 6, page 123, January 1958.

Tsunetoe, Y., Mineshige, S., Kawashima, T., Ohsuga, K., Akiyama, K., and Takahashi, H. R. Investigating the Disk-Jet Structure in M87 through Flux Separation in the Linear and Circular Polarization Images. *ApJ*, 931(1):25, May 2022. doi:10.3847/1538-4357/ac66dd.

Urry, C. M. and Padovani, P. Unified Schemes for Radio-Loud Active Galactic Nuclei. *Publications of the ASP*, 107:803, September 1995. doi:10.1086/133630.

Uzdensky, D. A. Radiative Magnetic Reconnection in Astrophysics. In Gonzalez, W. and Parker, E., editors, *Magnetic Reconnection: Concepts and Applications*, volume 427 of *Astrophysics and Space Science Library*, page 473, January 2016. doi:10.1007/978-3-319-26432-5_12.

Uzdensky, D. A., Loureiro, N. F., and Schekochihin, A. A. Fast Magnetic Reconnection in the Plasmoid-Dominated Regime. *PhRvL*, 105 (23):235002, December 2010. doi:10.1103/PhysRevLett.105.235002.

Uzdensky, D. A. Magnetic Reconnection in Extreme Astrophysical Environments. *SSRv*, 160(1-4):45–71, October 2011. doi:10.1007/s11214-011-9744-5.

Vainio, R. Diffusive Shock Acceleration. In Ostrowski, M. and Schlickeiser, R., editors, *Plasma Turbulence and Energetic Particles in Astrophysics*, pages 232–245, December 1999.

van Paradijs, J., Groot, P. J., Galama, T., Kouveliotou, C., Strom, R. G., Telting, J., Rutten, R. G. M., Fishman, G. J., Meegan, C. A., Pettini, M., Tanvir, N., Bloom, J., Pedersen, H., Nørdgaard-Nielsen, H. U., Linden-

Vørnle, M., Melnick, J., Van der Steene, G., Bremer, M., Naber, R., Heise, J., in't Zand, J., Costa, E., Feroci, M., Piro, L., Frontera, F., Zavattini, G., Nicastro, L., Palazzi, E., Bennett, K., Hanlon, L., and Parmar, A. Transient optical emission from the error box of the γ-ray burst of 28 February 1997. *Nature*, 386(6626):686–689, April 1997. doi:10.1038/386686a0.

Vazza, F., Brüggen, M., and Gheller, C. Thermal and non-thermal traces of AGN feedback: results from cosmological AMR simulations. *MNRAS*, 428(3):2366–2388, January 2013. doi:10.1093/mnras/sts213.

Vlasov, A. A. Reviews of Topical Problems: the Vibrational Properties of AN Electron Gas. *Soviet Physics Uspekhi*, 10(6):721–733, June 1968. doi:10.1070/PU1968v010n06ABEH003709.

Wang, F. Y., Yi, S. X., and Dai, Z. G. Similar Radiation Mechanism in Gamma-Ray Bursts and Blazars: Evidence from Two Luminosity Correlations. *ApJL*, 786(1):L8, May 2014. doi:10.1088/2041-8205/786/1/L8.

Wang, F. Y., Dai, Z. G., and Liang, E. W. Gamma-ray burst cosmology. *New Astronomy Review*, 67:1–17, August 2015. doi:10.1016/j.newar.2015.03.001.

Werner, G. R., Uzdensky, D. A., Cerutti, B., Nalewajko, K., and Begelman, M. C. The Extent of Power-law Energy Spectra in Collisionless Relativistic Magnetic Reconnection in Pair Plasmas. *ApJL*, 816(1):L8, January 2016. doi:10.3847/2041-8205/816/1/L8.

Wijers, R. A. M. J., Rees, M. J., and Meszaros, P. Shocked by GRB 970228: the afterglow of a cosmological fireball. *MNRAS*, 288(4):L51–L56, July 1997. doi:10.1093/mnras/288.4.L51.

Willingale, R., O'Brien, P. T., Osborne, J. P., Godet, O., Page, K. L., Goad, M. R., Burrows, D. N., Zhang, B., Rol, E., Gehrels, N., and Chincarini, G. Testing the Standard Fireball Model of Gamma-Ray Bursts Using Late X-Ray Afterglows Measured by Swift. *ApJ*, 662(2):1093–1110, June 2007. doi:10.1086/517989.

Yamada, M., Kulsrud, R., and Ji, H. Magnetic reconnection. *Reviews of Modern Physics*, 82(1):603–664, January 2010. doi:10.1103/RevModPhys.82.603.

Zatsepin, G. T. and Kuzmin, V. A. Upper Limit of the Spectrum of Cosmic Rays. *Soviet Journal of Experimental and Theoretical Physics Letters*, 4: 78, August 1966.

Zenitani, S. and Hoshino, M. The Generation of Nonthermal Particles in the Relativistic Magnetic Reconnection of Pair Plasmas. *ApJL*, 562(1): L63–L66, November 2001. doi:10.1086/337972.

Zhang, H., Yan, D., and Zhang, L. Characterizing the γ-Ray Variability of Active Galactic Nuclei with the Stochastic Process Method. *ApJ*, 930 (2):157, May 2022. doi:10.3847/1538-4357/ac679e.

Zhdankin, V., Uzdensky, D. A., Perez, J. C., and Boldyrev, S. Statistical Analysis of Current Sheets in Three-dimensional Magnetohydrodynamic Turbulence. *ApJ*, 771(2):124, July 2013. doi:10.1088/0004-637X/771/2/124.

Zhou, X., Büchner, J., Bárta, M., Gan, W., and Liu, S. Electron Acceleration by Cascading Reconnection in the Solar Corona. II. Resistive Electric Field Effects. *ApJ*, 827(2):94, August 2016. doi:10.3847/0004-637X/827/2/94.

Zweibel, E. G. and Yamada, M. Perspectives on magnetic reconnection. *Proceedings of the Royal Society of London Series A*, 472(2196):20160479, December 2016. doi:10.1098/rspa.2016.0479.

Acknowledgements

Here I want to thank the people without whom both scientifically and humanly I would not have made it here.
My first thought and my first thanks go to my supervisor, Andrea Mignone. He has been my guide already during my undergraduate studies, and then throughout my journey as a Ph.D. student. Everything I've learned, I've learned from him: how to analyze data, talk at a conference, write a paper, etc. Besides being an excellent teacher, he is also a nice person who has always supported and encouraged me in what I have done.
In addition to my supervisor, there is another person without whom this thesis would not have been possible. I want to thank Gianluigi Bodo for his ideas and for always being available to help me with the papers we have published and more. Indeed, I probably would not have been able to organize the departure for New York without him.
Regarding New York, I would like to thank Lorenzo Sironi for giving me the amazing opportunity to work with him at Columbia University and for all his ideas and input which prompted me to look at my research with a different eye. Regarding the latter, I would also like to thank Bart Ripperda.
I would like to thank my committee, Luca Del Zanna and Franco Vazza for reading my thesis and giving me great advice on how to improve it, and Francesco Massaro also for help with visa documents.
A word of thanks goes out to Giancarlo who, besides being a great friend, helped me during my Ph.D. (computationally and emotionally). Thanks to him I managed to organize my first symposium.
I would also like to thank Bhargav for constructive discussions about my work and for his help with applications for postdocs.
This thesis is for my mother and brother, who always believed in me more than I did myself. There are not enough words to thank you. Thank

you for always being there when I needed you, for never making me miss anything, for supporting me and pushing me to the right choices, and for the times I spent at home where I did not have to worry about anything. I could have not done all of this without you.
Other members of my family have been important on this journey, my aunt Donatella and my uncle Sandro. They have always supported me like secondary parents and celebrated with me all the small achievements of my Ph.D. Thank you also to embark on a foolish adventure to come to visit me in New York.
I would like to thank Barbara and Roberto for welcoming me into their home as if I were their daughter during the lockdown. They made me feel at home during a difficult time by allowing me to work in a peaceful and familiar atmosphere.
Thanks also to Irene. Thank you for welcoming me like a sister during the lockdown, and sharing joys and sorrows with me. I can never thank you enough. Thank you also for all the English corrections!
A word of thanks goes to Carlotta e Davide, for being there forever. You have always been present at my most important achievements (and not only), always showing you're proud of me. I am also very proud of you and I miss our evenings all together.
Thanks to Giovanni, for his patience and for always supporting me. You've always been there for whatever I needed, listening to me, cheering me up, and sharing my enthusiasm for the results achieved.
Thanks also to Andrea and Leonardo, with whom I shared my studies starting at the University of Cagliari. Thank you for being my friends and watching over me.
Thanks also go to my roommate Irene, who shared the joys and sorrows of the Ph.D. with me every day. Thanks also for letting me escape from Turin and take a break with you in Liguria when I needed it.